# Characterizing prototype dishes for CHORD and HIRAX using reflectometry

Amanda Di Nitto

Department of Physics

McGill University, Montreal

April 2023

A thesis submitted to McGill University in partial fulfillment of the requirements for the degree of,

Master of Science, Major in Physics

# Table of Contents

# Abstract

In the coming years, several large scale radio interferometric arrays are scheduled to be built. The Hydrogen Radio Intensity Mapping eXperiment (HIRAX) located in the Karoo region in South Africa, and the Canadian Hydrogen Observatory and Radio-transient Detector (CHORD) located near Penticton, BC are two arrays are under construction which will consist of hundreds of dishes. The science driver for both arrays consists of mapping neutral hydrogen and discovering radio transients such as Fast Radio Bursts (FRBs). Maps of neutral hydrogen, which are created via 21cm intensity mapping, can provide insight into the expansion history of the universe and further constrain the nature of dark energy. Before committing to a final design for the CHORD/HIRAX dishes, we have built a small prototype array at the Dominion Radio Astronomy Observatory (DRAO) near Penticton, BC known as the Deep Dish Development Array (D3A). This array lets us test design choices in the field and will allow us to make any necessary updates to the design in order to meet the requirements of a 21cm intensity mapping array. This thesis focuses on the design of the dishes and the requirement for dish uniformity. The reflective surface of the dish is imbedded within the composite material. Since the foregrounds are much brighter than the 21cm signal, the reflective surface must be uniform on the order of 1mm or less. A technique known as reflectometry is presented as the only possible method to study the uniformity of the imbedded reflective surface. The reflectometer is also used to study the resonance behavior of the reflective surface. The depth calculations for the different dish samples returned with a maximum standard deviation of 0.035 mm with a precision of $\lesssim$ 0.050 mm, therefore the samples were within tolerance. The resonance behaviour had a much larger variance from day to day but the effects of surface imperfections and the testing equipment's role on these changes were studied.

# Résumé

Dans les années à venir, il est prévu de construire plusieurs réseaux radio-interférométriques à grande échelle. “L'Hydrogen Radio Intensity Mapping eXperiment” (HIRAX), situé dans la région du Karoo en Afrique du Sud, et le “Canadian Hydrogen Observatory and Radio-transient Detector" (CHORD), situé près de Penticton, en Colombie-Britannique, sont deux réseaux en cours de construction qui comprendront des centaines de paraboles. L'objectif scientifique de ces deux réseaux est de cartographier l'hydrogène neutre et de découvrir des phénomènes transitoires radioélectriques tels que les sursauts radioélectriques rapides (FRB). Les cartes de l'hydrogène neutre, créées par la cartographie de l'intensité à 21 cm, peuvent donner un aperçu de l'histoire de l'expansion de l'univers et restreindre davantage la nature de l'énergie sombre. Avant de s'engager dans la conception finale des antennes CHORD/HIRAX, nous avons construit un petit prototype d'antenne à l'Observatoire Fédéral de RadioAstronomie (OFRA) près de Penticton, en Colombie-Britannique, appelé “Deep Dish Development Array” (D3A). Ce réseau nous permet de tester les choix de conception sur le terrain et nous permettra d'apporter toute mise à jour nécessaire à la conception afin de répondre aux exigences d'un réseau de cartographie d'intensité de 21 cm. Cette thèse se concentre sur la conception des paraboles et sur l'exigence d'uniformité des paraboles. La surface réfléchissante de la parabole est incorporée dans le matériau composite. Comme les avant-plans sont beaucoup plus lumineux que le signal de 21 cm, la surface réfléchissante doit être uniforme, de l'ordre de 1 mm ou moins. Une technique connue sous le nom de réflectométrie est présentée comme la seule méthode possible pour étudier l'uniformité de la surface réfléchissante imbriquée. Le réflectomètre est également utilisé pour étudier le comportement de résonance de la surface réfléchissante. Les calculs de profondeur pour les différents échantillons de paraboles ont donné un écart type maximal de 0.0350 mm

avec une précision de $\lesssim 0.050$ mm, donc les échantillons étaient dans la tolérance accepté. Le comportement de résonance présentait une variance beaucoup plus importante d'un jour à l'autre, mais les effets des imperfections de surface et le rôle de l'équipement de test sur ces changements ont été étudiés.

# Acknowledgments

First off, a massive thank you to my supervisor Jon Sievers for supporting me throughout my degree and allowing me to explore a side of radio astronomy I had not known before. Further thanks to the D3A team both university and DRAO whose continued hard work on the new dishes has given me the opportunity to continue the reflectometer work and explore new parts of it. Thanks to Laura Gonzalez Escudero for joining in on this project and brining in new ideas and perspectives. A big thanks to my parents, Tara and Sal who were always supportive and are willing provide the material and know-how for whatever new thing I wanted to build for this project. Lastly but most importantly, to my partner Renz Airron Torres for helping me stay sane while pursuing a masters during a pandemic and for your endless support during this adventure.

# Contribution of Authors

The original characterization and preliminary testing using the McGill reflectometer was conducted by E. Pieters [26]. Her work is detailed in Chapter 3 (specifically section 3.2 and 3.3), including previous data she collected and how it was used for the current work along with the original testing protocols. The original analysis code presented in section 4.2.2 was written by E. Pieters. All changes made to the code by the author are also presented in the same section. All the new testing protocols detailed in Chapter 4 (specifically section 4.1 and 4.3-4.5) are created by the author and the original testing protocol in section 4.2 was created by E. Pieters but modified by the author. All results presented in Chapter 5 were taken by the author along with the assistance of the undergraduate student L. Gonzalez Escudero.

# List of Figures

# List of Tables

# List of Abbreviations

**HIRAX**: The Hydrogen Intensity and Real-time Analysis eXperiment

**CHORD:** The Canadian Hydrogen Observatory and Radio-transient Detector

**DRAO:** The Dominion Radio Astrophysical Observatory

**CHIME:** The Canadian Hydrogen Intensity Mapping Experiment

**D3A(6):** The Deep Dish Development Array

**RF:** Radio Frequency

**BAO:** Baryon Acoustic Oscillations

**CMB:** The Cosmic Microwave Background

**LIM:** Line Intensity Mapping

**HI:** Neutral Hydrogen

**FRB:** Fast Radio Bursts

**RFI:** Radio Frequency Interference

**LNA:** Low-Noise Amplifier

**RFoF:** Radio Frequency over Fiber

**TE:** Transverse Electric mode

**TM:** Transverse Magnetic mode

**VNA/ENA:** Vector Network Analyzer/Network Analyzer (electrical)

**DUT:** Device-Under-Testing

**FWHM:** Full Width Half Maximum

**LWD:** Long way of the diamond

**SWD:** Short way of the diamond

# Chapter 1:

# Thesis Outline

In this thesis we characterize different prototype reflector dishes using a method known as reflectometry which is a resonance cavity with a missing enclosing wall. We will begin by discussing the relevant background topics needed to discuss the projects the prototype dishes will be used for. In Chapter 2 we will introduce hydrogen intensity mapping along with the basics of radio interferometry before describing the different projects, namely HIRAX and CHORD, along with their scientific goals. In Chapter 3 we describe the method of reflectometry and its use in dish characterization. We will also characterize the McGill reflectometer specifically along with the initial simulations done to determine its resonance behaviour. In Chapter 4 the testing protocols using the reflectometer are described. The dish prototypes received are detailed along with all the tools, equipment and vector network analyzers used during testing. In Chapter 5 the results of the different tests performed are presented along with the discussion of the impact of these results. These results are used not simply to characterize the prototype dishes but to also develop more efficient testing methods for future dish samples which should provide more consistent results between different testing days. Chapter 6 will summarize the findings and provide the list of best practices developed for future reflectometer users.

# Chapter 2:

# Introduction

## 2.1 Radio Cosmology: Hydrogen Intensity Mapping

Dark matter and dark energy are believed to make up 95% of the matter in the universe with only 5% being the baryonic matter which we see now. For this reason, these two fields of study are very active with many different projects working to constrain the parameters developed so far. To understand how these two fields can be studied we must first understand the evolution of the universe. Immediately after the Big Bang the universe rapidly expanded and began to cool allowing the dense plasma of quarks, lepton and photons to form the first protons and electrons. This occurred roughly at $10^{-6}$ seconds after the Big Bang. The Big Bang Nucleosynthesis began at 0.1 seconds after the Big Bang until $10^{4}$ seconds. This process is where Helium, Deuterium and Lithium nuclei were formed [1]. The primordial plasma was still extremely hot and therefore the complete atoms did not form until the universe cools further leading into the next major phase.

As the universe continued to expand and cool it eventually became energetically favourable for the formation of hydrogen atoms. The formation of neutral hydrogen was less efficient than the formation of ionized hydrogen so after it was formed, the hydrogen atom would quickly fall to its neutral state by emitting a photon in what is known as the decoupling phase. This process meant that the plasma became transparent since there were not as many free electrons present to scatter light. Immediately after decoupling the emitted photons were able to travel freely and is known as the first observable light. After the first observable light, the universe may have been

transparent but due to the amount of neutral hydrogen atoms, most photons were quickly reabsorbed which reionized the hydrogen atom. Other atoms began forming as well including helium. This process continued and since there were no stars forming yet the universe remained dark. The Dark Ages lasted until the first stars were formed at approximately 200 million years after the Big Bang. The stars were capable of forming due to the non-uniform manner in which the gas was distributed. Regions of denser gas would lead to more matter interacting and therefore the regions would grow even denser. Eventually the regions grew dense enough for stellar fusion to begin and the first stars were formed.

As the universe was still a dense gas of atoms after the first stars were formed, the light from these stars could not travel very far before interacting with an atom. At approximately 400 million years (z~20) post Big Bang the ultraviolet light from the stars began reionizing the hydrogen surrounding it in the period known as reionization. The reionization of the neutral hydrogen surrounding the stars meant the universe became a plasma of ionized hydrogen again. While this occurred, stars and galaxies continued to form in the denser gas regions. As the universe had expanded since the first time it was ionized plasma, the matter was much more diffused. Finally at approximately 1 billion years after the Big Bang (z~6) the universe became transparent with the ionized plasma having all been transformed into galaxies and other large-scale objects [2]. The reason behind why the primordial intergalactic medium had denser regions which eventually lead to galaxy formations was the presence of dark matter in these forming regions. Dark matter is believed to be electrically neutral but very heavy so that formation regions have an even stronger gravitational pull on the gas surrounding them [3]. By

understanding the formation regions better, we can improve the constraints on dark matter which will eventually lead to a better understanding of the nature of dark matter itself.

When studying the evolution of the universe and the formation of galaxies, the most obvious way to describe it would be via a map displaying the structures observed within the universe. For radio cosmology, these maps are created via intensity mapping. Intensity mapping is a technique where instead of resolving individual galaxies and other large-scale structures one by one we collect an aggregate of data using a chosen emission (such as visible light) and create a statistical map of the structures. This provides a way of creating a large-scale map of the structure formation with less detail but larger than is usually created with the traditional structure detection searches. Intensity mapping is an incredibly useful tool at higher redshifts (beyond z~3) as at these redshifts visible light or infrared emissions are much harder to track due to the large distance and the redshifting of the emissions from the galaxies and structures being studied [4]. Line Intensity Mapping (LIM) is when we us a specific spectral line to measure the many large-scale structures [4]. By tracking a source such as the 21 cm hydrogen line we can create a three-dimensional map rather than the two dimensions seen with the initial version of intensity mapping. The reason this is possible is due to the nature in which the 21 cm line has been redshifted. As we look further away, the 21-cm emission travelling towards us will be redshifted meaning the frequency of the emission has decreased. As we look further back in time the redshift will increase [5]. The redshift provides a distance measurement meaning the map can be made in three dimensions.

After recombination, neutral hydrogen (HI) became pervasive and although it was significantly reduced after reionization it remained present at an estimate of one atom per $cm^3$ [6]. Due to the hyperfine splitting (spin-flip transition) which occurs via the interaction between the magnetic moments of the electron and the proton, neutral hydrogen emits radiation at the 21 -cm line [6]. As this radiation has an absorption cross-section on the scale of $10^{-15}\ m^2$ it does not interact much with the HI surrounding it, nor does it scatter when passing through dust clouds. This creates a very reliable marker for mapping out structure formation within the universe and encompasses a large period of time making it an ideal tool to study the early universe.

One example of fluctuation measurements leading to a structure formation map is the cosmic microwave background (CMB) map. The CMB was an image created from the glow of first light at the beginning of the recombination era. It was used to prove that the gas dominated universe during this era was not uniform and that this inhomogeneity is what lead to large-scale structure formation. It is a two-dimensional map which measures the fluctuations in the temperature of the universe between 2.721 and 2.729 Kelvin and found that the smaller anisotropic regions did in fact correlate to galaxy formation regions [7]. The CMB map was a major step in understanding large-scale structure formation along with further development of dark matter and dark energy theories. Intensity maps can therefore be an important tool in studying formation using emissions which are not in the visible light region.

### 2.1.1 Baryonic Acoustic Oscillations

As mentioned earlier, dark energy remains one of the great unknowns in astrophysics. The effects of dark energy have only been seen on the largest scales therefore, to study it and further improve the constraints placed on it, the studies must be done on these scales. One method used is the study of Baryon Acoustic Oscillations (BAOs). Before recombination, the universe was opaque and filled with plasma. Any variations in density that developed would produce an acoustic wave which would travel in this plasma. At the decoupling era, the universe became transparent, and these acoustic waves stopped travelling effectively freezing the plasma density waves in place; this is what is known as the BAO. The acoustic oscillations are of characteristic comoving length 150 Mpc [8]. For reference, the Milky Way galaxy is 40 kpc and galaxy clusters are on average between 1 to 5 Mpc. The BAOs freeze in time at the same point that the CMB was created. These density waves create the peaks and troughs seen in the CMB angular power spectrum therefore the effect the BAOs have on the structure formation in the universe has already been tested and validated through the CMB anisotropies [7].

One method used when studying a field such as dark energy is the use of standard rulers. These objects are of a known size and can be classified in two ways; by being able to study this object at a single redshift or by studying a group of these objects for an array of redshifts whose size either changes in a well understood way or is constant with redshift [9]. The reason BAOs are an ideal standard ruler is that it is believed they fall into both classes. By studying BAOs at redshifts where the universe expansion became influenced by Dark Energy ($z \sim 2$), Dark Energy constraints can be improved and further narrowed [10]. As Intensity Mapping can measure the

distribution of baryonic matter at different redshifts, we can evaluate the large-scale structures at the BAO comoving length scale and use those as tracers for the expansion of the universe.

### 2.1.2 Radio Transients

Transient events are an astrophysical phenomenon which is characterised by short bursts of quickly varying radio pulses. There are several astrophysical objects which display this behavior such as pulsars and the recently discovered fast radio bursts (FRBs) [11]. Pulsars are rapidly rotating neutron stars that are highly magnetized which leads to beams of radiation (at radio frequencies) to be emitted at the magnetic pole. Due to the rotation, the emission beams can only be seen by telescopes when the poles are pointed towards us. The constant rotation leads to a consistent pulsing effect. FRBs on the other hand are not well understood yet. They are micro to millisecond long flashes at radio frequencies which appear to be originating beyond the Milky Way Galaxy but the cause of them remains a mystery [11].

## 2.2 Radio Interferometry

Radio telescopes can set up as a single telescope project or as an array of telescopes. The array can vary from a few telescopes to a thousand or more as described in Section 2.4. The size of a radio telescope dish determines the field of view. The BAOs being studied are large enough that a large dish is not required and since we are studying a fixed temperature signal, the sensitivity does not depend on dish size. By instead using an array of many smaller dishes, we can increase the sensitivity or resolution. These small telescopes are still capable of observing large scales but have some positive points such as being able to rotate the dishes for sky tracking easier than a very large telescope. As the array are still composed of individual telescopes, each dish has its

own antenna capable of collecting signals. The signals from each antenna are later combined by a correlator and create a complete image formed by the array.

### 2.2.1 Baseline

In interferometric set ups, baseline refers to the distance between two telescopes. The choice of baseline is important as it effects several different areas. As we are observing astrophysical objects in the far-field we can assume that the incoming waves can be treated as planar waves for the telescopes. The distance between the two telescopes dictates the geometric delay that the second telescope will experience in receiving the signal with respect to the first ([12] Eqn. 2.1):

$$\tau_g = \frac{D}{c} sin\theta \tag{2.1}$$

where θ is the angle at which the antenna is pointed away from the vertical axis (see Figure 2.1). Another aspect that baseline effects is the ability to resolve an image or not. The complex visibility function is the two-dimensional Fourier transform of the sky brightness distribution $T(l,m)$ ([12] Eqn. 3.9):

$$V(u,v) = \iint T(l,m) e^{-i2\pi(ul+vm)} dldm \tag{2.2}$$

where *(u,v)* are the east to west and north to south spatial frequencies in wavelengths respectively and *(l,m)* are the east to west and north to south angles in the tangential plane in radians respectively. Therefore, longer baselines lead to a higher spatial frequency of the sky brightness. The size of the object we wish to resolve will dictate the choice of baseline; shorter baselines for larger objects and longer baselines for smaller objects [13]. Lastly, when working with an interferometer of many telescopes, baseline redundancy is possible. This occurs when the same baseline is repeated in the array. The foreground signal is much brighter than the 21cm signal. Unfortunately, the process of subtracting the foregrounds from the weak signal is very

susceptible to calibration errors. One possible technique used to reduce this issue is redundant calibration which takes advantage of the redundant baselines in the interferometer set up. This technique was specifically developed for 21 cm topography studies as they require a high sensitivity on large spatial scales [14]. One array set up used to account for this had a large number of very short baselines with the overall array diameter being no more than a few kilometers [15]. For interferometers where the goal is intensity mapping, the clarity of a specific image is not as important as the overall survey, meaning redundant baselines is very useful for this type of science. Redundancy also allows for less data storage since the telescopes with identical baselines are collecting identical signals and these signals can be averaged before being saved [16]. The downside is that the tolerance for imperfections is much smaller for all parts of the telescope since redundancy requires the dishes, antennas, and electronics from each telescope to be as similar as possible. The reason behind the strict tolerance is the foreground signal. Since the foregrounds are much brighter than the 21 cm signal, we must ensure that the response similarity of the dishes is at approximately a part-per-thousand since that is our foreground-to-signal ratio (see Section 2.2.2 radiometer equation). If the tolerance is not met, the 21 cm signal will be much harder to recover from the foreground noise.

### 2.2.2 Noise Temperature

Noise temperature is a variable that expresses power spectral density, which is a description of how the power of the signal, $P_{in}$, is distributed over the frequency range in terms of temperature. It does so by calculating what temperature would produce that level of Nyquist Noise in the Rayleigh-Jeans domain. The relationship can be given as ([12] Eqn. 1.4):

$$P_{in} = k_B T \Delta \nu \tag{2.3}$$

where $k_B$ is the Boltzmann constant, $T$ the noise temperature and $\Delta\nu$ the frequency bandwidth. When discussing temperature in the field of radio astronomy there are a few different ones to take into consideration. The first is the antenna temperature, $T_A$, which is related to the power delivered to the antenna by the thermal source being observed. It is the noise temperature of the antenna therefore it is directly related to how bright the source we are observing is; the brighter the source the higher $T_A$, but it will always be less than the brightness temperature due to the efficiency of telescopes [13]. The next is the receiver noise, $T_{rec}$, which is the noise contribution caused by the receiver electronics and the dish. The receiver noise will be present whether we are looking at a source or not. The spillover temperature, $T_{spill}$, comes from ground spillover. This can be anything from Radio Frequency Interference (RFI) from nearby radio emitters, unwanted sources in the sky or signal spillover on the ground. These three temperatures add to give the noise temperature for the system:

$$T_{sys} = T_A + T_{rec} + T_{spill} \tag{2.4}$$

where $T_A$ is a sum of the many contributors to the antenna temperature such as the CMB [13]. Lastly the noise temperature measured from the source object which we are studying is given by $T_{sky}$. The addition of the system and sky temperatures gives us the total temperature. Interferometers aim to reduce the system temperature as much as possible as the sky temperature is quite small, usually below 10 K. As seen later in Section 2.3.1, the combined total temperature for set ups such as HIRAX (Section 2.4.1) are 50 K, therefore newer interferometers continue to work to minimize this system temperature as much as possible. One of the most important ways to reduce this is by choosing remote locations where the RFI can be minimized as much as possible.

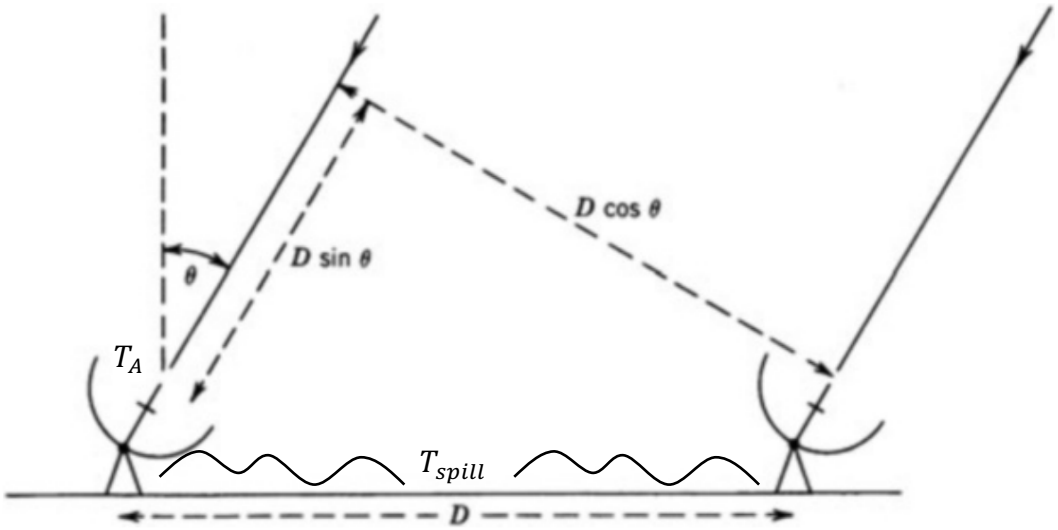


**Figure 2.1:** Interferometer set up described via two telescopes. $D$ is baseline, $\theta$ the angle from which the antenna is pointed away from the vertical axes and $Dcos\theta$ the simulated baseline. $T_{spill}$ is the noise from the ground and $T_A$ the noise from the antenna. $T_{rec}$ cannot be seen in this diagram as the receivers are not displayed. Photo credit [12]

Another important relationship comes from the radiometer equation also known as the signal-to-noise ratio ([13] Eqn. 3.154):

$$\sigma_T \approx \frac{T_{sys}}{\sqrt{\Delta\nu\tau}} \qquad (2.5)$$

where $\Delta\nu$ is the frequency bandwidth and $\tau$ the integration time. This equation specifically is known as the ideal radiometer equation for a total-power receiver. This equation provides a value which we can use to determine what is the weakest signal, $T_A$, we could measure. As long as the temperature of the source of interest is a couple times larger (generally five times) than the output rms of the radiometer equation we should be able to resolve the source from the noise

[13]. This value helps in determining the design constraints for the telescopes as they will be made based on how small a signal-to-foregrounds value we require for the source we want to resolve.

### 2.2.3 Correlation

The correlator is where the signals from all the telescopes are received and worked through. As the signals received includes a lot of noise, the correlator's function is to find the correlating signal of the source within all the noise. The cross-correlation for two input voltages is given by ([17] Eqn. 3.19):

$$r(\tau) = \lim_{T\to+\infty} \frac{1}{2T} \int_{-T}^{T} V_1(t) V_2^*(t-\tau) dt \tag{2.6}$$

where $V_2^*(t)$ is the complex conjugate of $V_2(t)$ and $\tau$ is the geometric delay (i.e. the delay in time for $V_2(t)$ to arrive at the correlator with respect to $V_1(t)$) [12]. The factor of *2T* is related to the integration time. The correlator output is inversely proportional to it, meaning a longer integration time will allow for observation of more sensitive or faint astrophysical objects.

## 2.3 Radio Telescope Components

### 2.3.1 Antennas

The antenna is comprised of two main sections, the feed, and the dish. The antennae's purpose is to collect the radiation signal from the source we are studying, couple it to the receiver where we digitize and later analyze. The type of antenna being used will depend on the wavelength of the source we intend to study. There are a few categories: wire antennas ($\lambda$ >1 m), reflector antennas ($\lambda$< 1 m) and a hybrid antenna which combines properties from both ( $\lambda$ ~1 m). For the purposes of hydrogen intensity mapping, reflector antennas are used. The reflector antennae's biggest

difference is the use of a dish. The dish is made of a reflective surface (to the wavelength of interest) which reflects the incoming signal to the feed. The dishes are generally parabolic in order to reflect back as much of the radiation received as possible to a singular point. The location of the feed is another option as there are antennas where the radiation is reflected directly to the feed and others where the radiation is focused towards a subreflector which then reflects the signal towards the feed. The subreflector choice tends to be used most frequently since the ground spillover noise can be reduced by placing the feed away from the direction of the ground spillover [12]. Lastly, the dish size is also important. The dish should be larger than the wavelength of the signal in order for the waves to be treated as planar based on the far-field approximation; this is at least larger than one meter for radio signals [17]. The choice for a single dish/a few dishes or interferometer set up will depend on the scientific goal of the project.

The feed collects the electromagnetic signal and converts it to a voltage signal. The design of the feed will also play a role in its ability to pick up either circularly or linearly polarized electromagnetic radiation. HIRAX, for instances, is using a dual-polarization feed based on the Canadian Hydrogen Intensity Mapping Experiment (CHIME) cloverleaf dual-polarization antenna which can take two linear polarizations offset by 90° received from the incident signal and send them both individually down the signal chain to be amplified, transformed and eventually digitized [18]. The dual-polarization is a common choice in radio astronomy as it allows for the study of two linear polarizations individually and to get the full stokes parameters.

### 2.3.2 Signal Chain

Once the signal has been collected by the feed and converted to a voltage, the signal is sent through a chain which will end with a digitized signal arriving at the correlator. The signal chain can vary slightly between different projects, but the essential process remains the same. The voltage signal from the feed is first amplified, usually by Low-Noise Amplifiers (LNA) which are capable of amplify a signal with as little degradation to the foreground-to-noise ratio as possible. This is important for intensity mapping since the foregrounds are much brighter than the 21 cm signal. It is then passed on to a local oscillator and frequency converter. HIRAX, for example, first converts the signal to optical via a Radio Frequency over Fiber (RFoF) transmitter, then sends it down an optical fiber and lastly transforms it back to radio frequency at the RFoF

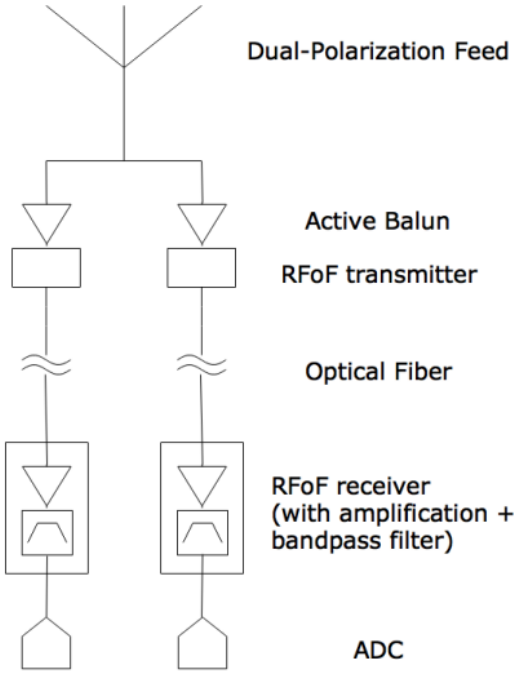


**Figure 2.2:** Signal chain for HIRAX antenna detailing the input voltage signal converted by the feed to the amplification, conversion to optical, passing via the optical fiber, return to radio frequency, amplification, filtering and eventual digitization of the signal. Photo credit [19].

receiver where it also amplifies and filters the signal (see Figure 2.2). Lastly the signal will pass through a digitizer and is then sent to the correlator which collects the signals from all the telescopes. The signal chain occurs per signal, meaning for a dual-polarization feed there are two signal chains, one for each linear polarization [18].

## 2.4 Interferometers

### 2.4.1 The Hydrogen Intensity and Real-time Analysis eXperiment (HIRAX)

HIRAX is a new radio interferometer being built in the Karoo desert in South Africa. The final array will have 1024, six-meter parabolic dishes on a 32x32 grid (~250mx250m) and a spacing of seven meters between dishes. The field-of-view will be between 15 and 56 square degrees [19]. As HIRAX aims to study BAOs as well as radio transients such as FRBs and pulsars, the frequency range will be between 400-800 MHz, meaning the minimum baseline required is approximately 40 meters, and a frequency resolution of 12 MHz. HIRAX will be a drift-scan telescope; the dishes will all be pointed at the meridian with a given declination and the sky will rotate overhead as the Earth moves [19]. This will provide a stripe of the sky of approximately 6° for each declination pointing. The six-meter dishes with have a focal ratio of $f/D = 0.25$ in order to try and reduce the cross talk between neighbouring antennas. HIRAX aims to have a high degree of geometric redundancy which improves the sensitivity of measurements. This means that we must have very strict requirements on the variations in the reflective surface of the dishes; the tolerance for surface imperfections is $\frac{\lambda}{50} = 7\text{mm}$ based on the Ruze equation [19] but this acts as an upper limit to ensure that the directivity of our beam pattern is not lost via larger side lobes caused by surface imperfections [20]. The tolerance followed during prototyping is set by the foreground-to-noise ratio which is a part-per-thousand meaning the dish tolerance is

below 1 mm [19]. The dishes will be capable of moving along one axis but will not be able to tilt more than 30° in each direction north-south. HIRAX will be using a Dual-Polarized antenna as described in section 1.3.2 (see Figure 2.2). Currently, an 8-dish prototype array is being tested while instrumentation decisions are made. Once this is concluded, a 128-dish array will be built and eventually the full 1024-dish array.

**Figure 2.3:** 8-dish prototype set up at HartRAO site. Dishes displayed are one of the prototypes which are being tested, other dish prototypes also exist but are not included in this photograph. Photo credit HIRAX Facebook page [21]

### 2.4.2 The Canadian Hydrogen Observatory and Radio-transient Detector (CHORD)

CHORD is another future interferometer being built in Penticton, British Columbia at the Dominion Radio Astrophysical Observatory (DRAO) beside the current CHIME set up. It will contain 512 six-meter dishes with two outrigger stations between 30-3000km away. The frequency range observe is between 300 MHz to 1.5 GHz. By working with CHIME, the field-

of-view for the combined observatories will be approximately 200 square degrees which will be matched by the outriggers [22]. CHORD plans on using dual-polarization feeds like HIRAX but these will be Ultra-Wideband Feeds which involves a newer feed design. They will also employ Ultra-Low-Noise-Amplifiers which should reduce the system temperature compared to HIRAX. CHORD will be a drift-scan telescope and will also have high geometric redundancy. Due to the frequency range of study, the tolerance for the dish surface imperfections will be even more stringent with dish surface variance tolerance set to 0.5 mm. Composite dish prototypes are being designed and tested at the Deep Dish Development Array (D3A).

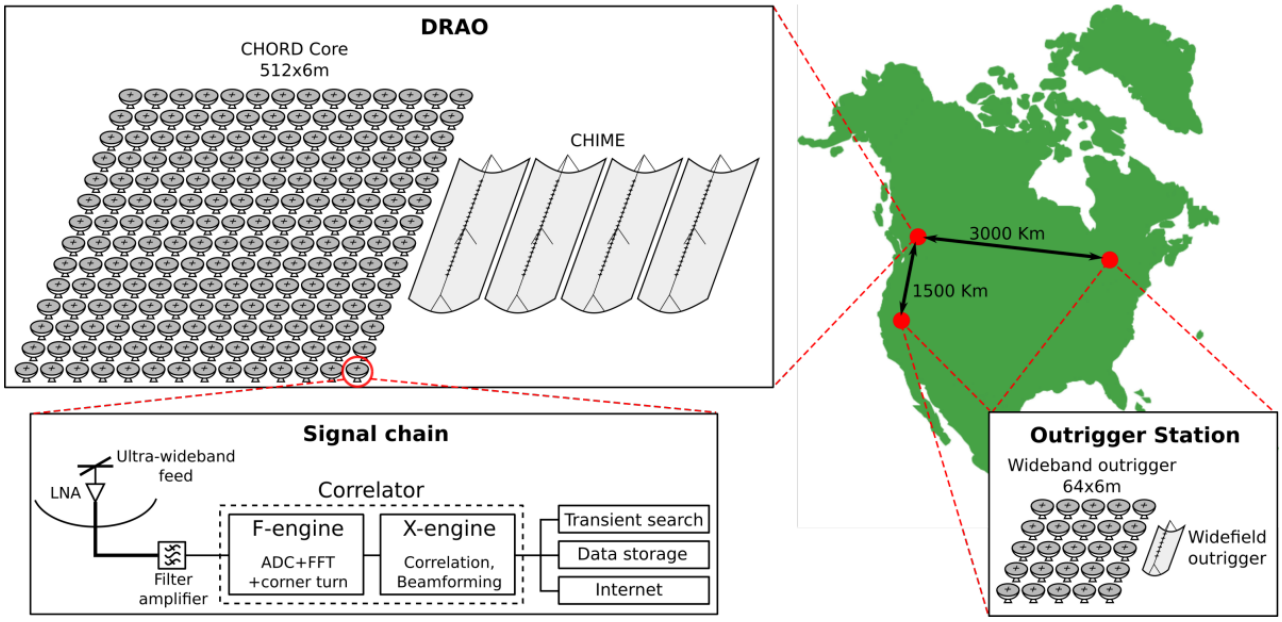


**Figure 2.4:** Description of CHORD set up at the core site and outriggers. CHIME is active at core station already present but CHIME style widefield dishes at outriggers will be added for CHORD project. Outrigger station distances an estimate as exact locations have not been chosen. Signal chain for the CHORD dishes alone displayed. Photo credit [22]

### 2.4.3 Deep Dish Development Array (D3A)

D3A is where the dish, antenna and electronics prototyping for CHORD and HIRAX occurs. D3A is located at the DRAO near the current CHIME site and future CHORD site. The interferometer currently has two three-meter dishes and the new six-meter dish installed with plans to add two more six-meter dishes in the future. The dishes are made of a composite material with an expanded aluminum sheet embedded inside. The composite material is invisible at radio frequencies therefore the embedded mesh acts as the reflective surface. The mesh must obey the same tolerance for surface variance as the composite surface itself since that will dictate how well we can take advantage of the geometric redundancy of the dishes. The surface of the dish is measured for conformity via laser tracking; measurements of the conformity of the embedded mesh require a different technique.

## 2.5 Summary

As a high tolerance for surface imperfections is required for the dishes for both HIRAX and CHORD a method to study the uniformity of the embedded mesh is required for full prototype evaluation. The field of reflectometry will be discussed in the next chapter and the McGill Reflectometer specifically will be characterized. As the reflectometer allows for more than just surface uniformity testing, the subsequent studies concerning resistivity and resonance behaviour analysis will be covered. The original characterization of the reflectometer and development of the analysis code was conducted by E. Pieters. All subsequent testing with the reflectometer conducted for the purpose of developing further analysis methods was completed by the author and the undergraduate student L. Gonzalez Escudero.

# Chapter 3:

# The Reflectometer

Arrays which employ redundancy, such as HIRAX/CHORD, require a high level of repeatability between individual telescopes. All individual parts of the telescopes must be as similar as possible including the dishes as the response similarity of the individual telescopes must be at the part-per-thousand level since that is our foreground-to-signal ratio. In order to ensure that the beams on the sky are the same the dish surfaces must be as close to identical as possible (on the order of 1 to 0.5 mm rms falls within the 1/1000 specification range). There are techniques such as laser tracking and photogrammetry which measure the uniformity of the composite material surface, but the composite material is transparent at the wavelengths of interest. For the radio waves, the embedded reflective material is the surface it will interact with, meaning this too must conform to the precision restrictions indicated. A technique known as reflectometry is used in order to study the electromagnetic uniformity of the dish. Reflectometers are also used to study the surface resistivity of the reflective surface since the uniformity of the embedded material is not the only variable which can affect the beams [23][24]. Should the resistivity of the embedded material vary significantly over the dish surface the beams will be negatively impacted again.

## 3.1 Reflectometry Principles

Reflectometry arose as a method to study electrically reflective surfaces without needing to be in direct contact with them [23]. The reflectometer is a cylindrical resonance cavity which lacks one of the end plates as seen in Figure 3.1. When the reflectometer is placed against a reflective surface, that surface acts as an end plate. The geometry of the reflectometer dictates which

frequencies the cavity can sustain resonance modes at if it were an enclosed cavity. With this knowledge, when placing the reflectometer against a surface we can determine the depth of the imbedded reflective surface by monitoring the resonance frequencies. The depth of the material will lead to a longer cavity and therefore will shift the resonance frequencies seen by the reflectometer. To be able to calculate the exact depth of the imbedded material we must first determine what resonance mode to use for this specific reflectometer. The basics of resonance cavities will be covered first and then the addition of the antenna, which changes the reflectometer from an empty cavity, will be discussed.

The resonance modes of a cylindrical cavity include both transverse electric (TE) and transverse magnetic (TM) modes. For either resonance modes, the z-component of the fields (electric or magnetic) must be zero so that only the transverse components are left. The cavity coordinates are provided in Figure 3.1 with *z* running lengthwise down the cavity. The radial component is given by *r* and the azimuthal by $\phi$. The TE and TM modes excited in the cavity are index by *n, m,* and *l.* The *n, m,* and *l* indexes correspond to the number of variations in the standing wave pattern in the $\phi$ , *r,* and *z* directions respectively [25]. Having zero variations along a certain direction would mean that the field strength is constant along that direction. Having a variation would means the number of periods of the wave increase by half. For example, when the index has a value of two, one sinusoidal wave has completed meaning the number of periods the wave has is one.

### 3.1.1 Resonance Modes for a Cylindrical Cavity

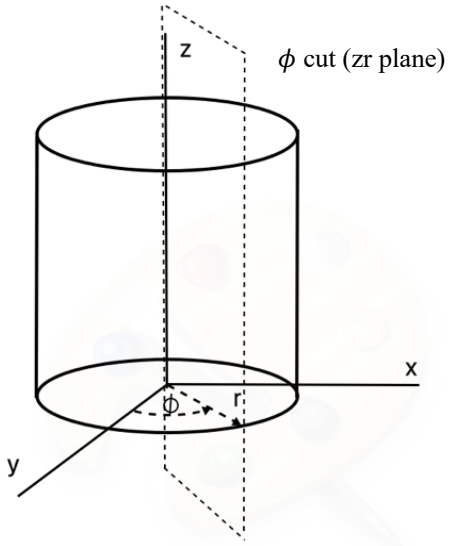


**Figure 3.1:** A cylindrical cavity with the cartesian coordinates as well as the cylindrical coordinates, which are the coordinates used for all calculations. A 2D plane cut example was included.

The resonant frequency for the TE mode is derived in ([25] Eqn. 6.53a):

$$f_{nml}^{TE} = \frac{c}{2\pi\sqrt{\mu_r \epsilon_r}} \sqrt{\left(\frac{p'_{nm}}{a}\right)^2 + \left(\frac{l\pi}{d}\right)^2} \tag{3.1a}$$

$$where,\ p'_{nm} = \left(\frac{d}{dx} J_n(x)\right)^{\frac{1}{m}} \tag{3.1b}$$

Where $a$ is the radius of the cavity, $d$ is the depth of the cavity, $c$ is the speed of light, $\mu_r$ and $\epsilon_r$ are the relative magnetic permeability and permittivity respectively. Similarly for the TM mode, ([25], Eqn. 6.53b):

$$f_{nml}^{TM} = \frac{c}{2\pi\sqrt{\mu_r \epsilon_r}} \sqrt{\left(\frac{p_{nm}}{a}\right)^2 + \left(\frac{l\pi}{d}\right)^2} \tag{3.2a}$$

$$where,\ p_{nm} = \left(J_n(x)\right)^{\frac{1}{m}} \tag{3.2b}$$

Where all previous values are the same except for $p_{nm}$. Note that for both TE and TM modes $n, m \geq 0$ but for the TE modes $l \geq 1$ and the TM modes $l \geq 0$. From these equations we can

determine the depth of the cavity so long as we know the radius of the cavity and the resonant frequency for a chosen TM or TE resonant mode. Using the TE mode equation, we find that the depth of the cavity is given by:

$$d = \frac{\pi}{\sqrt{\left(\frac{f_{nml}^{TE}}{\frac{c}{2\pi}}\right)^2 - \left(\frac{p'_{nm}}{a}\right)^2}} \tag{3.3}$$

Where $f_{nml}^{TE}$ is the resonance frequency of the chosen TE mode. This relationship is the core of what is used to determine the depth of an embedded reflective surface. A resonant mode is chosen and the frequency corresponding to that mode is monitored when the reflectometer is placed against a material with an imbedded electrically reflective surface. The changes in depth will lead to a shift in the resonance frequency we are tracking.

The resonant mode is chosen based on the fact that the reflective surface acting as the enclosing end plate for the reflectometer may not be in good electrical contact with the walls of the reflectometer. Therefore, a mode which does not require surface current between the cylinder walls and the end plates is the ideal choice. The $TE_{011}$ mode is the ideal candidate as the fields and the surface current die down to zero at the junction between the cylinder walls and the end plates. This can be seen in Figure 3.3, where it is shown that the $TE_{011}$ mode has a single variation in the *r,* and *z* directions. One large issue with the $TE_{011}$ mode is that it is located at the same frequency as the $TM_{111}$ mode. The $TM_{111}$ mode has a maximum surface current at the junction between the walls and the end plates (Figure 3.4). If the modes are not separated, the depth calculations may not work since the resonance of the cavity will depend more strongly on

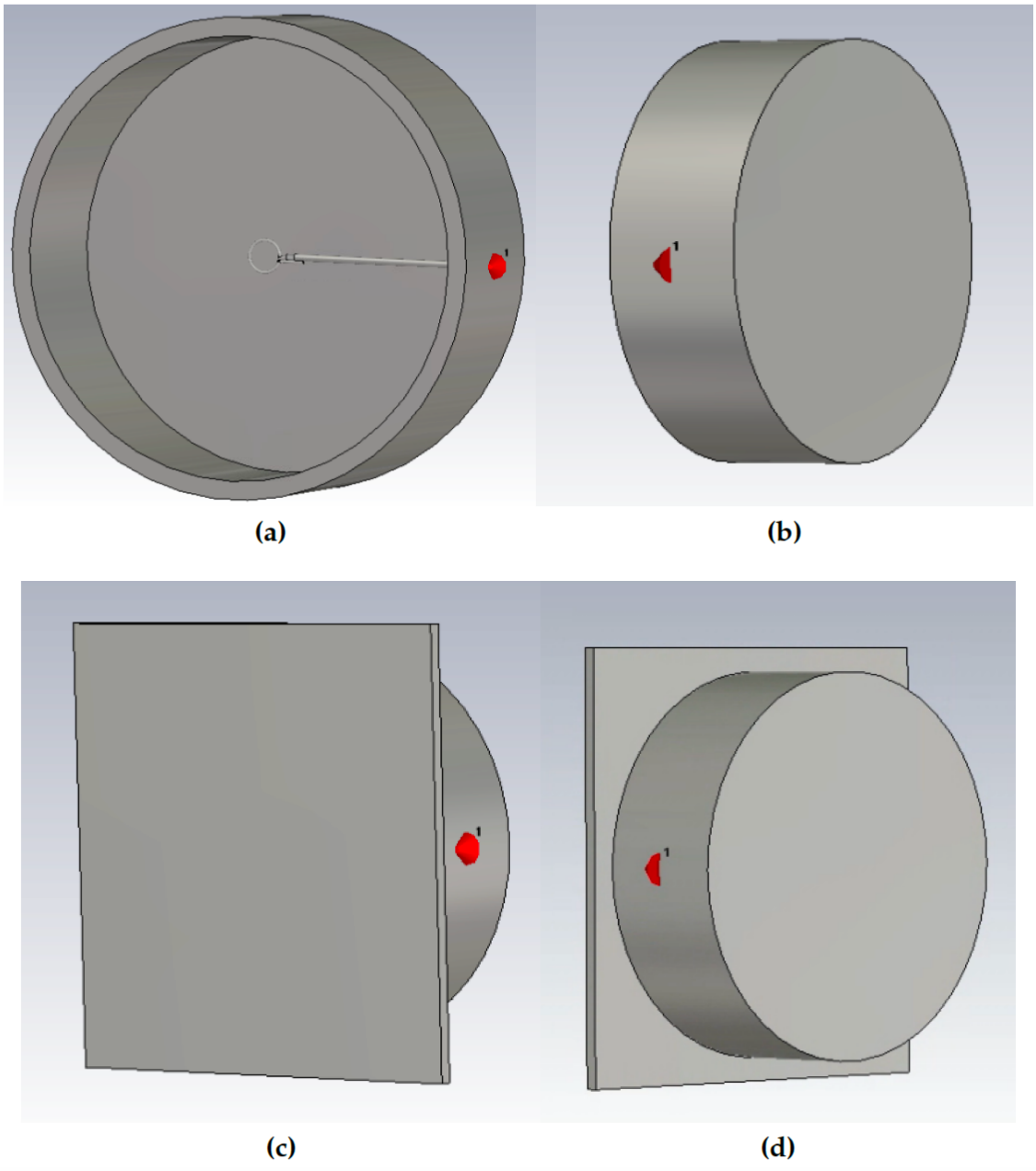


**Figure 3.2:** An electromagnetic simulation model made with CST Studio Suite of (a) the inside of the reflectometer along with the antenna inside, (b) the external walls of the reflectometer without an end plate. (c) and (d) are separate views of the reflectometer placed against an external reflective surface which acts as the reflectometer's enclosing wall. [26]

the contact between the walls and the imbedded reflective surface. In an ideal cylindrical resonator, the $TE_{011}$ and $TM_{111}$ modes resonate at the same frequency. However, adding an antenna to the resonator splits the resonances as we will see in section 3.3. The methods and equipment used to monitor the resonant frequency for the $TE_{011}$ mode are introduced in Chapter 4, but a small description of what is observed is required for the following sections. When the vector network analyzer is connected to the reflectometer it sends a signal to the reflectometer and it measures what is reflected back (the $S_{11}$parameter). The resonance modes, specifically the modes we are tracking, will produce a dip in the frequency sweep whereas the other frequencies will simply reflect back towards the vector network analyzer. These dips can be observed in Figure 3.6 and 3.7 later on in Sections 3.2 and 3.3 of this chapter.

## 3.2 The McGill Reflectometer

The McGill reflectometer's design was based off a similar reflectometer used for the KAT-7 array which is a radio telescope array located in Meerkat National Park, South Africa. This reflectometer also used the $TE_{011}$ mode and it was located at a frequency of 3.7GHz. The McGill reflectometer was designed by Isak Theron with the technical drawings provided by Simon Tartakovsky (see Appendix A). The inner length and radius are the values which affect the resonance properties of the reflectometer. For the McGill reflectometer, a shorter length over radius was chosen in order to increase sensitivity to depth changes (see Table 3.1). This reflectometer was designed to be small enough so that it remains portable and can be transported easily to site to be able to test the six-meter dishes. The $TE_{011}$ mode for an empty cavity falls at 3.863GHz.

The antenna for this reflectometer was built by E. Pieters. The antenna was modelled after the loop antenna used for the KAT-7 array reflectometer. The antenna consists of a loop made from copper wire with a diameter of 1.2 mm which is then soldered onto a stiff coaxial cable. The cable ends with an SMA connecter which is connected to an SMA bulkhead in the reflectometer wall that allows for the connection of the external coaxial cable on the exterior side of the wall (Figure 3.5). The external coaxial cable is connected to the reflectometer and is used to carry the signal to the analyzer. The radius of the antenna loop was chosen via CST simulation. The ideal radius provides a resonance dip near the resonance frequency we are tracking which is at 3.863 GHz for an empty cavity. It is also important that the $TE_{011}$ mode be easily identifiable in that the resonance is well separated from the $TM_{111}$ mode. The $TE_{011}$ mode is at a higher frequency than what will be observed by the constructed dishes (21 cm signal). This will have an effect on the Q factor but not the depth calculation. The discrepancy in frequency ranges should not lead to incorrect an conclusion as reflective loss is almost always worse at higher frequencies, meaning this value is expected to improve when the dish is being used by HIRAX/CHORD. As long as the Q factor measurements taken in Chapter 5 are in the higher Q region, the resistivity of the embedded mesh will be consistent enough to satisfy the surface variations conditions.

| Geometry | Size (mm) |
|---|---|
| Inner Radius | 75 |
| Outer Radius | 81 |
| Inner Length | 50 |
| Outer Length | 56 |

**Table 3.1:** The McGill Reflectometer's specifications. The reflectometer is made from aluminum.

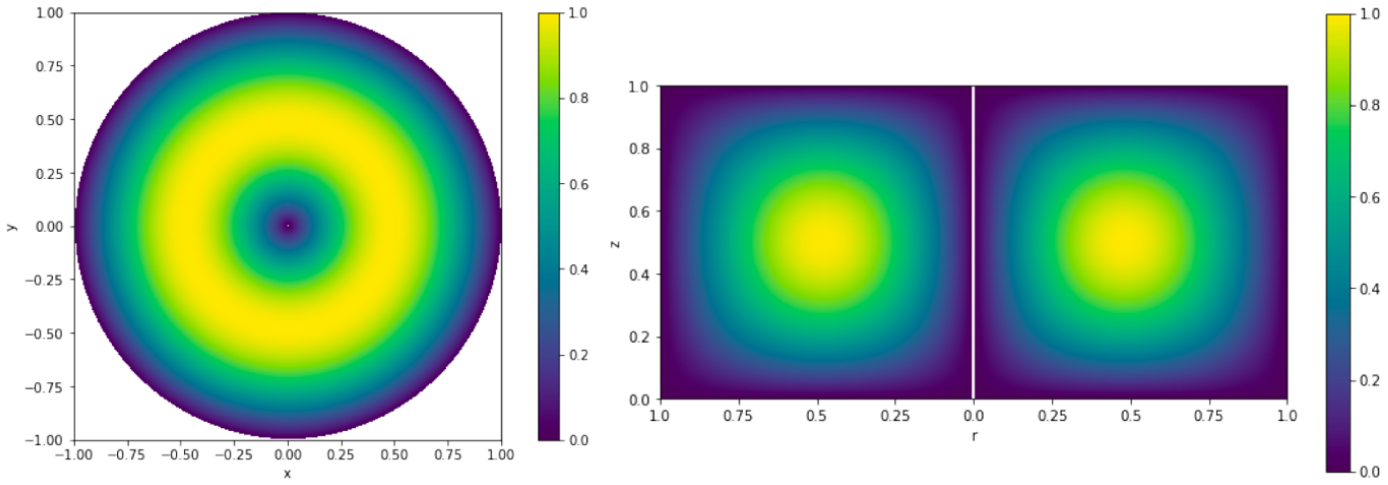


**(a)** E field cut at $z = 0.5$.

**(b)** E field cut at $\phi = 0$.

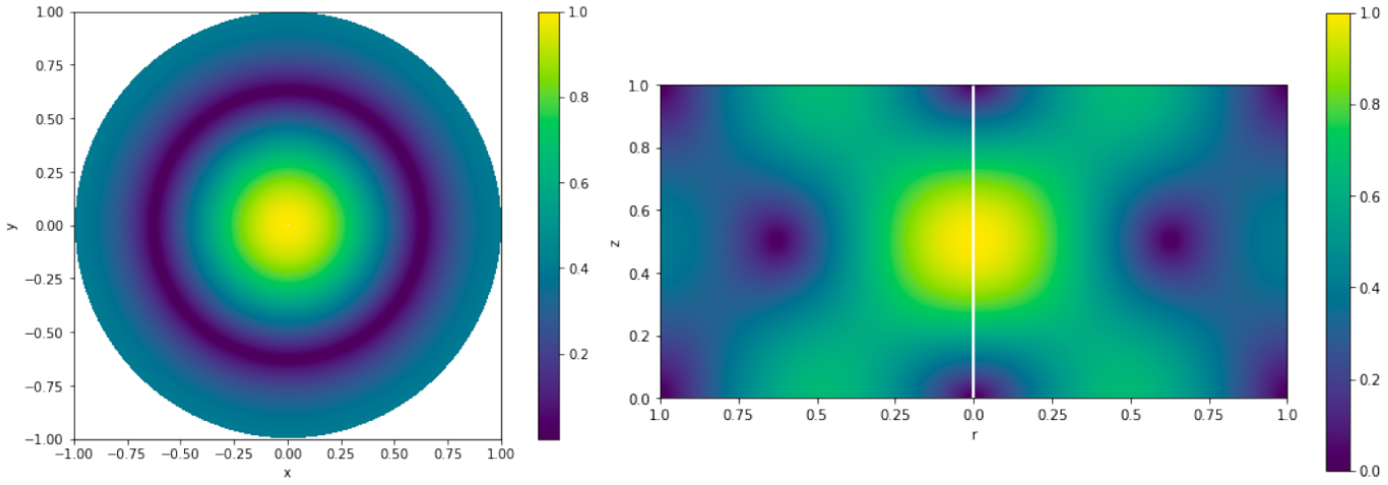


**(c)** H field cut at $z = 0.5$.

**(d)** H field cut at $\phi = 0$.

**Figure 3.3:** The calculated $TE_{011}$ electric and magnetic field magnitudes. The fields are normalized to the maximum magnitude for a given cut and then calculated using equations 6.54(a-f) in [25]. The 2D slice plots are produced using the script `mode_plotting.ipynb` which was written by E. Pieters [26]. The *E* and *H* field cuts prove that there are no variations along the $\phi$ direction and only one variation along *r* and *z*. The $\phi$ cut presented is set to zero but due to rotational symmetry the fields for the $\phi$ cuts will be identical no matter than angle set in the CST simulator. Since the electric fields go to zero where the walls meet the end plate, the surface current will also go to zero in this location. Therefore, the $TE_{011}$ mode does not rely on the electrical contact between the walls of the reflectometer and the end plate it is placed against and makes it an ideal mode to track for the depth calculation.

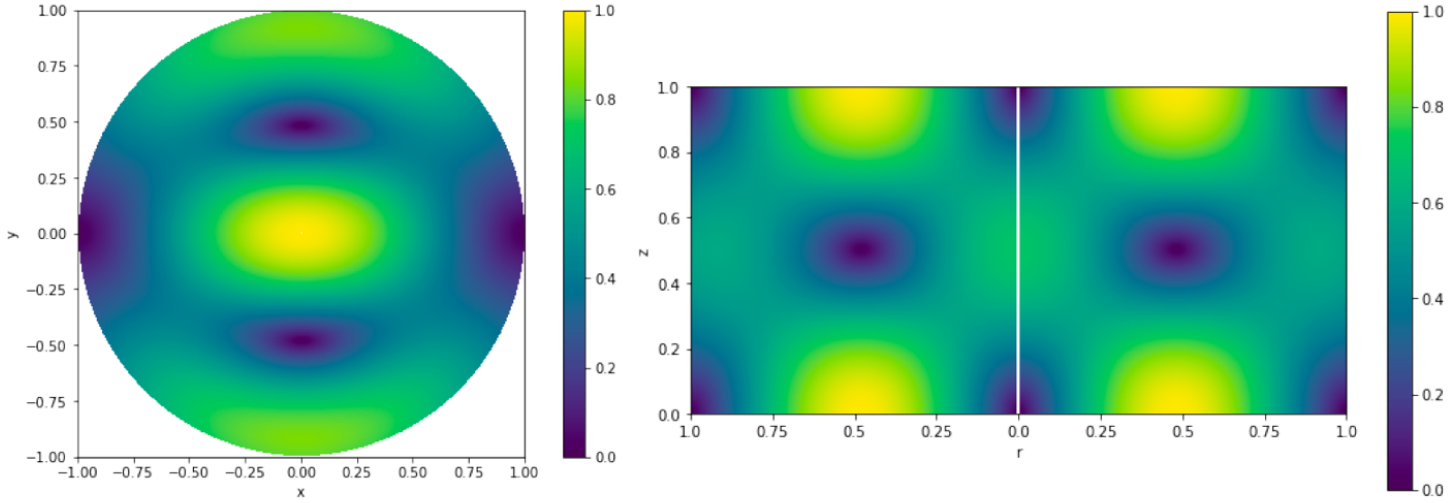


**(a)** E field cut at $z = 0.5$.

**(b)** E field cut at $\phi = 0$.

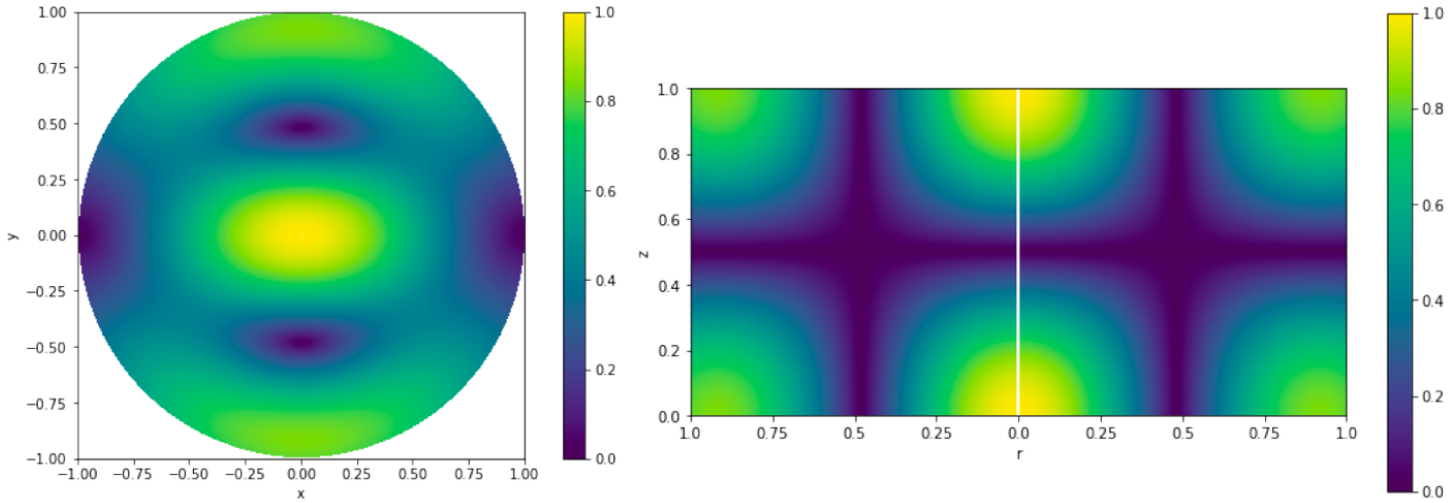


**(c)** H field cut at $z = 0$.

**(d)** H field cut at $\phi = 0$.

**Figure 3.4:** The calculated $TM_{111}$ electric and magnetic fields. The fields are normalized to the maximum magnitude for a given cut and then calculated using equations 6.54(a-f) in [25]. The 2D slice plots are produced using the script `mode_plotting.ipynb` which was written by E. Pieters [26]. Contrary to the $TE_{011}$ slice plots, the $E$ and $H$ fields have a single variation along the $\phi$ direction. This means that the fields and surface current do not go to zero where the walls meet the end plate for either E or H fields. The $\phi$ cut presented is set to zero but due to rotational symmetry the fields for the $\phi$ cuts will be identical no matter than angle set in the CST simulator. The $TM_{111}$ therefore relies on good electrical contact between the reflectometer and the end plate in order to measure any variance in depth. This makes the mode a bad candidate for tracking.

Three different loop sizes were tested against a painted metal sheet: 2.3 mm, 5 mm and 12 mm radius. It was found that the 2.3 mm and 5 mm loops produced similar results, but the 5 mm loop led to a slightly larger separation between the $TE_{011}$ and $TM_{111}$ mode dips (Figure 3.6). The 12 mm had a very large frequency gap between the two modes, and it was concluded that this loop was no longer acting as an electrically small antenna [17]. An electrically small antenna is an antenna whose size is much smaller (approximately one-tenth) than the wavelength of the signal it is receiving or sending. The reason we want to keep the antenna below this threshold is because when the loop is much smaller than the wavelength the current around the loop is constant but for a large loop antenna that may not be the case and this affects the radiation pattern seen. We want to maintain a low side lobe pattern as we want to maintain a high directivity in the radiation pattern, and this is easier to control with an electrically small antenna. The KAT-7 array reflectometer used an electrically small antenna as well therefore we ruled out the 12 cm antenna. Since the distinction between the two modes is important, the 5 mm antenna was chosen [26]. As the frequency the resonance dip is located at is slightly shifted from the frequency found for an empty cavity due to the antenna size, the shifts must be taken into account. The issue was studied through the CST simulations in order to explore how much the shifts might change the depth calculations. Calibration was also used to reduce this issue, and the calibration performed is explained in Chapter 4.

**(a)**

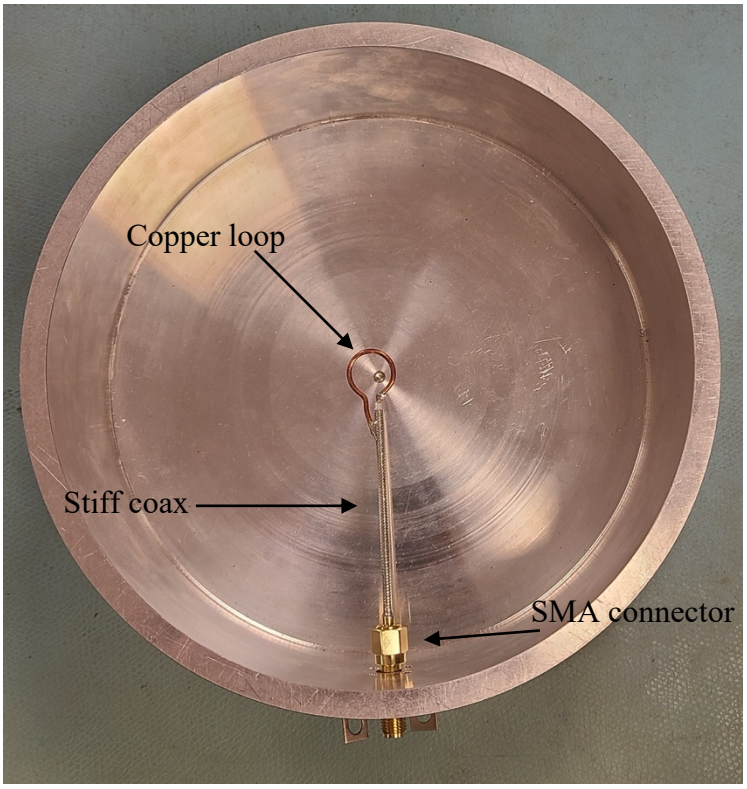


**(b)**

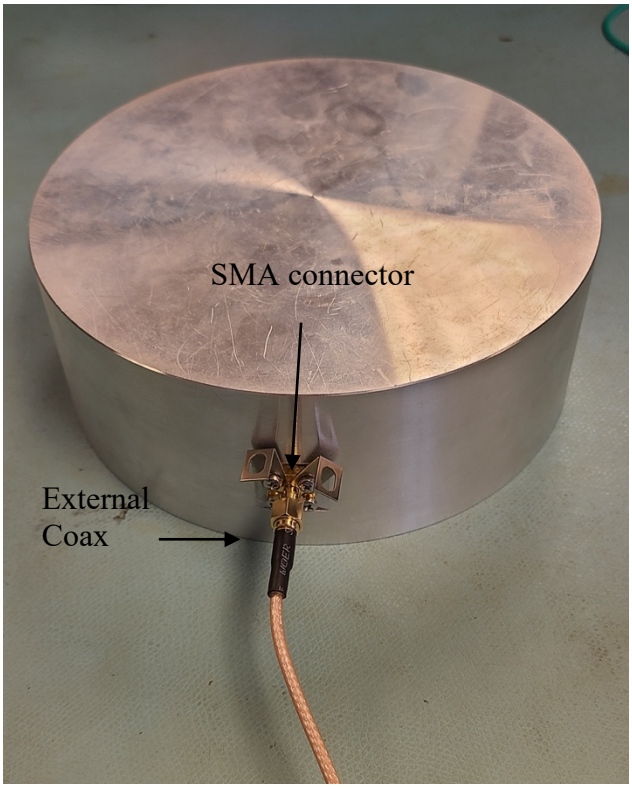


**Figure 3.5:** The reflectometer **(a)** internal view with the components of the antenna outlined and **(b)** the external view when the reflectometer is placed down on a surface. The external components used to connect the reflectometer to the analyzer and outlined as well.

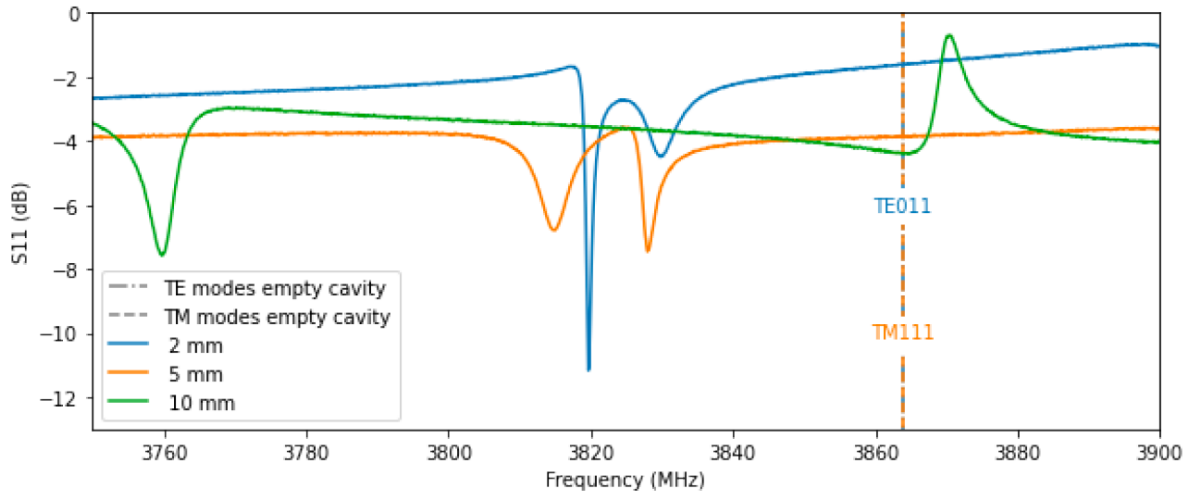


**Figure 3.6:** Reflectometer tests results for the resonance modes using the three different antennas. The test was conducted by E. Pieters [26] and the reflectometer was placed against a painted metal surface. The 2 mm (blue) and 5 mm (orange) results have the $TE_{011}$ and $TM_{111}$ located at very similar frequencies but the 10 mm (green) antenna has large gap between the two modes (approximately 100 MHz). Based on these results the 5 mm antenna was chosen as the two resonance modes are separated enough to avoid misidentification of the $TE_{011}$but not too separated as to no longer have an electrically small antenna.

## 3.3 CST Simulations

Due to the presence of the antenna, the resonance mode being tracked has shifted from its expected frequency for an empty cavity. The shift was measured by E. Pieters using CST Studio Suite, a 3D electromagnetic simulation and analysis software [27]. The change from empty cavity led to the presence of two dips very close to the original $TE_{011}$ frequency of 3.863 GHz. The CST simulator is used to determine which of the two dips corresponds to the mode of interest and which corresponds to the $TM_{111}$ mode. This was done using the CST monitor function which allows the user to request information concerning the electric field, magnetic

field, and surface current at pre-selected frequencies before running the simulation. These simulation runs were then compared to the field calculations for $TE_{011}$ and $TM_{111}$ for an empty cavity.

The frequencies were chosen by first running the simulation for the reflectometer's $S_{11}$ parameter or reflected power (see Chapter 4 for $S_{11}$ details). The simulation had two dips near the original $TE_{011}$ mode, one at 3.865 GHz and another at 3.843 GHz (Figure 3.7). The simulator was then used to calculate the field results and surface current for these two frequencies. The results compared to the empty cavity simulations (Figures 3.3 and 3.4) found that the 3.865 GHz dip corresponds to the $TE_{011}$ mode and that the 3.843 GHz dip corresponds to the $TM_{111}$ mode [26]. Therefore, the modes which are degenerate in an empty cavity are successfully separated enough for proper $TE_{011}$ mode detection when the antenna is present. This allows for the use of the $TE_{011}$ mode as the frequency to track for the depth calculations of an imbedded electromagnetic surface.

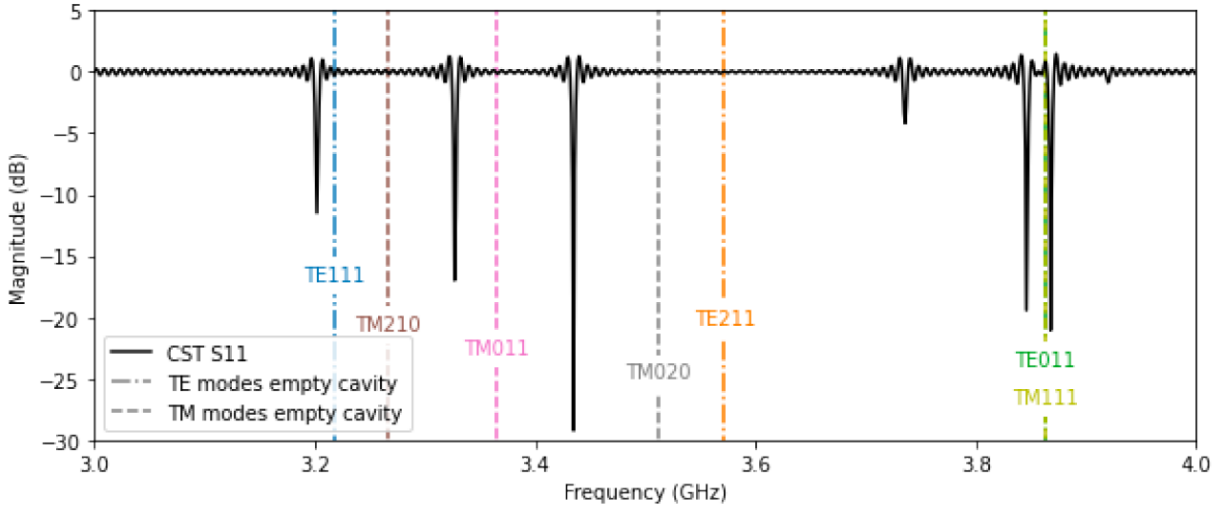


**Figure 3.7:** CST simulation of the reflectometer with the antenna [26]. The two modes are no longer collocated but now we must determine which is the $TE_{011}$ mode. The CST results gave two resonance dips located near the empty cavity frequency: one at 3.865 GHz and one at 3.843 GHz. We determine which is the correct mode by simulating the electric fields in the resonance cavity at those frequencies.

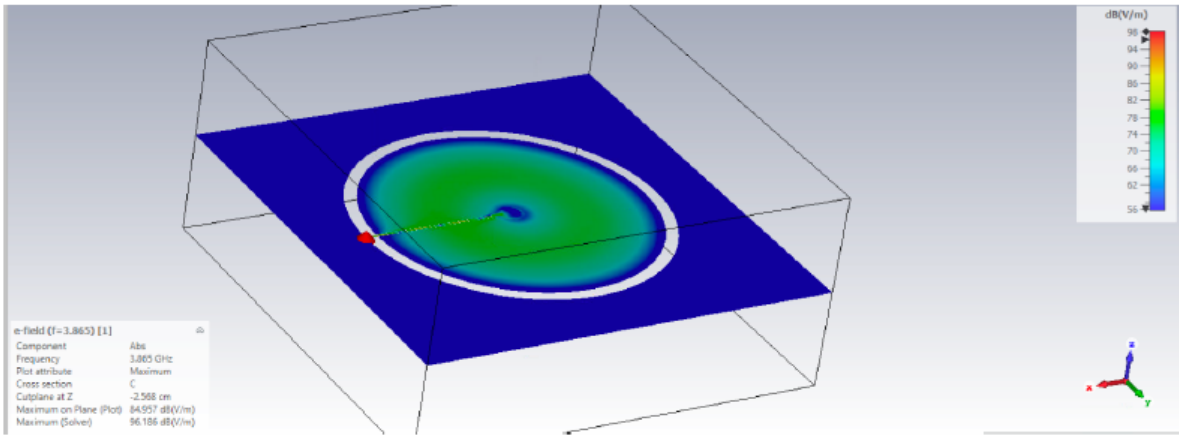

**(a)** E field cut ($xy$ plane).

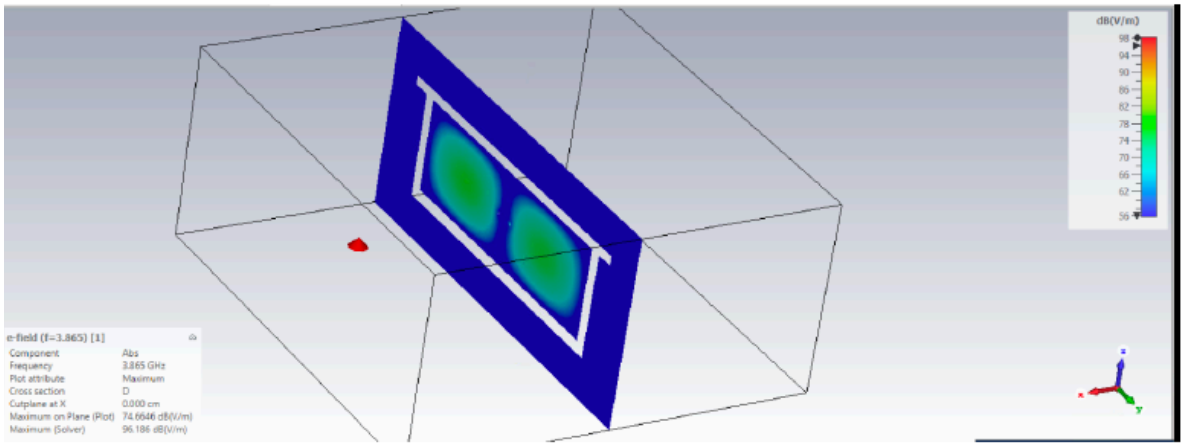

**(b)** E field cut ($yz$ plane).

**Figure 3.8:** The simulated electric field magnitudes at 3.865 GHz. These field simulations match the calculation slices performed for the $TE_{011}$ mode in an empty cavity in Figure 3.3. These simulations prove that the resonance dip at 3.865 GHz does correspond to the $TE_{011}$ mode when the antenna is present. The simulations were also performed for the magnetic field magnitudes and the surface current but since the mode we are interested in using is the transverse electric field we can confirm if the frequency is the correct mode with the electric field alone. Simulations were performed by E. Pieters in CST [26].

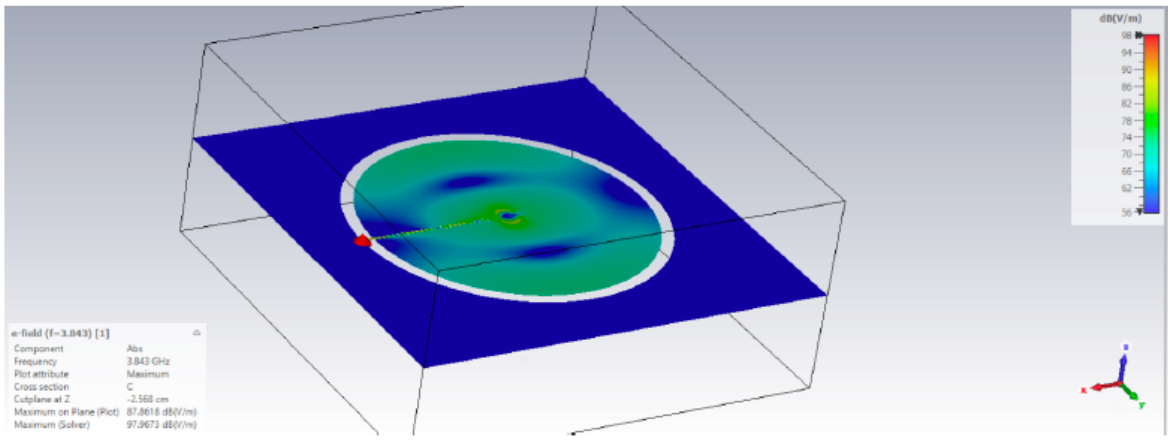

**(a)** E field ($xy$ plane).

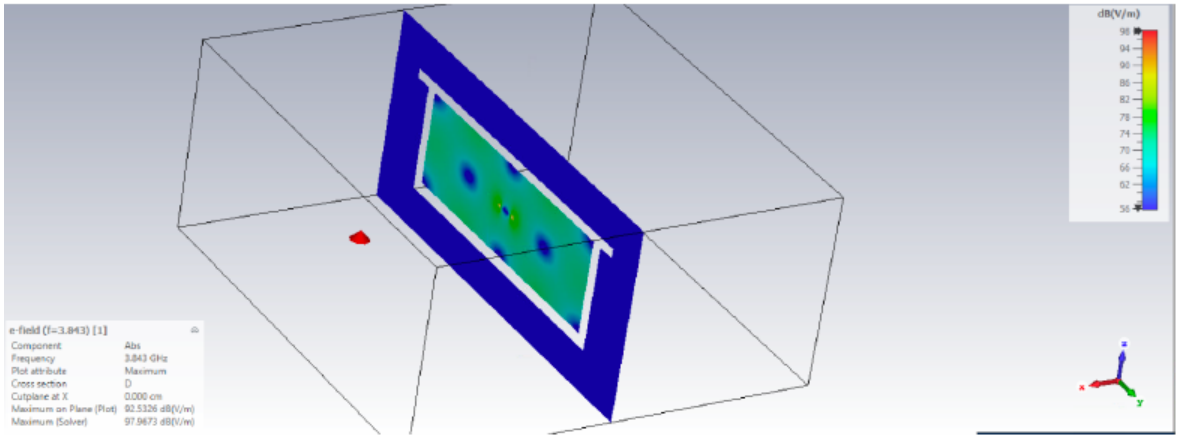

**(b)** E field ($yz$ plane).

**Figure 3.9:** The simulated electric field magnitudes at 3.843 GHz. These field simulations match the calculation slices performed for the $TM_{111}$ mode in an empty cavity in Figure 3.4. These simulations prove that the resonance dip at 3.843 GHz does correspond to the $TM_{111}$ mode when the antenna is present meaning the $TE_{011}$ and $TM_{111}$ are no longer collocated when the antenna is present. The simulations were also performed for the magnetic field magnitudes and the surface current but since the mode we are interested in using is the transverse electric field we can confirm if the frequency is the correct mode with the electric field alone. Simulations were performed by E. Pieters in CST [26].

The simulator was then used to get a preliminary understanding of how a surface offset caused by an embedded material would affect the $TE_{011}$ mode frequency as well as confirming that the reflectometer will be able to detect changes in depth below 0.5 mm as required by CHORD/HIRAX. The offsets were 0.125 mm each until a total offset of 1.25 mm was reached. The CST simulation found that there was a decrease in frequency of approximately 38-40 MHz per mm [26]. The value calculated by equation 3.1 found that the shift should be approximately 46 MHz per mm. The CST simulations calculates the presence of a physical antenna that changes the frequency response, but the real value is slightly higher than the CST values meaning the real values are slightly overestimated compared to the idealized case. Based on these values, in order to measure the surface to 0.1 MHz we must be able to measure the peak position to 5 MHz with the reflectometer and the analyzer.

# Chapter 4:

# Tests and Protocols

The reflectometer is a tool which we will use to measure the depth of the embedded conductive surface along with the resistive properties based on the cavity's resonance behaviour. In this chapter we will detail what equipment is used, specifically the type of vector network analyzer along with what settings and calibrations were used for them. The specific testing protocol for the depth and resistive measurements is detailed along with the tests done in an attempt to trouble shoot issues seen with the reflectometer. The issues seen during the standard test involved variations in the results for the depth but most importantly the resistive behaviour from day-to-day. Several types of tests are introduced to try and determine what may be causing, or at the very least worsening this issue. The data and subsequent analysis will be presented in Chapter 5.

## 4.1 Calibration and Equipment

Testing was completed using two types of Vector Network Analyzers (VNAs), the Fieldfox N9914A and the ENA E5080B Vector Network Analyzer. A VNA is a device which sends a signal at a specified frequency range out and measures how the Device-Under-Testing (DUT) responds via the signal reflected from the input side and the signal transmitted to the output side [28]. The resulting signal is compared to the original signal sent from the VNA and provides transmission, reflection, and impedance measurements along with the S-parameters. The S-parameter, also known as the scattering parameter, is a value which measures the reflected and

transmitted power in a network as a function of frequency. It describes the electrical behaviour of the DUT while undergoing constant stimuli via an electric signal (travelling power waves) over a period of time. S-parameter has both a magnitude, measured in decibels (dB), and phase, measured in degrees. The magnitude describes how strongly the stimuli affected the DUT via a dip or peak in the $S_{11}$ graph while the phase describes how much the scattered signal is delayed from the incident/input signal. The type of S-parameter studied will depend on the DUT. If only the reflections are to be measured, then the $S_{11}$ or $S_{22}$ parameters for the input or output port reflections respectively are the parameters of interest. If the DUT's transmission is being tested, then the S-parameters measured would be either $S_{21}$ or $S_{12}$ depending on if it was the forward or reverse transmission being tested [28]. For our purposes we will focus only on the $S_{11}$ parameter as the McGill reflectometer has only one port and is only capable of reflecting an input signal.

The $S_{11}$ parameter is also known as the reflection coefficient or reflected power. It is most commonly defined in terms of impedance ([17] Eqn. 4.42):

$$\mathrm{S}_{11} = \left|\frac{Z_L - Z_A}{Z_L + Z_A}\right| \tag{4.1}$$

where $Z_L$ is the load impedance and $Z_A$ is the antenna impedance. This quantifies how much of the incident wave is reflected, meaning if the antenna reflects nothing back, the reflection coefficient should be zero. In general, antennas aim to minimize this value since a low reflection coefficient would mean a smaller loss in signal power. The coefficient can be written in decibels via the return loss ([17] Eqn. 4.44):

$$RL = -20\log|S_{11}| \tag{4.2}$$

The measurements are conducted by having the VNA sweep a test tone and then measure the $S_{11}$ parameter reflected back across a frequency range which is chosen by the user. The antenna will efficiently couple to the cavity when driven by the VNA at the TE and TM resonant frequencies. The $S_{11}$ will show a sharp dip along with a phase change at the resonant frequencies when the VNA signal is broadcasted into the cavity, whereas the other frequencies will reflect off the antenna back to the VNA. The phase change can be seen in Figure 4.1 where the phase has a discontinuity right where the resonance frequency occurs. The phase flips from -180 to +180 degrees before flipping again at the next resonance frequency. The resonance frequency dip can be matched to the corresponding mode and the calculations of interest can be performed using the analysis code introduced in Section 4.2. It is important to save both the phase and magnitude when saving the measurement data as both can be used in detecting the resonance peaks. All datasets are therefore saved as single parameter Touchstone files (s1p) [29].

The ENA used was the E5080B from Keysight. It has a dynamic range of 140 dB and a max frequency of 53 GHz. Its maximum power output is 10 dBm (decibel-milliwatts) and it has one sweep per 2 ms when set at 201 points [30]. The Fieldfox is a handheld RF and microwave Analyzer. The Fieldfox used was the N9914A from Keysight which has a frequency range of 30 kHz to 6.5 GHz. The maximum power output depends on the frequency range chosen but for frequencies between 3-6.5 GHz the power output at high power is 1 dB. The dynamic range at high power with 100 points average for frequencies between 300 kHz and 9 GHz is 95 dB [31]. Calibration for both the Fieldfox and the ENA were performed using the Keysight Cal Kit 85033D/E for a 3.5 mm male connector on a single port. The settings were set to sweep between 3 GHz and 4 GHz with the highest resolution possible (for Fieldfox the maximum is 10001

channels over the frequency band and for the ENA it is 10003). Remaining settings were left on default for $S_{11}$ measurements. The metal sheet used for later tests was a 1.5”x1.5” (approximately 47cm x 47cm) aluminum sheet with a thickness of 3 mm.

## 4.2 Reflectometer Data Analysis

Analysis is performed with a version of the reflectometer analysis code called `reflectometer_analysis_template`. All code was originally written in Python 3.6 by E. Pieters but further additions and alterations were performed by the author and L. Gonzalez Escudero. The package has three main routines, the analysis template mentioned above, the code which performs all the calculations along with the statistics such as the standard deviation of the depth as well as the measurements using the resonance detection methods introduced in the following section and lastly a library of different resonance mode frequencies[1]. There are three main calculations being performed by the code: the depth of embedded reflective surface, width of peaks, and quality factor (Q factor) calculations. Before any calculations can occur, the code must search for the correct resonance peaks. There are several different peak finders used which leads to easier error detection.

### 4.2.1 Resonance Detection

#### Magnitude Peak Finder

This method employs Scipy signal’s `findpeaks` function [32] which will find both the positive and negative peaks for the $S_{11}$ magnitude in decibels (dB). One of the main issues with this method is that it occasionally choses the incorrect dips. This can occur for two main reasons. The

[1] All code can be found on Github at https://github.com/chord-observatory/D3A/tree/reflectometer/reflectometer

**(a)**

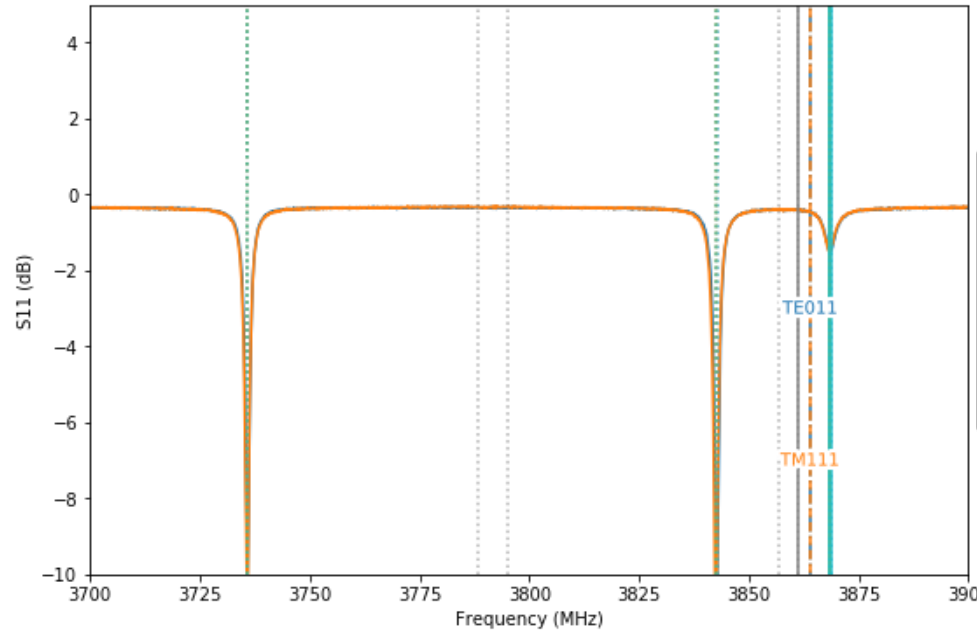


**(b)**

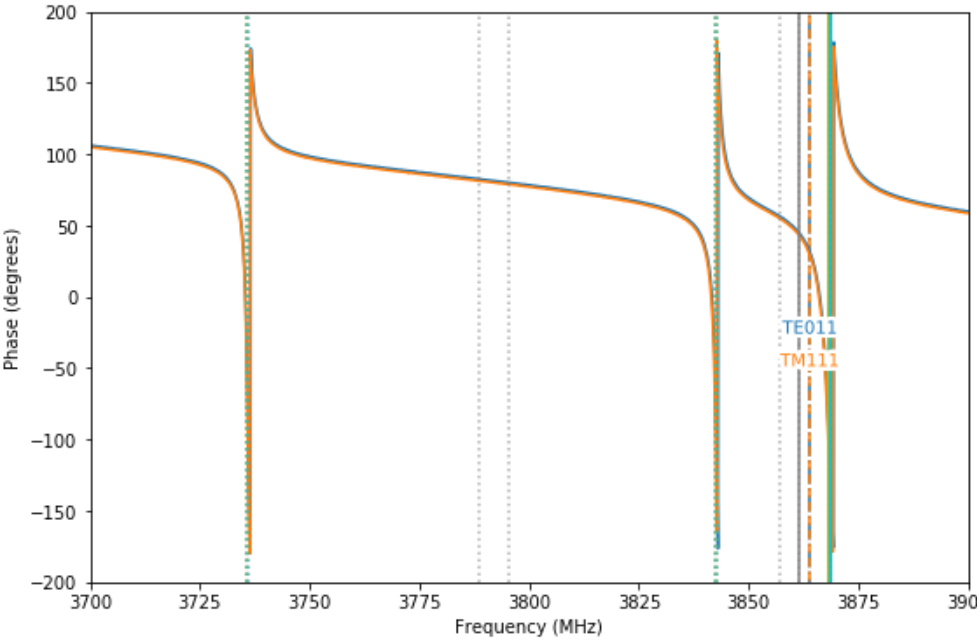


**Figure 4.1:** Different examples of resonance finding errors. **(a)** and **(b)** is the case where the magnitude peak finder (mag_peaks), which is the solid grey line, misses the $TE_{011}$ mode due to the peak being much smaller than the peak located on its left. The finder then incorrectly chose the $TM_{111}$ mode instead (solid grey line). The other two methods (solid blue and green line) choose the correct peak as they rely on the phase flip. This error was found by the author.

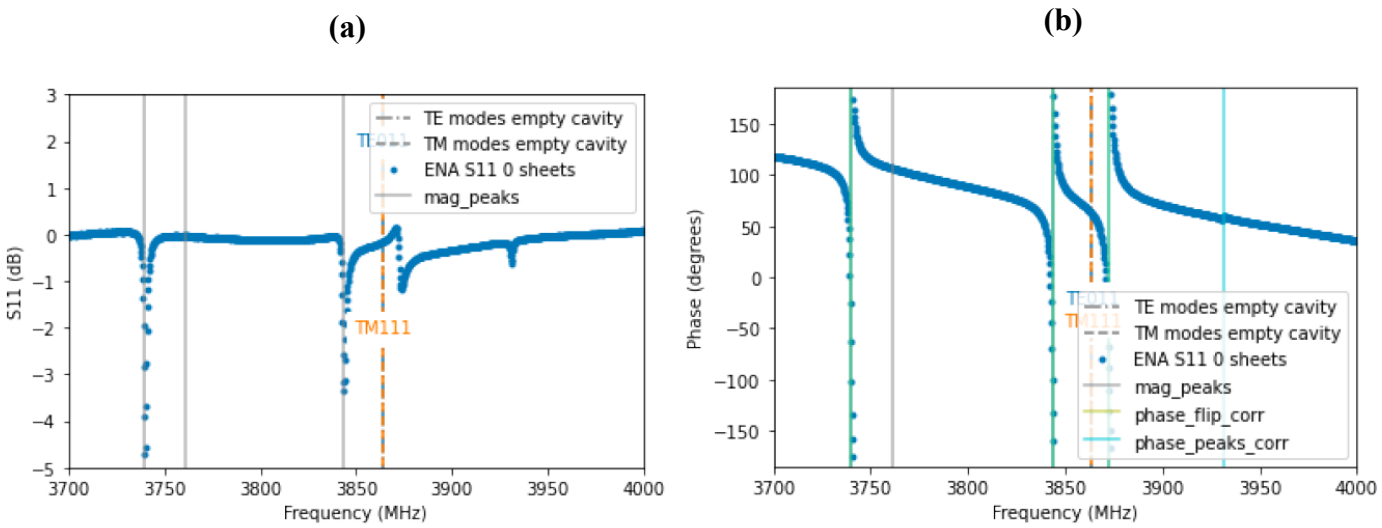


**Figure 4.2:** Second example of resonance finding errors. **(a)** and **(b)** is the case where the resonance dip shows up as a half peak, half dip. The magnitude peak finder misses this resonance peak entirely but the other two methods pick up on it. This error was found by E. Pieters [26]. These are just two of the more notable errors that can occur during resonance detection but most of the errors can be adjusted for by using the other peak finding methods or during analysis.

first is caused by the phase shift. At resonance, the $S_{11}$ parameter usually displays this via a sharp dip, but the accompanying phase shift can sometimes lead to this showing up as a peak instead. In these cases, the peak finder will miss the resonance dip as it shows up as a half dip, half peak. The other error occurs when the resonance dip we are interested in is much smaller than a dip directly adjacent to it (Figure 4.1). The peak finder will then incorrectly detect the $TM_{111}$ mode dip as the correct one leading to an error in the depth and width calculations.

**Deramped Phase Peak Finder**

The same Scipy signal function is employed again but first the phase is corrected to remove the phase ramp. The phase peak finder will therefore detect when the phase flips from -180 to +180

degrees only when the background phase is close to zero. This flip corresponds to the center of the phase change which is also the center of the resonance dip. The deramping is done by subtracting a 1D fit line from the data and then re-wrapping the data to fall within $\pm$180 degrees. This method works very well at detecting the dips the magnitude peak finder method might have missed so long that the phase flips cleanly from -180 to +180 degrees. In the cases where this does not occur, the finder will not detect the center of the dip but rather the peak on one side. It may also detect an entirely different peak which does not correspond to the resonance dip. This occurs when the $S_{11}$ parameter has ripples when it should be at zero post calibration. It was noted that using longer coax cables (~15ft) lead to a higher frequency of this error occurring therefore the cables used are short enough (>2ft) to control this problem [26].

**Deramped Phase Flip Finder**

The deramped phase flip finder performs the same deramping as the phase peak finder but rather than searching for the point where the phase flips, it searches for discontinuities in the phase which correspond to the flip from -180 to +180 degrees. This allows for the detection of dips the phase peak finder might have missed and it will also not detect any false dips due to ripples in the $S_{11}$ parameter. This method however will not detect any resonance dips if the phase change lacks discontinuity. Therefore, this method is least likely to misidentify a non-resonance dip as resonance, but it may miss the actual resonance dips of interest.

### 4.2.2 Data Analysis Calculations

As seen in Chapter 3, the depth of the embedded reflective surface can be calculated based on the resonance properties of the McGill reflectometer. The $TE_{011}$ mode was chosen as the mode to

track in order to calculate the depth. The `modecalculationsfunction.py` uses equations 3.1 and 3.2 to calculate the resonance frequencies for different TE and TM modes to create a library of resonance frequencies. Once the data from the VNAs has been inputted the analysis Jupiter notebook called `reflectometer_analysis_template.ipynb` will call the `reflectometerDepth.py`. This script is responsible for both the depth and width calculations along with all the plotting.

The width is calculated by taking the same resonance dips and calculating the full width half max (FWHM) of the peak via a fitting function on the dips. This leads to the Q factor:

$$Q = \frac{f_{res}}{\Delta f} \tag{4.3}$$

Where $\Delta f$ is the FWHM of the dip and $f_{res}$ is the resonance frequency. The Q factor provides information on the energy storage versus dissipation for a resonance. A higher Q factor means the resonance stores the energy better/longer. A smaller Q factor means the resonance will dissipate the energy faster or in fewer oscillations. This provides a method to study the resistivity of the imbedded reflective surface as changes in resistivity will lead to changes in the Q factor. This study will only provide Q factor measurements as absolute resistivity values require knowledge of the resistivity of the reflectometer's inner cavity walls.

The code is also capable of outputting some simple statistics such as the standard deviation and average of the depth for all different methods used to calculate it per folder. This presents a way to verify the accuracy of the measurements being taken (i.e., the shift in the resonance peaks observed during testing).

## 4.3 Depth and Q Factor measurement

The standard test that the reflectometer is used for is the measurement of the depth of the imbedded mesh for the dish samples. The metal mesh is an electrically reflective surface and acts as the enclosing wall for the reflectometer. As the distance of the reflective mesh must be as uniform as the surface of the composite material (sub-mm variance) the depth must be measured in different locations. Two dish samples were sent from the DRAO, both are made of a Stypol resin with a Dexmet aluminum mesh embedded with an E-glass of 1808x3 at 0/90° which is an extremely corrosion resistive fiber glass. The degrees refer to the direction the fibres are pointed in, and the fibers are not woven. The mesh is an expanded metal which is later leveled but not flattened. The metal thickness is approximately 0.127 mm with an overall thickness of 0.152 mm. There is approximately 60% open space with the grid being diamond shaped rather than traditional squares. The first panel (referred to as the C-Glass veil from here on) is made of a Freudenberg (C-glass) veil (T-1777 26gsm) and the second panel (referred to as the Pearl veil from here on) is a Pearl veil (SCH 110-23) (see Figure 3.2). Once the VNA is calibrated, the reflectometer is connected to port 1. The reflectometer is placed on the veils in four separate locations, each time picking up and replacing the reflectometer but being sure to place the reflectometer in a similar position with respect to the cable direction. Four sets of data points are taken per veil and the test is performed several times on different days. The data sets are uploaded into the reflectometer code and the depth of the imbedded mesh is calculated along with the Q factor of the veil.

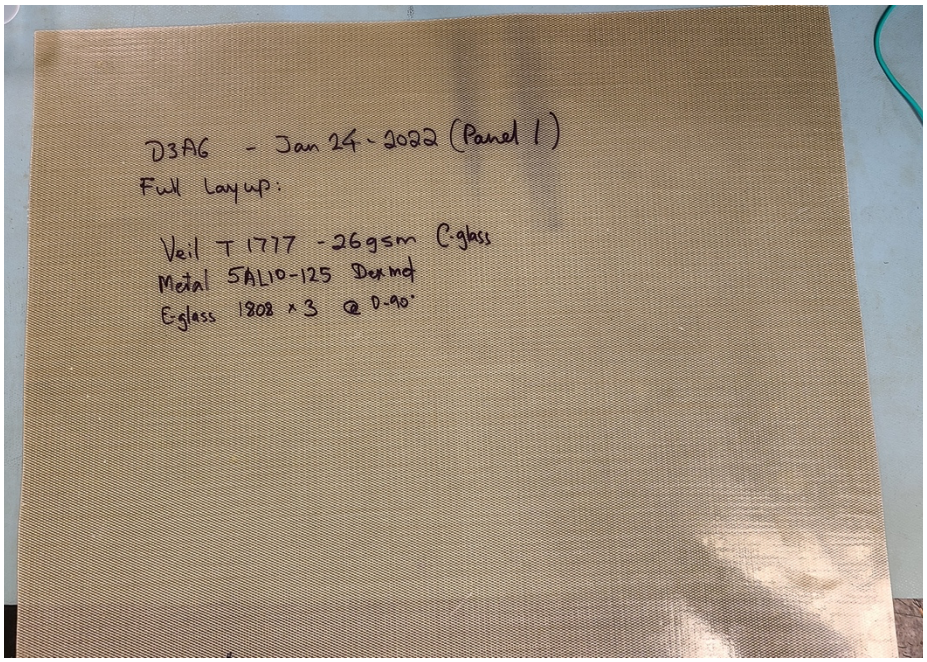


**(a)**

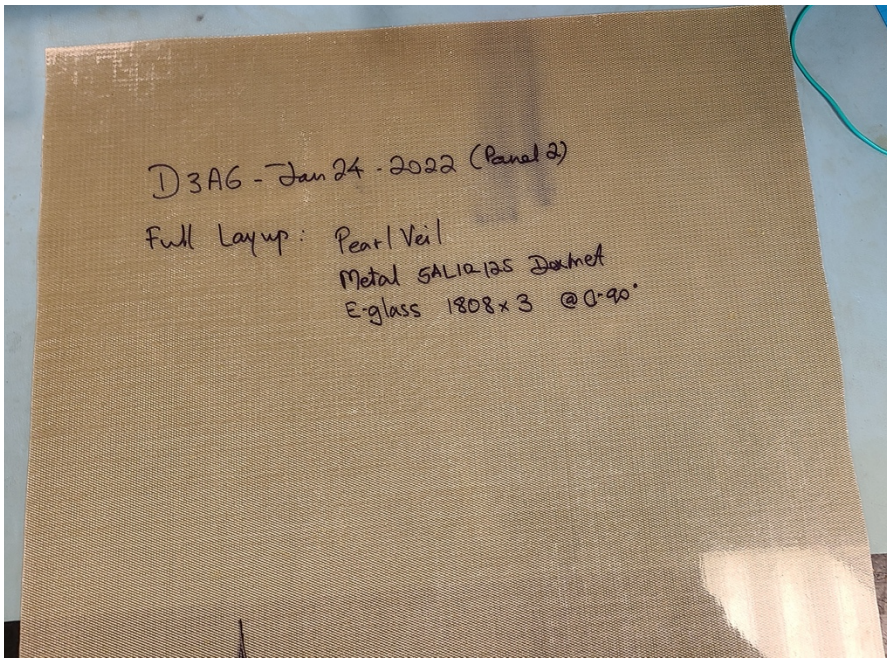


**(b)**

**Figure 4.3**: **(a)** C-Glass veil sample and **(b)** Pearl veil sample. Both have their respective specifications written on smooth resin side which is the exposed side of the dish and the side in contact with reflectometer. Both veils are 51x46 cm.

## 4.4 Calibration Test

Using a flat sheet of metal that makes direct contact with the reflectometer, the calibration test is completed for both types of VNAs. To start, the VNA is calibrated, and the calibration set is saved. The reflectometer is placed on the sheet of metal and the results are saved. Four data sets are taken each time lifting the reflectometer up and placing it back in the same location and same position. The VNA is then power cycled, and the saved calibration set is re-loaded. The reflectometer takes another four points on the same sheet of metal at the same location as before. The VNA is then power cycled again but this time it is recalibrated. Four data sets are taken again. The VNA is recalibrated once more, but no power cycling is done between these tests. The last four data sets are taken on the metal sheet at the same location. For comparison, four data sets are taken without any calibration immediately upon power cycling the VNA. All tests must be completed in one go meaning it must be conducted with no breaks between the tests. On a different day, another set of data is taken on the same metal at approximately the same location, but the VNA will use the saved calibration set from the first day of testing. For comparison, testing will also be done using a new calibration by power cycling the VNA and recalibrating it before testing the same metal sheet. The last two tests should be conducted in one go as well. For the ENA the Cal Set can be saved directly to the ENA, for the Fieldfox the state and trace is saved to a USB and re-uploaded when the re-loaded tests are being conducted. On both days, the same cable was used to ensure the re-loaded calibration would be under the same conditions as the previous day.

## 4.5 Changes to Testing Environment

The material present beneath the veils has an impact on the results obtained by the reflectometer. In order to gauge the effect, a set of tests were conducted changing the material beneath the veils. To begin, the veil is placed on the tabletop in the lab with the rubber mat beneath the veil in order to reduce conductivity. The reflectometer is placed on top of the veil in four different locations being careful to ensure the orientation of the reflectometer is maintained between tests, meaning the direction the antenna is facing with relation to the flow of the veil. The cable is also kept as straight as possible to avoid any bends in the wire. Next the aluminum sheet is placed under the veil and the reflectometer collects another four data sets. Lastly the veil is placed on a lift in order to simulate the dish being in the air. The lift (Figure 4.3) is 10 inches (25.4cm) in height and is 51x46cm wide which is the approximate size of both veil samples. The lift was built out of medium density fiberboard (MDF) and construction grade glue by the author. No nails or screws were used to avoid any possible conductive material effecting the data the reflectometer would take. The veil is placed resin side up and the reflectometer is placed on top of the veil. The same four data points are taken, again being careful to maintain the orientation of the reflectometer from the previous tests as closely as possible. The entire test is conducted in one day. The tests are conducted using the Fieldfox alone as the lift and the length of the cable restricted the movement of the reflectometer when it was connected to the ENA. All tests are conducted for both veil samples and the same wire was used throughout.

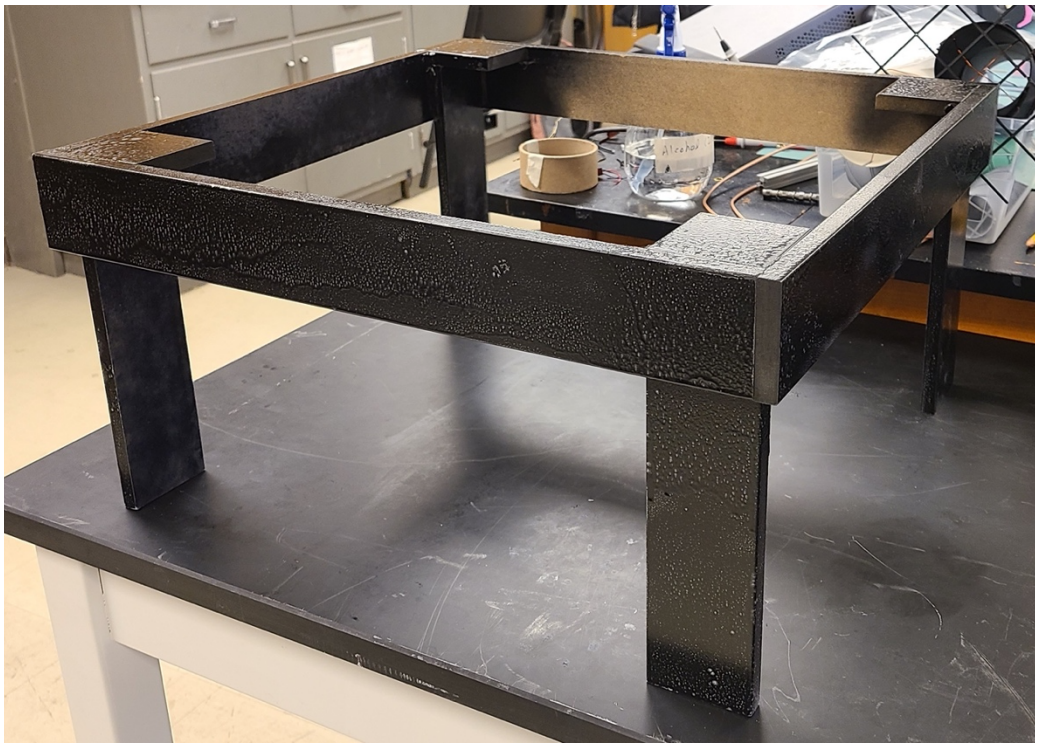

**(a)**


**(b)**

**Figure 4.4: (a)** The lift used for the veils. It has four corner squares to support the veil and ensure it remains flat. The lift has no metal and is made entirely out of non-conductive materials. **(b)** The lift with a veil placed on top. The lift dimensions are 51x46x25.4 cm.

# Chapter 5:

# Results and Analysis

Based on the test protocols described in Chapter 4, the results for the depth and resonance behaviour will be presented. The first results presented in section 5.1 will be the basic measurements taken with the reflectometer on either the aluminum sheet or the two dish samples. This will introduce the issue of the change in results seen from day-to-day as well as provide an understanding as to how the reflectometer results vary from the ideal/theoretical case seen with the CST simulations in Chapter 3. The calibration and environment tests follow in section 5.2 and 5.3 respectively and are used to try and determine if the changes are caused by a single issue or if there are multiple factors which make these daily changes more significant. These daily changes were not large enough to affect the confidence in the depth measurements presented but the changes did present a significantly larger variance for the Q factor results. Lastly, an extra test about the placement of the reflectometer with respect to the direction of the embedded metal grid is added in section 5.4. This test was not initially planned but results from other tests lead to additional in order to study the effect the rotation of the reflectometer had on the results. This chapter will delve into the possible causes for the changes observed and will describe the improvements done to the measurement process that yielded more consistent results.

All data presented in Chapter 5 was taken by the author along with the undergraduate student L. Gonzalez Escudero. The tests presented in sections 5.2 to 5.4 were original tests conducted for the first time. The original depth measurements test protocol was designed by E. Pieters, but the width and Q factor measurements are new variables added to the analysis code and measured for

the first time. The characterization of the dish prototypes received are new measurements conducted by the author and L. Gonzalez Escudero. The original tests conducted by E. Pieters using bare metal or sheets of paper were used to determine the measurement error and calibration data for the reflectometer. Values found using the new data presented below are compared to the values obtained by E. Pieters.

## 5.1 Depth and Q Factor Measurements

We calculated the depth and Q factor for all tests conducted. We collected many datasets, allowing us to carry out a detailed comparison on how the depth and Q factor vary between testing days. We begin by presenting the aluminum calibration data and afterwards the D3A(6) dish sample measurements. The aluminum sheet acts as a direct enclosing wall, therefore it is used to calibrate the data. This step is important as any shift from zero must be included before beginning testing on the veil samples.

The code presented in Chapter 4 has many debugging parameters added so that the user may generate extra plots. These plots are used to help determine what exactly the peak finder methods are detecting as the correct resonance peak. As the data would sometimes present a large difference in the depth calculated by different peak finder methods the plots help determine which finder method is not choosing the correct resonance peak. As we can adjust the initial search parameters to look in specific ranges of frequency as well as the depth of the peak in dBs the plots were used to adjust the constraint values. The DEBUG plots for the magnitude peak width finder were put to true as this specific debugging plots allowed for comparison between the width results and the actual resonance peaks from the $S_{11}$ data (Figure 5.1). These plots are

then used to ensure that the magnitude peak finder identified the correct peak to use to calculate the depth and Q factor.

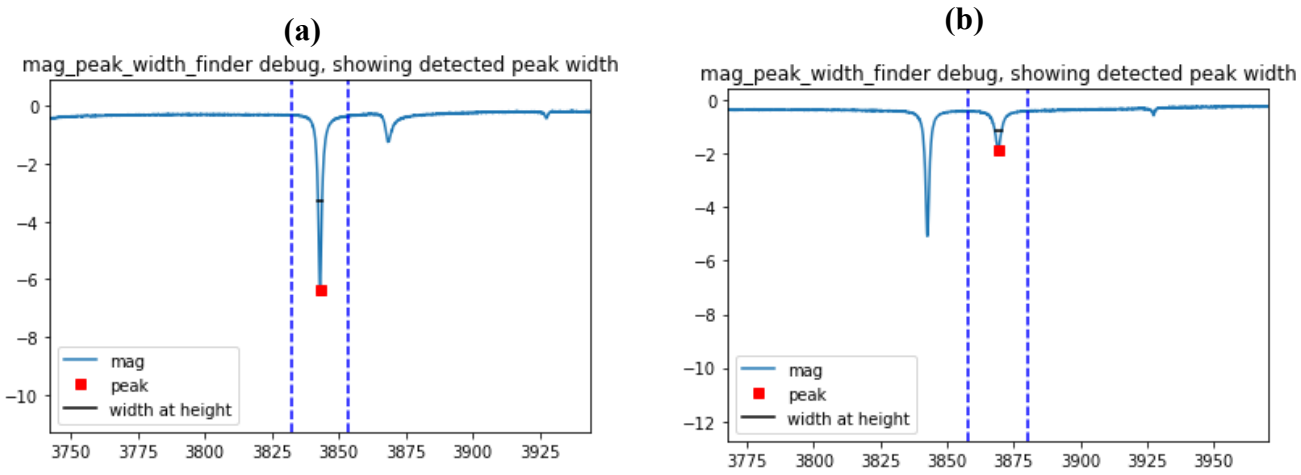


**Figure 5.1:** DEBUG plots showing the misidentification of the resonance mode. **(a)** has the magnitude peak finder choosing the $TM_{111}$ mode whereas **(b)** shows the finder selecting the correct resonance dip. These DEBUG plots were used when the depth values produced were very different from the expected range to confirm if the correct mode was chosen. The starting parameters used when model fitting are carefully chosen to ensure the peak finder choses the $TE_{011}$mode but sometimes they are not constrained enough so the DEBUG plots help with the further constraint of these variables. The x-axis provides the frequency and the y-axis the magnitude in dBs.

### 5.1.1 Aluminum Base Results

Starting with the calibration data, the depth test was conducted using the aluminum base with two different length coaxial cables to see if the cable length had an effect on the results. The results presented all used the Fieldfox. There were two coaxial cables used for the calibration; a 26 cm long cable labeled “short”, and a 57 cm long cable labeled “long”. The longer cable is not so long that we risk introducing the $S_{11}$ ripples issue mentioned in Chapter 4. The $TM_{111}$ peak is much stronger than the $TE_{011}$ for the aluminum sheet therefore careful consideration must go into starting parameters to ensure correct mode is identified.

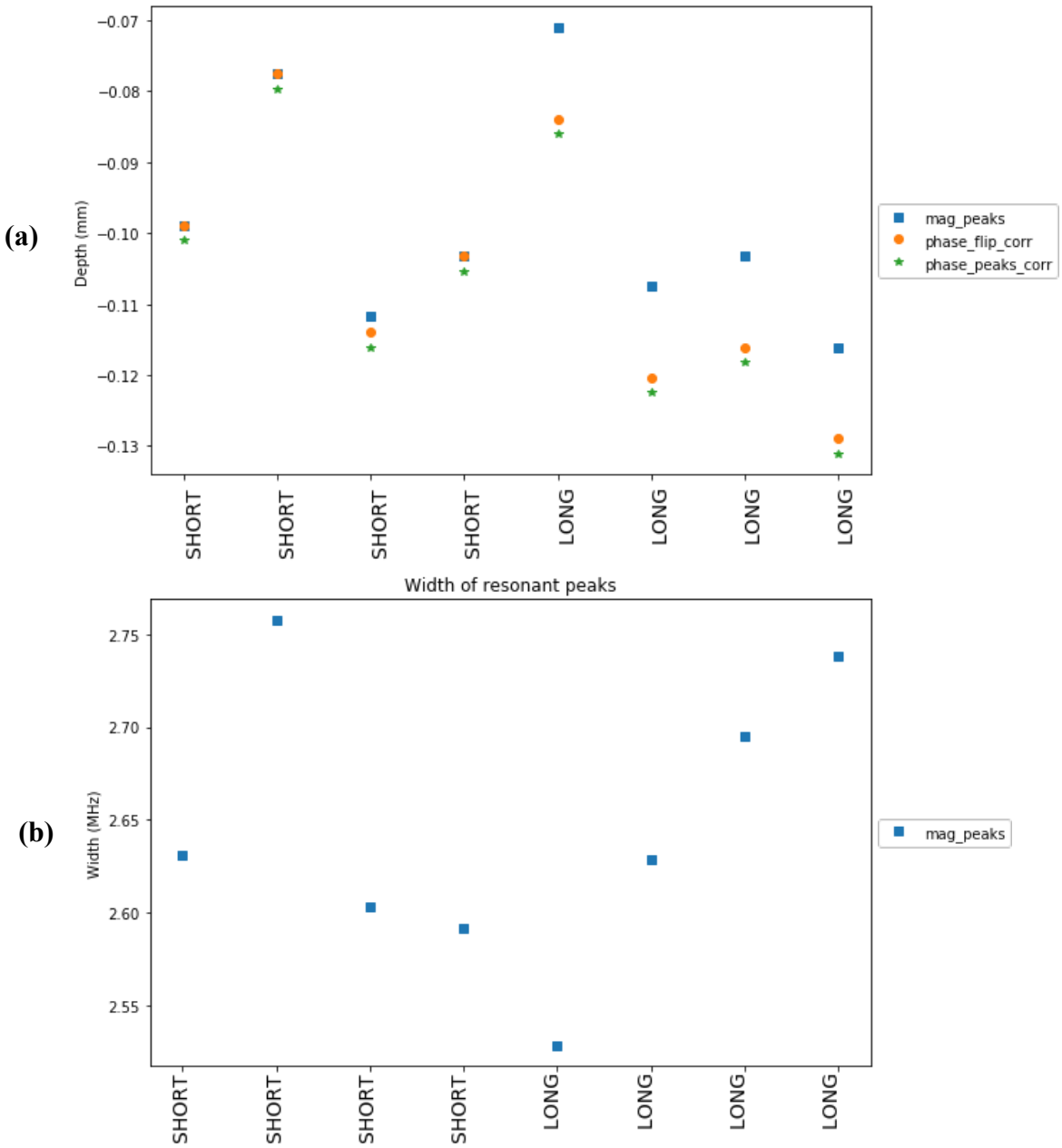


**Figure 5.2:** Depth calculation and width measurement for the sheet of aluminum using a short (26 cm) and long (57 cm) cable via the Fieldfox. **(a)** is the depth calculation and **(b)** the width measurement. The measurements for each wire were conducted in the same day one after each other. The reflectometers' location on the metal sheet was maintained between measurements. The x-axis labels the measurement point with either short or long depending which wire was used. Although the short cable appeared more consistent than the long for these results the short cable encountered issues producing consistent results between different testing days. This problem, presented in Figure 5.3, meant that the short cable could not be used for testing.

The two cables were tested to see if there was a noticeable difference in the results produced in a single day and over different testing days. In total three datasets were collected with the short and long measurements completed one after the other to avoid any daily variance being introduced. The data presented in Figure 5.2 was taken on September 29$^{th}$ 2022 and the other two data sets were taken on September 27$^{th}$ and October 12$^{th}$.

The two cables had very similar results in that the depth calculation did not change too much between cables with a standard deviation of 0.017 mm for the long cable and 0.013 mm for the short cable (Figure 5.2). The average depth for the three testing days was -0.128 mm for the short and -0.106 mm for the long. The absolute mean difference between the two cables across all three measurements was no greater than 0.03 mm which is consistent with measurement error. After a few runs with the short cable, we noticed that the short cable was starting to produce resonance peaks that were very different from the other runs (Figure 5.3). This could be seen as a decrease in all the resonance peak's amplitude by such a large amount (magnitude was smaller than -1 dB) that the magnitude peak finder could not even detect the resonance peak no matter the initial search parameters set. As the other finder methods rely on the change in phase, they could still decern a resonance peak but the peak being so much smaller than what was normally seen resulted in no width measurements. Since the short cable was not producing consistent results between days as well as the fact that the longer cable allowed for easier manipulation of the reflectometer when it was connected to the ENA, the short cable was eliminated.

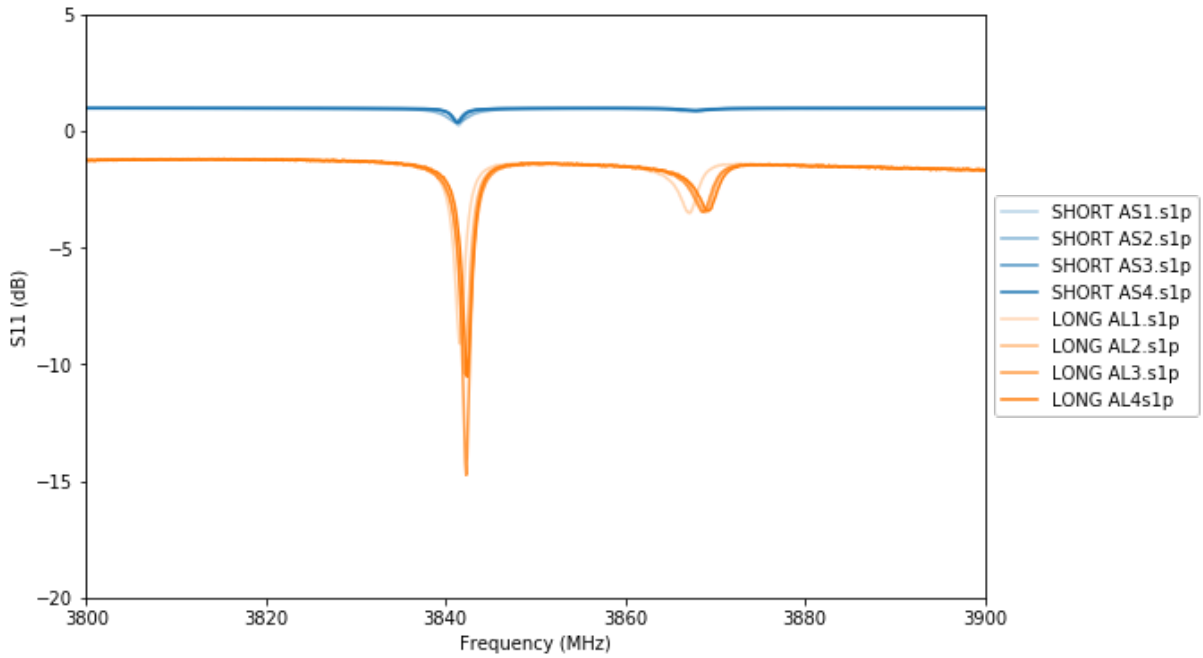


**Figure 5.3:** Comparison of the $S_{11}$ for the short and long cables while calibrating against aluminum. The blue sweeps are the short cable measurements, and it displays an overall decrease in both TE and TM mode peaks. The $TE_{011}$ peak is so small in fact the magnitude peak finder could not detect it. As the magnitude peak finder is what we use to measure the width, the Q factor could not be calculate for these data sets. Due to the unreliability of the short cable and the fact that the long cable made for easier manipulation of the reflectometer when connected to the VNA's we stopped using the short cable for measurements.

With the long cable being chosen as the permanent testing cable we could now proceed with the aluminum base tests. These datasets provided a better understanding on how the reflectometer's resonance cavity behaves when it is in direct contact with an enclosing wall. It was vital we understood this behaviour before conducting any depth measurements for the dishes as the reflectometer's zero-depth frequency was slightly shifted from the analytic calculation due to real effects such as the antenna. The calibration is conducted to determine the value for that shift.

The measurements are presented with uncertainties calculated using the standard deviation for the whole dataset. This was necessary as the standard deviation for the daily results is not very large but there is a greater change in measurements seen between different testing days. The uncertainty is calculated this way for both the depth and Q factor measurements. The data set presented in Figure 5.4 and 5.5 shows the summary of the measurement results collected over five different days. It was found that the reflectometer has a slightly negative value when placed directly against the conductive surface with a value of -0.09$\pm$0.02 mm. The three different methods had slight differences in the calculated depths, but the variations were on the order of $\pm$0.01 mm per day meaning there was no need to eliminate any of the methods for miscalculation or misidentification of the $TE_{011}$ peak. The aluminum sheet tests were repeated with the ENA to see if any difference was observed between the VNAs. Datasets were collected on three separate days, again four measurements per day. The data was still slightly negative with a value of -0.10$\pm$0.02 mm (Figure 5.6). There were less data sets taken with the ENA compared to the Fieldfox, but the absolute zero-depth found for the ENA was not a big enough difference from that found with the Fieldfox to cause concern that one of the VNAs was introducing a measurement error. Overall, the results for the two VNAs depth results were similar enough that we can continue using both of them.

Day to day measurements would occasionally present a value for the shift larger than the -0.09 mm average for the Fieldfox and -0.10 mm for the ENA. This difference is partially related to the measurement precision when using the VNAs. As seen in the figures thus far, there was not a large change between data points for the same finder method (on the scale of 0.02 mm or less). Therefore, comparing different day results is the best way to approximate the measurement

precision. This value must be small enough to ensure that the surface variation tolerance set by CHORD/HIRAX can be met ($\lesssim$0.1mm). The largest change in depth seen for the aluminum measurements was -0.14 mm with a daily average of 0.11 mm for that entire data set while using the Fieldfox (the data marked September 29$^{th}$ in Figure 5.4). This value only appeared in one data set indicating that there may have been an issue with that specific measurement (such as coaxial cable not secured tightly enough). For the ENA, the maximum value seen was -0.13 mm but there was a large difference in time from when the first two measurements were taken and as can be seen for those results (labeled February 28$^{th}$ in Figure 5.6) there is little variance over the whole dataset making it unlikely that measurement error led to this value. Overall, the rms scatter results did not change by more than 0.05 mm from day-to-day for tests conducted with both the Fieldfox and ENA. Therefore, the measurement precision is $\lesssim$0.05 mm which is small enough that the dish uniformity results will not be adversely affected. This is consistent with the precision level found with previous measurements which compared the measured results for the reflectometer placed on a painted metal sheet using the Fieldfox to the calculated CST results [26].

While testing the measurement precision, the noise estimate on the resonance frequency peak position was also calculated. This was not done by comparing day-to-day measurements since the variation in measurements between different testing days can be larger than the noise value itself. Instead, the measurements made on the same day while maintaining reflectometer position and direction were compared. For both VNA's, four measurements were taken per data set during the calibration testing done over different days. For the Fieldfox, the resonance frequency peak position had a noise value of $\pm$0.50 MHz on average with a maximum noise value of $\pm$0.90

MHz and a minimum of $\pm$0.05 MHz. For the ENA, the noise values were even smaller with an average of $\pm$0.09 MHz and a maximum noise value of $\pm$0.15 MHz. For both VNA's, the results appear to be roughly consistent with a single noise. As the ENA is the more precise VNA it is expected that the noise estimate for the ENA would be better than that found with the Fieldfox. Since the Fieldfox is a handheld device, there maybe be more noise during sweeps compared to the ENA, but the noise estimate on the Fieldfox is not high enough to cause concern for the depth calculation accuracy. For this reason, the Fieldfox will continue to be used during testing along with the ENA.

The final measurement checked before moving on to the veil measurements was the variance in the width. Overall, the width values for the aluminum sheet fell between 2.50-3.00 MHz for the Fieldfox and 2.75-3.10 MHz for the ENA. This change in width results in a Q factor range between 1320 – 1500 for the Fieldfox and 1280 - 1410 for the ENA. This range in Q factor values is large enough that should this variance appear in the dish measurements, it will be difficult to comment on the resistive behaviour of the embedded mesh. For this reason, it is important to further investigate what factors might be impacting the change in the width of the resonance dip. As the results for the VNAs are consistent to better than our measurement tolerance we can continue to use both VNAs for the next section of testing.

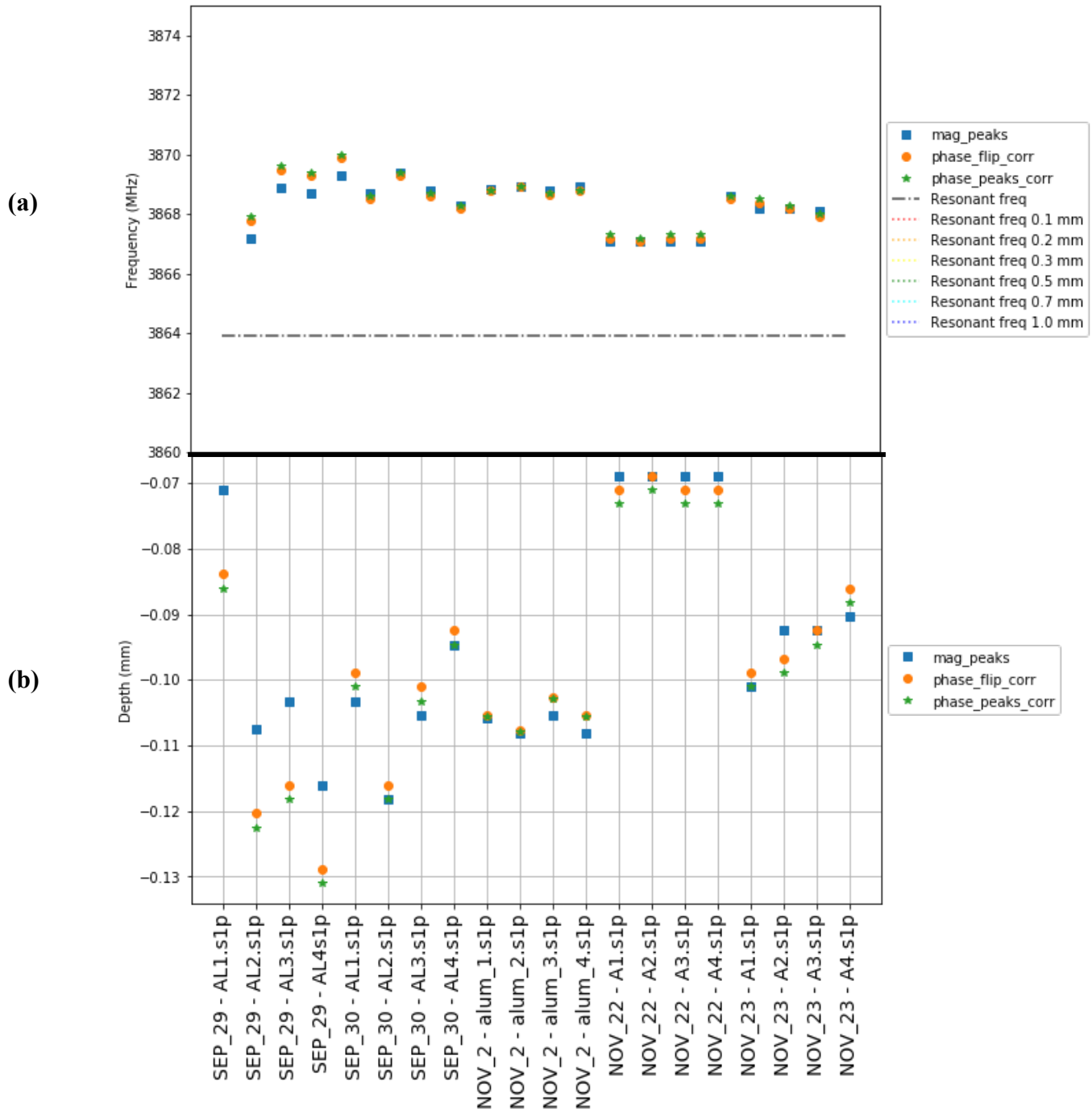


**Figure 5.4:** Data from a test where the reflectometer is placed directly against an aluminum sheet using the Fieldfox. The x-axis is the individual test points where the reflectometer is replaced in the same location four times. **(a)** Identification of the resonance frequency with the expected resonance frequency for the cavity (the $TE_{011}$ mode) marked as the horizontal grey dashed line. **(b)** The calculated depth of the aluminum sheet. The shift of approximately -0.09 mm from the absolute zero-depth can be seen.

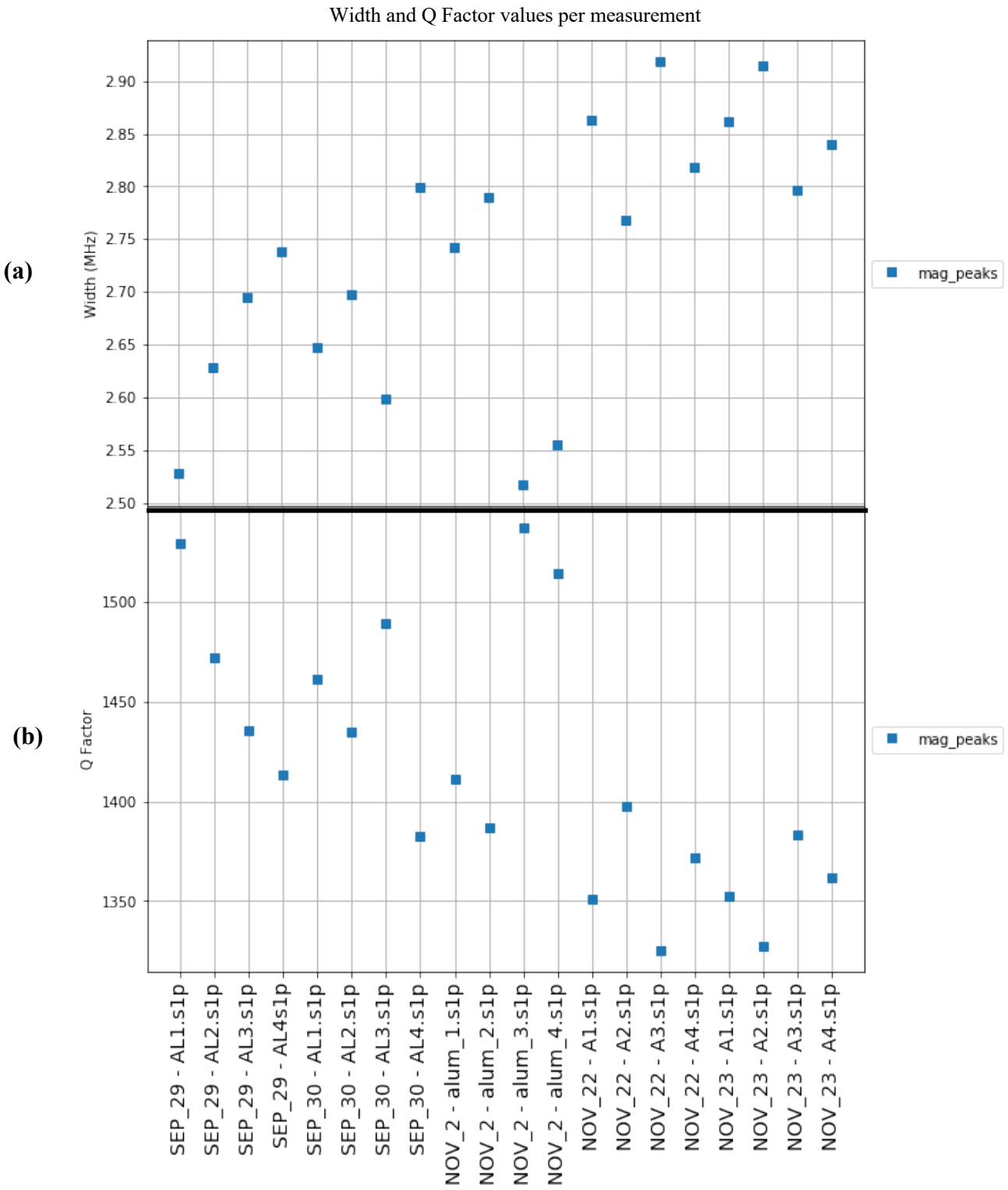


**Figure 5.5:** Data from a test where the reflectometer is placed directly against an aluminum sheet using the Fieldfox. The x-axis is the individual test points where the reflectometer is replaced in the same location four times. **(a)** and **(b)** are the width of the resonance peaks along with the corresponding Q factor value respectively. A larger variation is present for the width and Q factor compared to the depth.

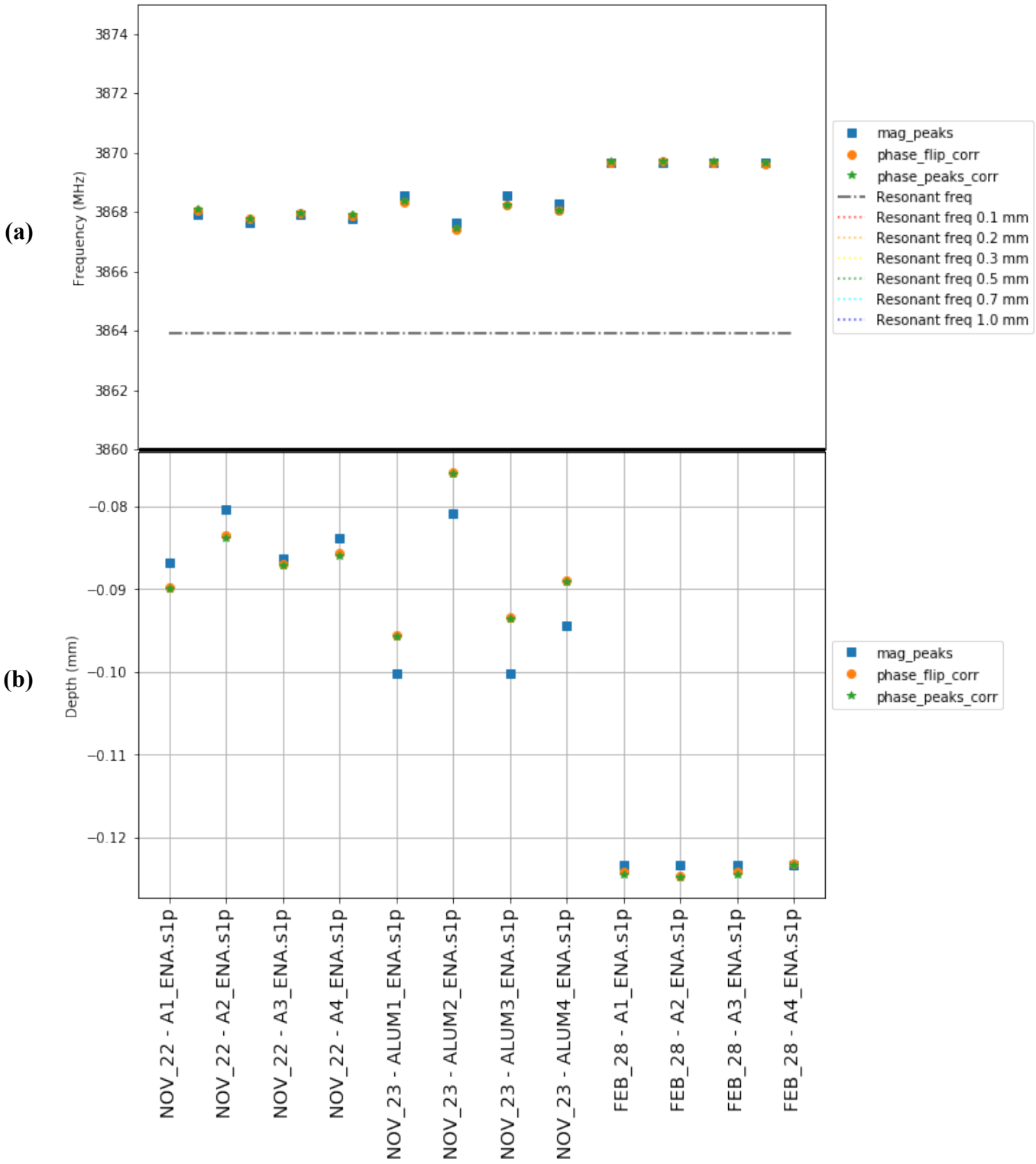


**Figure 5.6:** Data from a test where the reflectometer is placed directly against an aluminum sheet using the ENA. The x-axis is the individual test points where the reflectometer is replaced. **(a)** Identification of the resonance frequency with the different resonance mode frequency per depth calculation are marked with the dotted horizontal lines. **(b)** The calculated depth of the aluminum sheet. The shift of approximately -0.10 mm from the absolute zero-depth can be seen.

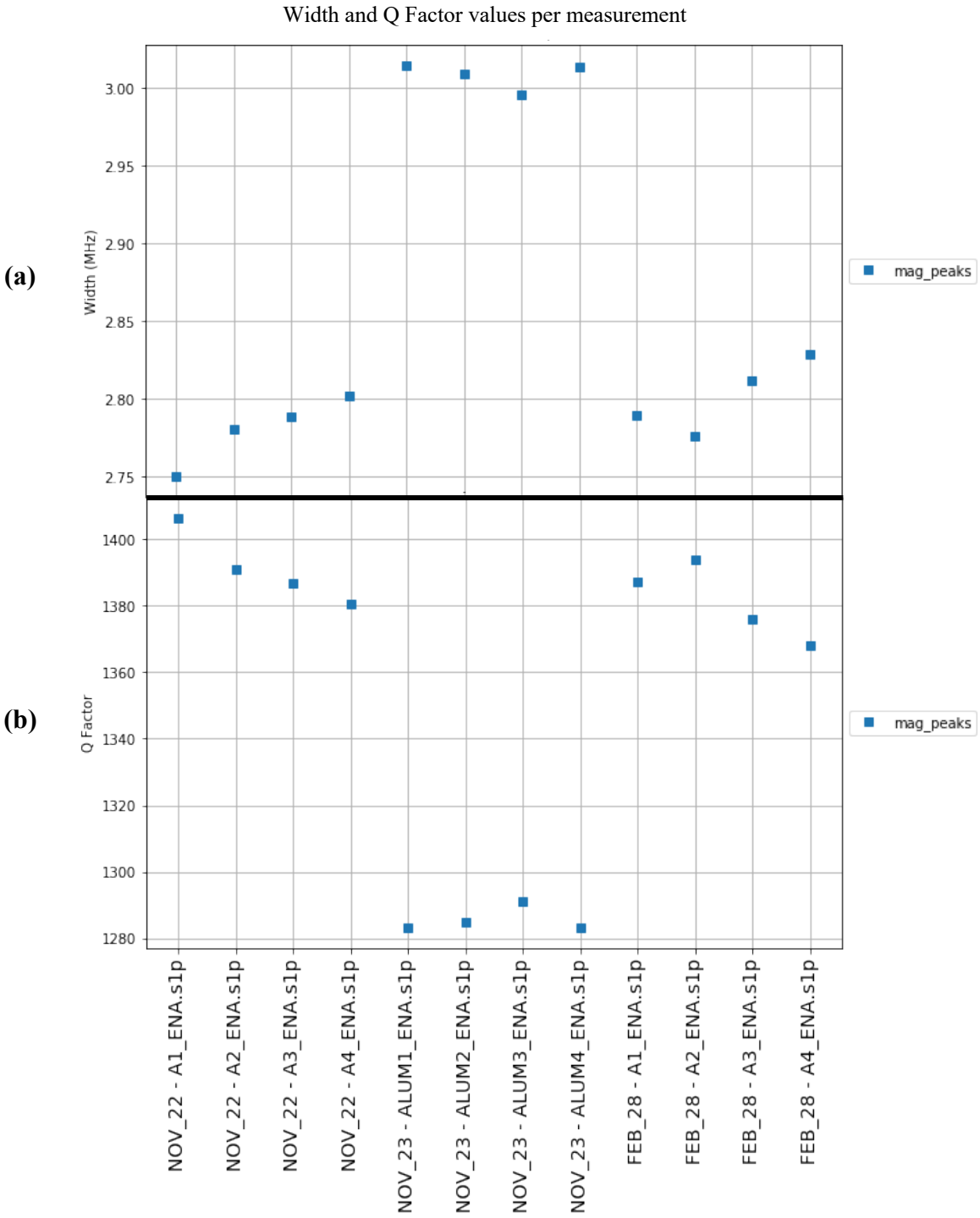


**Figure 5.7:** Data from a test where the reflectometer is placed directly against an aluminum sheet using the ENA. The x-axis is the individual test points where the reflectometer is replaced. **(a)** and **(b)** are the width of the resonance peaks along with the corresponding Q factor value. The test was conducted with the ENA to compare the differences seen between the VNAs. If one of the VNAs had produced a noticeable difference in the variance for the width and Q factor results that could mean that the VNA is possibly causing this variance. Results between the two VNAs are consistent to within the measurement tolerance therefore we will continue to use both.

### 5.1.2 D3A Dish Sample Results

The dish samples sent by the DRAO were tested in order to measure the embedded depth as well as assure the variations within the composite material are within tolerance. The data was reported to the DRAO to help in the decision on which material to proceed with for the construction of the six-meter dishes. There were several data sets taken with both VNAs in order to compare and ensure the day-to-day changes seen thus far did not affect the presented results too strongly. We first begin with the results (both depth and Q factor) obtained with the Fieldfox and later compare this to the results gathered with the ENA. Before discussing the results of the measurements, it is important to understand what Q factor range we are hoping for. As the dish is supposed to be made with a material that is low in resistive loss, we expect a high Q factor value. For a microwave resonator a high Q factor is expected to fall in the $10^3 - 10^4$ range [33]. If the Q factor were to fall below this range that would mean that the material acting as the enclosing wall has a higher resistive loss also called an overdamped system. As losses in the dish correspond to an increase in system noise temperature, a variable we hope to reduce as much as possible, the Q factor can provide an estimate of how much loss we can expect.

The depth results using the Fieldfox were quite consistent over all datasets. There were five different testing days with each day taking the measurements one after the other to avoid introducing any changes. Over these testing days, we expected the results to remain consistent since the properties of the veil remain the same and so do the testing protocols. This is the behaviour seen for the depth measurements, but this does not extend to the width value and Q factor. A small amount of change in those variables is always expected due to measurement accuracy and noise scatter but the daily changes seen are larger than expected. The average depth

across measurements for the C-Glass veil was 0.30 ±0.01 mm and the Pearl 0.44 ±0.03 mm. These values are adjusted to take into account the shift of -0.09 mm calibrated zero-depth therefore the values for these depths on the graphs will be lower (Figure 5.8 and 5.9). The values for the standard deviation of depth varied slightly for different data sets. The largest change in depth was seen for the Pearl veil where there was a 0.10 mm change between two data points (a single step) and a result of 0.035 mm rms for the data set. This was by far the largest change in depth seen for the Pearl veil with the other data sets all having variations no larger than 0.05 mm and a standard deviation between 0.019 – 0.025 mm rms. The values for the C-Glass veil were always smaller than that of the Pearl. The largest variation between data points was 0.05 mm with a standard deviation between 0.006 – 0.016 mm rms. The standard deviation values fall well within tolerance for both veil types. There was no set minimum or maximum embedded depth set by HIRAX or CHORD therefore the depth values presented are allowed. Since both veils pass the tolerance check, analysis of the width and Q factor can proceed.

The values for the width varied much more than the depth. Values for the individual data sets did not vary more than 0.5 MHz but, overall, the width values were between 1.95 and 3.65 MHz. This correlates to a variation in Q factor between 1060 and 1960 approximately. There was no discernable trend or difference seen between the width values for the Pearl veil versus the C-Glass veil (see Figure 5.8 and 5.9). The Q factors are also similar in that there is no observable difference between the C-Glass and Pearl veils. This is the expected result as both veils use the same type of aluminum (a Dexmet) for its embedded mesh meaning the resistive properties for each veil should behave similarly. The surface of the composite material is the only different between the two dishes. Although this material is non-conductive it still has a non-zero dielectric

constant meaning it can still affect the resonance behaviour. Due to this fact, we do not expect the Q factors to be identical between the two veils but very similar. It is difficult to precisely comment on the resistive nature of the embedded mesh as the Q factor results vary over a large interval. The Q factor being quite high does mean that the resonance is good at storing energy. This again is ideal as a high Q material is a more conductive material and that is the goal for the dish material since we want to reduce resistive losses in the dish. For this reason, Q factor is a useful quantity to study as we can assure that the radio signal will not be overdamped by a more resistive reflective dish and therefore alter the signal the antenna receives. Before we can confidently comment on the resistive nature of the embedded mesh, the results for the Q factor should be more consistent over the different daily tests (at least a change of less than 500 between testing days). More measurements will need to be taken once a stricter set of testing practices has been determined via the troubleshooting tests since we should then have a more consistent and smaller range for the Q factors. Before this can occur, we will first see if there is any improvement in the results when we use the ENA instead.

The measurements for both depth and Q factor were repeated twice using the ENA for comparison. The values for the depth were a bit higher compared to the Fieldfox with an average value of $0.47 \pm 0.02$ mm for the Pearl veil and $0.34 \pm 0.01$ mm for the C-Glass. A possible reason for the difference in depth values could be due to the ENA having a higher resolution. The ENA has more sweeps per second and a higher power output. This leads to higher precision in the data taken which has led to the depth values being larger than those taken with the Fieldfox. The precision continues with the values for the standard deviation as the results were also more

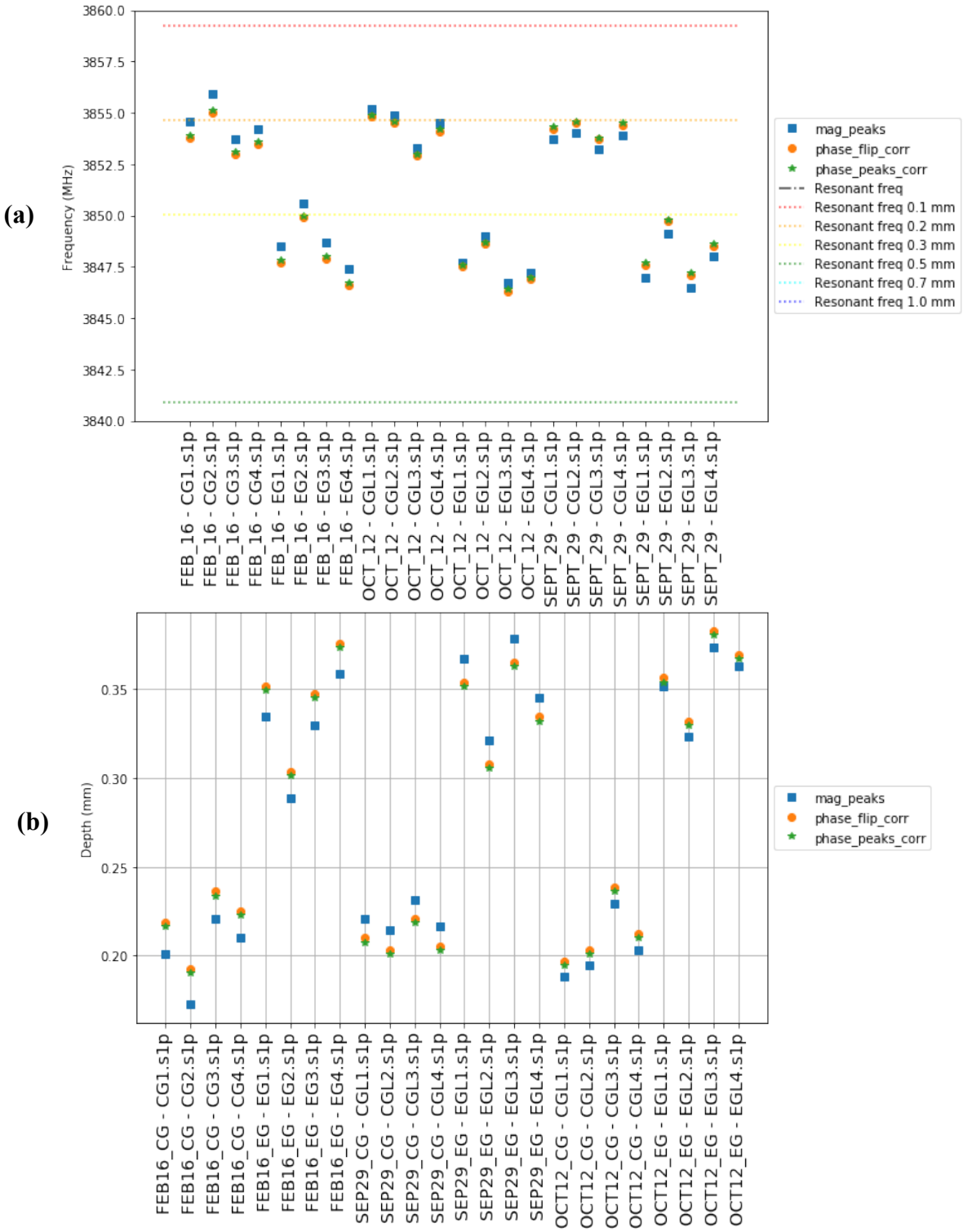


**Figure 5.8:** Data sets taken with Fieldfox. Results for the Pearl and C-Glass veils with an average depth standard deviation of 0.022 mm and 0.013 mm respectively. The CG label refers to the C-Glass veil and the EG the Pearl. **(a)** shows frequency location of the $TE_{011}$ resonance peak for both veils with the horizontal dotted lines representing the different calculated resonance frequencies depending on the embedded depth. **(b)** shows the calculated values for the depth. The depth change falls within the tolerance set by CHORD/HIRAX meaning both veils are acceptable prototypes.

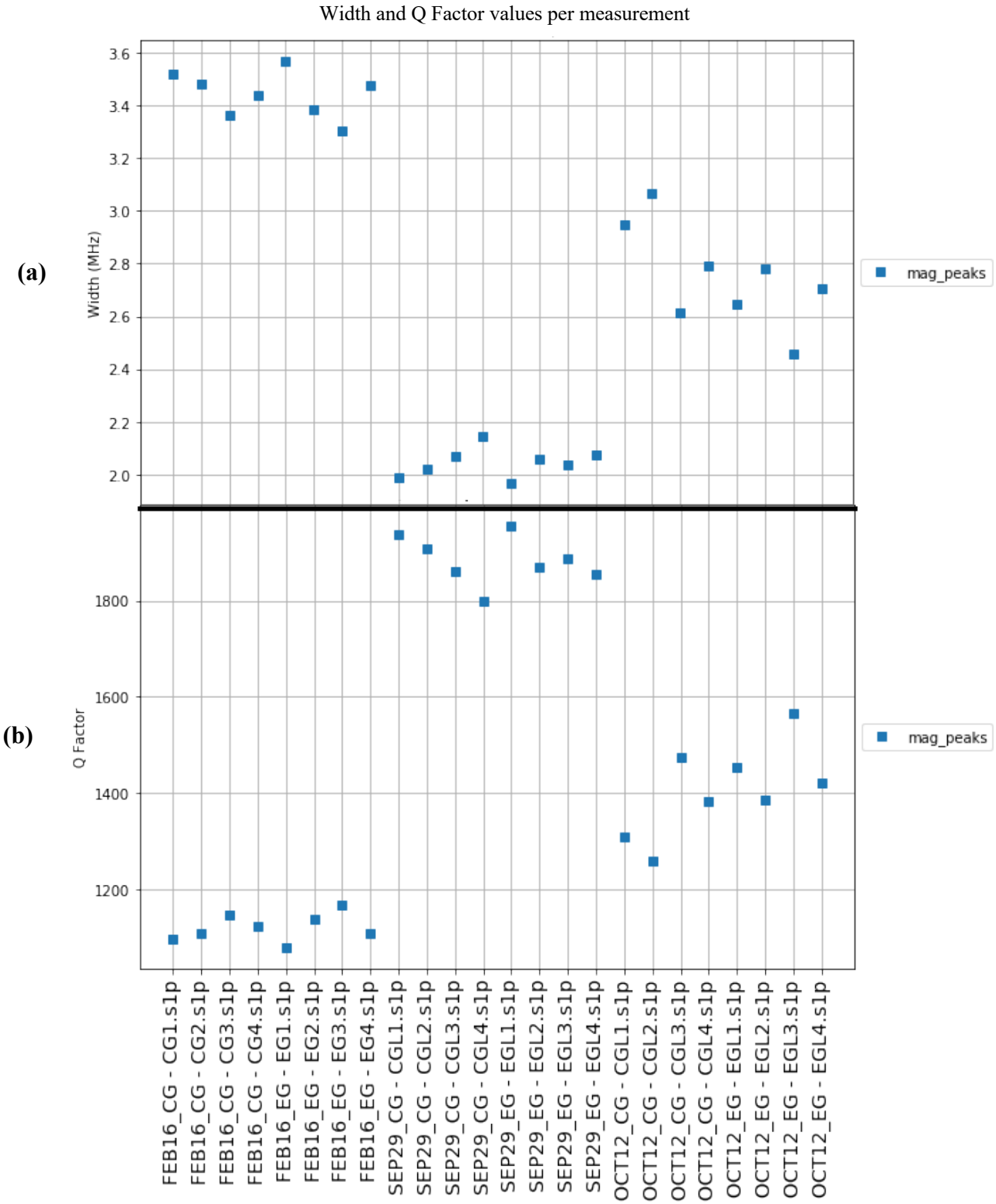


**Figure 5.9:** Continuation of the data sets taken with Fieldfox. The CG label refers to the C-Glass veil and the EG the Pearl. **(b)** shows the calculated values for the Q factor and **(a)** the measured width of the peaks. These data sets include the highest Q factor of 1960 as well as the lowest of 1060 approximately. The resistive behaviour is similar which is expected as they both are made with the same aluminum mesh.

consistent between the two veils. The standard deviation for both veil types fell between 0.012-0.025 mm. With the ENA, the variance range was smaller but neither veil was consistently better than the other. The width values had a bigger difference as the peaks at the $TE_{011}$ mode were much sharper leading to a smaller FWHM (see Figure 5.10, 5.11 and 5.12). The width results were between 1.7-2.2 MHz for both veils which gives an approximate range of 1750-2200 for the Q factor. The range of data points is not as large as that found with the Fieldfox. This is partially due to the fact that there were more data sets taken using the Fieldfox, as the Fieldfox only was originally used since it is handheld and is the only VNA that can be used when measuring in the dish at the DRAO. The ENA was later added due to the daily changes that was seen in the Fieldfox data. It was hypothesized that the ENA may be more consistent across data sets as the ENA is the more precise device between the two. The daily changes are still present, but it is an improvement. Therefore, the Fieldfox will continue to be used for measurements as its daily variance results are similar to those found with the ENA and therefore neither appear to be specifically introducing any measurement error. Further investigation as to what may be affecting the width results of the resonance peaks is conducted in the following section. The tests are performed with both the Fieldfox and ENA in order to determine if one VNA's is better than the other at controlling this issue.

**(a)**

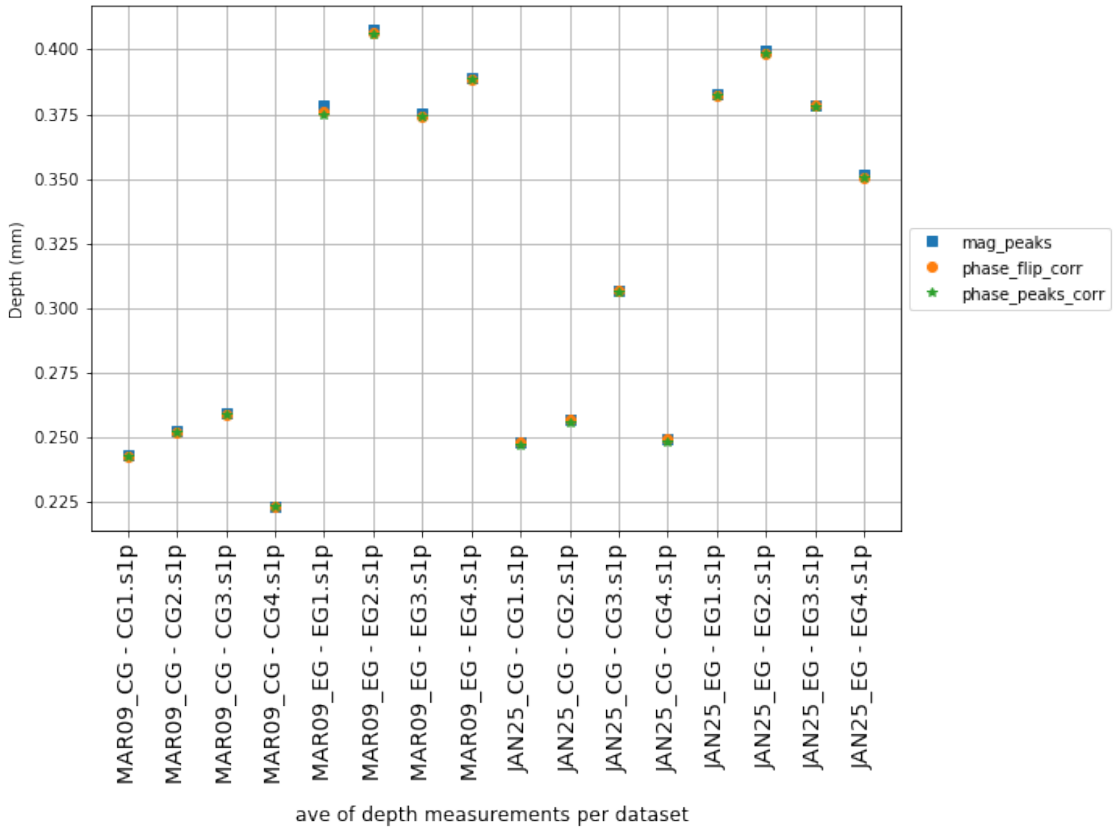


**(b)**

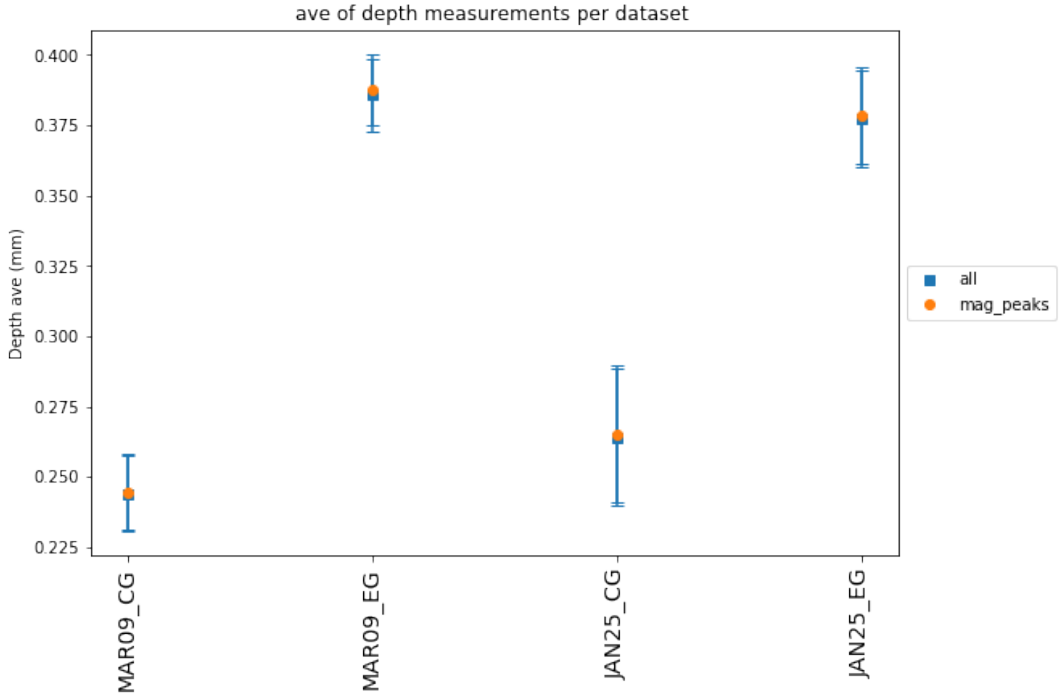


**Figure 5.10:** Summary of two data sets taken with the ENA. The results for the Pearl and C-Glass veils are displayed and the dishes have a depth standard deviation between 0.012 – 0.025 mm. The CG label refers to the C-Glass veil and the EG the Pearl. **(a)** Displays the calculated depth for each veil and **(b)** an example of one of the rms calculation plot's using the "mag_peaks" finder method only in this case. The plot displays the average of the depths per folder and then calculates the standard deviation (error bars) per method. As the methods have similar error bars only the one method along with the average of all the methods is displayed.

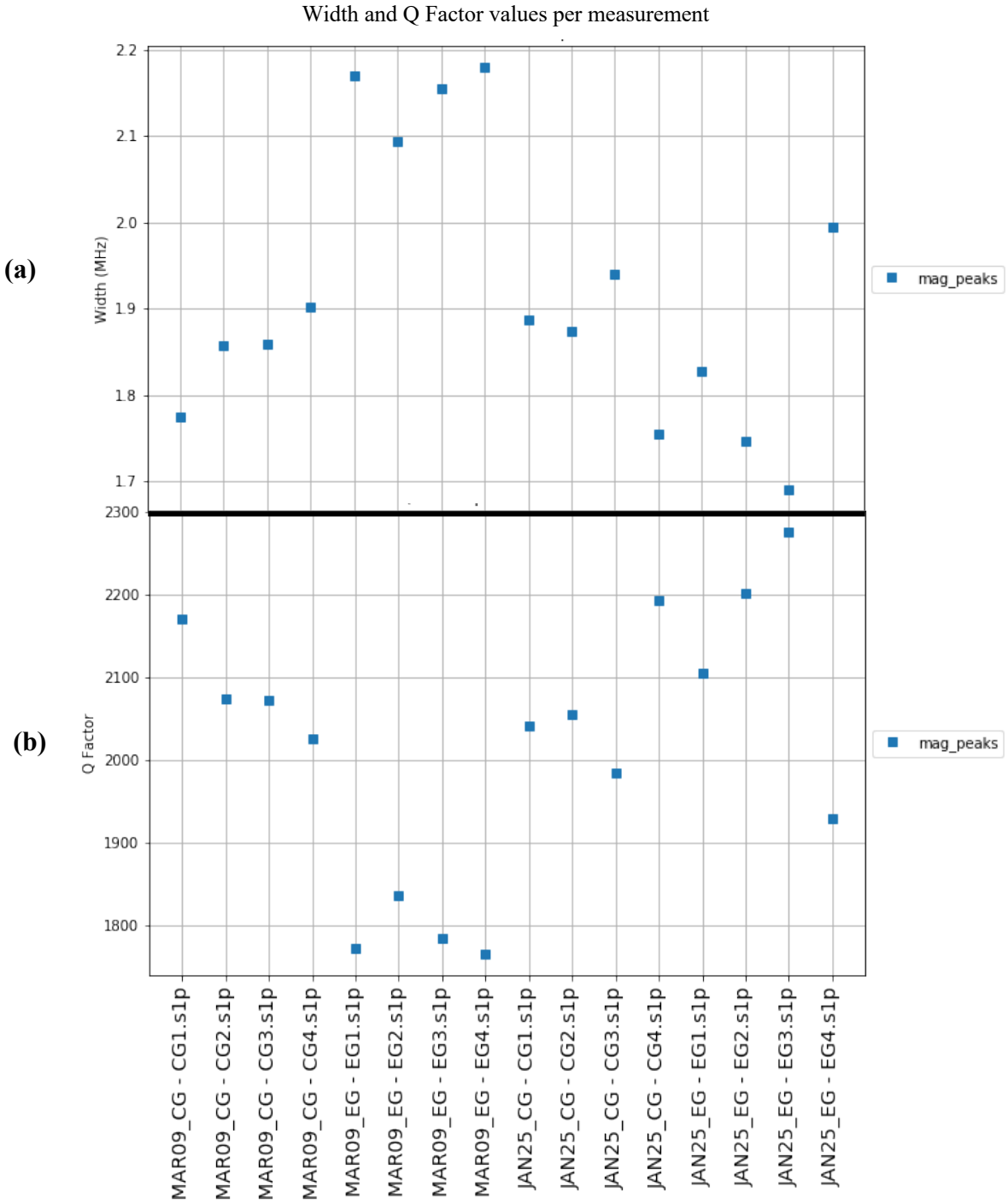


**Figure 5.11:** Summary of two data sets taken with the ENA. The results for the Pearl and C-Glass veils are displayed and the dishes have a depth standard deviation between 0.012 – 0.025 mm rms. The CG label refers to the C-Glass veil and the EG the Pearl. **(a)** Displays the measured FWHM of the $TE_{011}$ peaks and **(b)** the Q factor. The results overall are slightly higher than that of the Fieldfox but display the same trends of the widths and Q factors being in the same range for both veils. There was a difference between the C-Glass and Pearl Q factor values seen with the MAR_09 but it was not larger than the daily variance seen so far and has only been seen in this one data set so no conclusions were drawn based on this change.

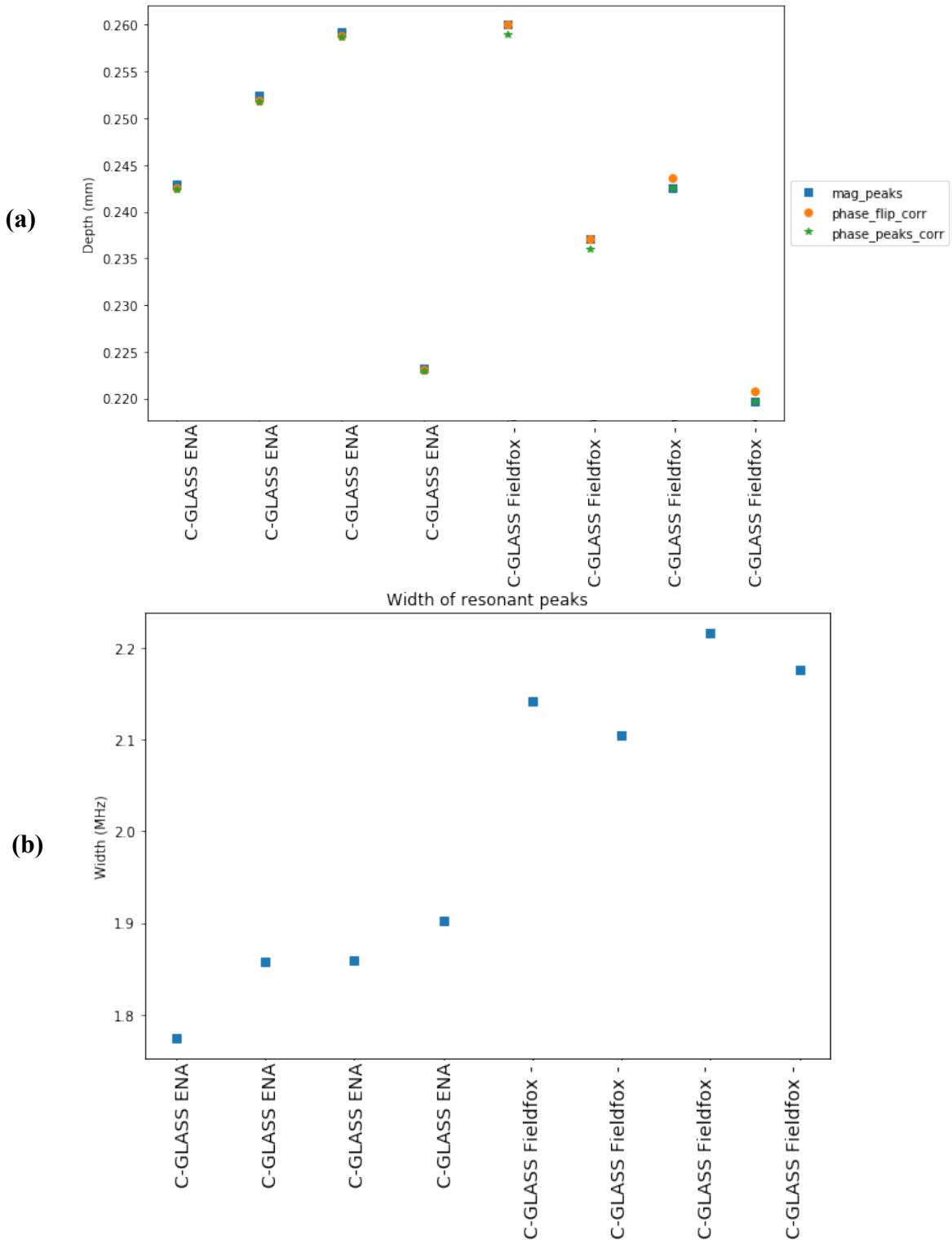


**Figure 5.12:** Comparison of C-Glass measurements using the ENA and Fieldfox on the same day to gain a better understanding of the difference in measurements between the VNAs without introducing any daily changes. The ENA has a larger depth and a sharper resonance dip leading to a smaller width and larger Q factor compared to the Fieldfox. The change is not large enough to cause concern with the reliability of one of the VNAs but does mean we should continue to use both in our calibration tests.

## 5.2 VNA Calibration Test

The VNA calibration test was designed to determine if the daily changes to the measurement results seen so far are created by the VNAs. For the previous measurements, the VNA calibration was redone every day. If the daily recalibration of the VNAs is causing the daily changes, then using a save calibration taken on one day and reloaded and used on another testing day should produce more consistent results. The test will be first completed with the Fieldfox and later the ENA to determine if one of the VNAs is possibly better than the other when using the saved calibration. When discussing the calibration sets, a new calibration which will be referred to sometimes as recalibrating, is when we use the calibration kit to calibrate the VNA. When we say that we are using a reloaded calibration that means a saved calibration is being uploaded to the VNA and used instead of using the calibration kit to calibrate the VNA that day. The VNA calibration kit used for both VNAs is the Keysight 85033D/E as described in Chapter 4. For the Fieldfox, the saved calibration is reloaded to be used on different days by uploading the original calibration set to a USB key and later downloaded onto the Fieldfox. The ENA is capable of saving a calibration set in its list of calibrations. This means we can simply reload that calibration by selecting it when we open the ENA's calibration set list. Power cycling was the other aspect that was used to test the VNAs. After power cycling a new calibration is done but in the last round of measurements another calibration is done without power cycling. This measurement was conducted to determine if the power cycling has an effect on the measurements. Since the same calibration kit is being used both times it is expected that the results should be even closer than the measurements separated by power cycling. The purpose of all these different calibration methods was to gain a better understanding of what affects the VNAs and what leads to larger differences than expected in the measurements.

### 5.2.1 Fieldfox Data

Beginning with the Fieldfox, the calibration test was run on the Aluminum sheet as outlined in Chapter 4. Overall, there were changes between the individual tests on the same day, but the changes were no greater than 0.02 mm. The changes seen from the testing the next day were much larger. The average depth for the first day was -0.073 mm with a standard deviation of 0.004 mm and the second day was -0.093 mm with a standard deviation of 0.004 mm. If the calibration was causing the issue, then the data taken with the reloaded calibration saved from the first day of testing should have produced approximately the same average results (can be seen in data titled RECAL23NOV in Figure 5.13). This is not the case, with the reloaded calibration data having on average a 0.02 mm difference when comparing to the data set using the same saved calibration (ORG set from November 22nd in Figure 5.13). Similarly, for the width measurements the original saved calibration and the reloaded calibration data are different, with the original calibration having an average width of $2.84 \pm 0.08$ MHz and the reloaded calibration having an average width of $3.11 \pm 0.06$ MHz. This corresponds to the Q factor ranging between 1275-1300 for the original and 1220-1260 for the reloaded calibration. The new calibration taken on the second day produced width results more in line with the first day suggesting that the calibration being saved and reused on the second day led to a bigger difference in the results (see ORG from the 22$^{nd}$ and NEWCAL from the 23$^{rd}$ in Figure 5.14).

The saved calibration was not only used on the second day of testing but also the first after power cycling the Fieldfox (see NOV22_RELOAD). We can see changes in the width measurement and Q factor even between these two measurements taken on the same day. Again, had the new calibration and been causing the changes seen between data sets, the data sets using

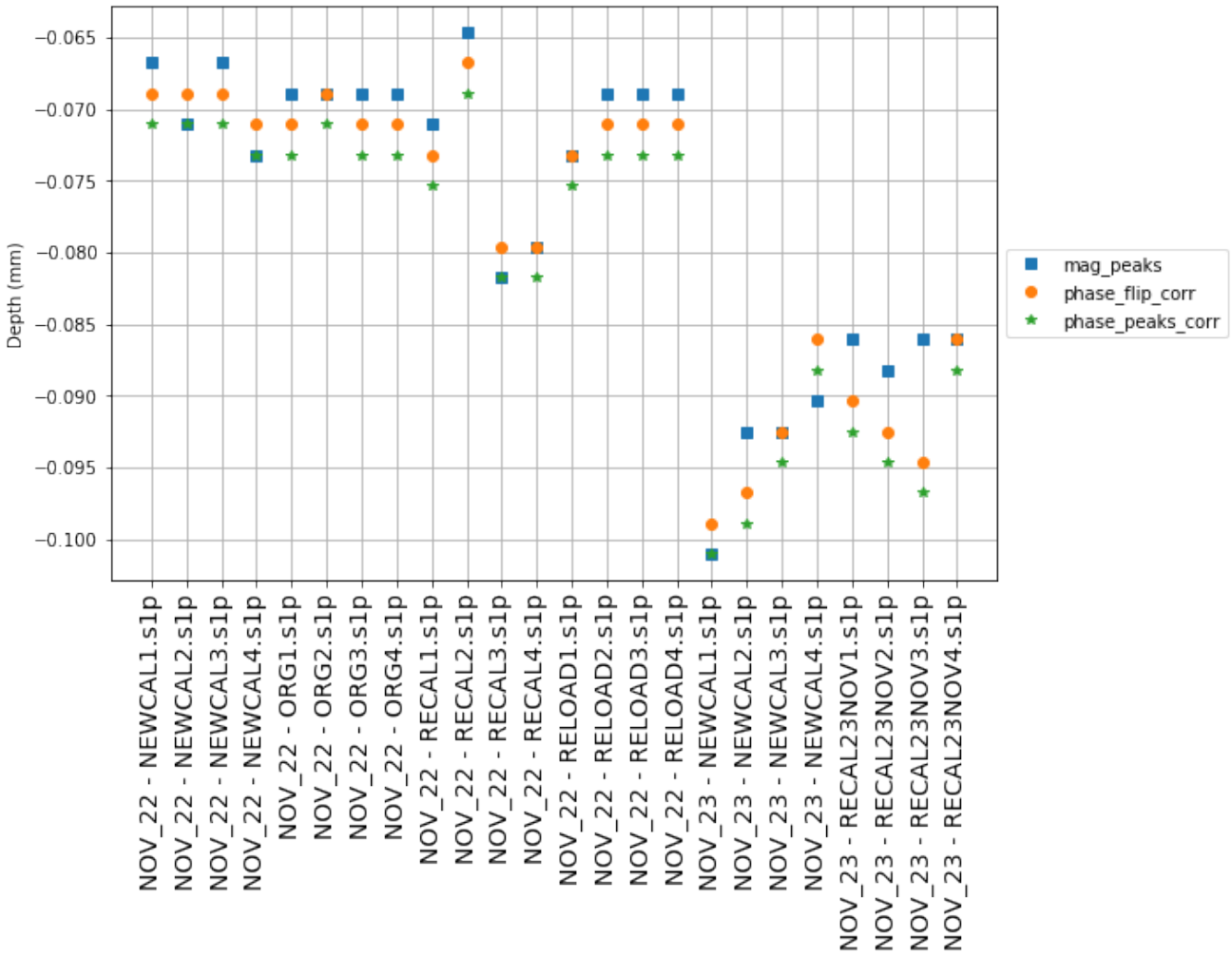


**Figure 5.13:** Calibration test result using the Fieldfox. The data compares two different test days, the 22nd and the 23rd of November 2022. On the 22nd the data sets are as follows: ORG is the original calibration which is saved for reloading. RELOAD is the reloaded calibration after power cycling the Fieldfox. RECAL is the new calibration done after power cycling and NEWCAL is the new calibration done without power cycling immediately after the RECAL. On the 23rd the RECAL corresponds to the reloaded calibration from the 22nd and NEWCAL is the new calibration done after power cycling the Fieldfox. The graph above is the depth calculation. The results for the depth using the saved calibration were not consistent between different days suggesting the recalibration done each day is not introducing the day-to-day changes. It appears beneficial to continue recalibrating each day as it produces more consistent results between testing days compared to the saved calibration.

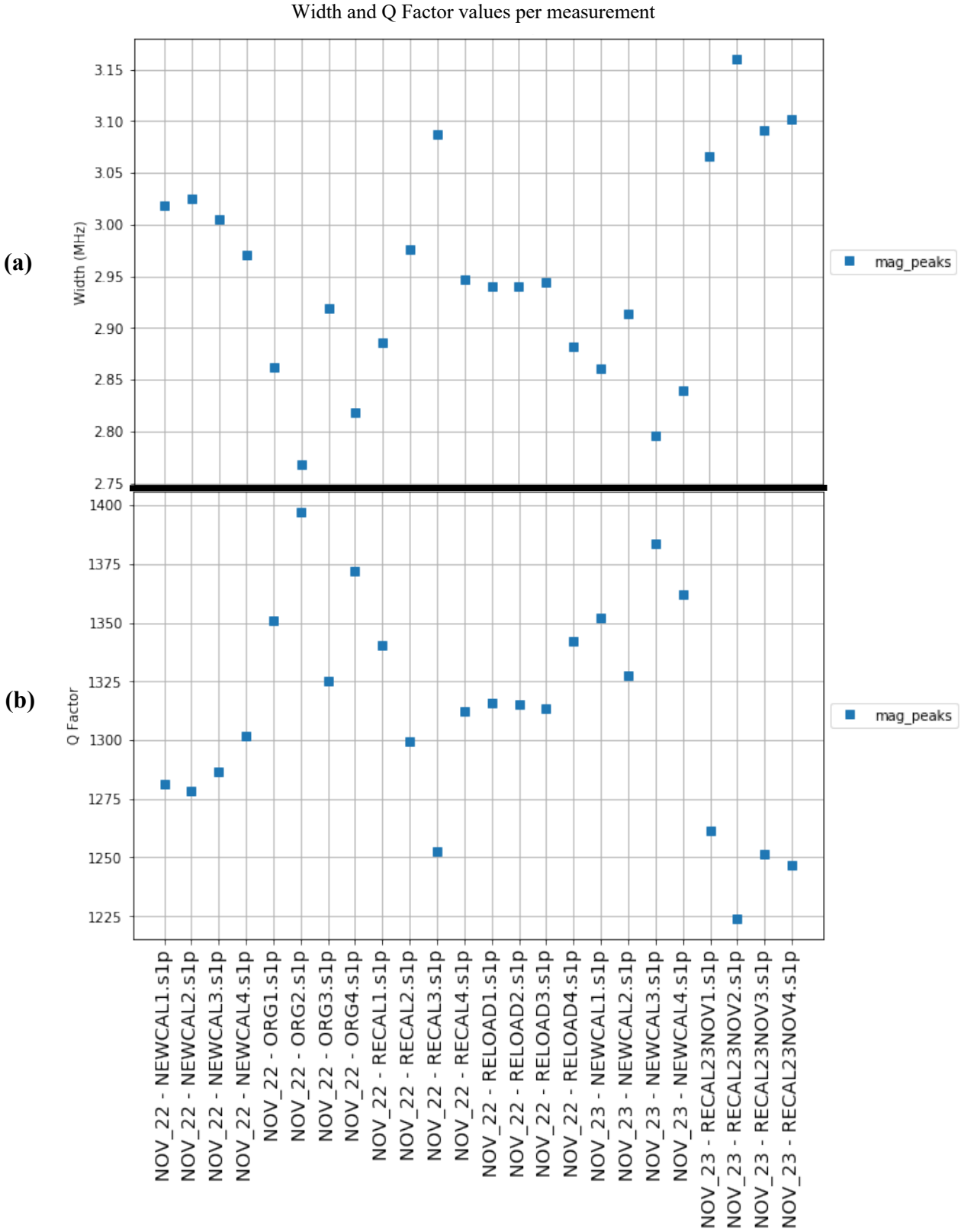


**Figure 5.14:** Continuation of calibration test result using the Fieldfox. The data compares two different test days, the 22nd and the 23rd of November 2022. **(a)** is the width measurement and **(b)** is the Q factor calculation. The Q factor data with the new calibration taken on the second day produced results closer to that of the first than the saved calibration did.

the same calibration on the same day should have been as close to uniform as possible compared to the other sets which have a new calibration used especially since no major day-to-day changes should have been introduced yet since the data sets are all taken in one go. Instead, there does not appear to be a much better comparison between the results using the same calibration than those using new ones on either day. Between these results and the results from the second day it does not appear that the new calibration is the cause of the day-to-day changes. Based on these results, it confirms that daily calibration is the correct method for testing as using a saved calibration did not reduce the daily variance in results. This is expected as the calibration kits made for the VNAs are created for the exact purpose of ensuring the most consistent results between different testing days. Now that we have confirmed daily calibration for the Fieldfox is the best option we will perform the same tests with the ENA to see if this is also the best option for the ENA.

### 5.2.2 ENA Data

The data for the depth calculation was quite consistent across the two separate testing days with no large shift in depth seen. The depth values were all within a range of -0.07 to (-0.1) mm. The only noticeable difference between the two days of testing was the fact that the different peak finder methods were in better agreement on the first day of testing compared to the second. On the other hand, the width measurements did still experience the day-to-day shift. The width results were between 2.70-2.85 MHz for the first day and 3.00-3.10 MHz for the second day. When comparing the results taken with the ENA to those taken with the Fieldfox we can see that the ENA data displayed a similar trend to that seen with the Fieldfox along with an overall improvement. For the ENA the second day results were more consistent between tests than what was seen for the Fieldfox. By this we mean that the ENA data sets taken on the second day were

shifted from the first whereas the Fieldfox new calibration data on the second day was in better agreement with the first days results. For the width values, the shift between days for the ENA is even more pronounced than the data taken with the Fieldfox since the data taken on the same day is more consistent. The Fieldfox had values for the width vary between 2.75 and 3.05 MHz within the same day so the jump to 3.10-3.15 MHz for the second days reloaded calibration results was not as drastic as the change in values that the ENA experienced between days. Based on the results presented for both VNAs we have determined that it is better to continue daily calibration as the saved calibration set being used on different days did not provide more consistent results. Although the ENA depth data was much more consistent between testing days compared to the Fieldfox, it failed to maintain that consistency for the width measurement and the subsequent Q factor calculation. Therefore, neither VNA appeared to perform better than the other at reducing the daily changes and it is recommended to continue using both for future resistivity measurements.

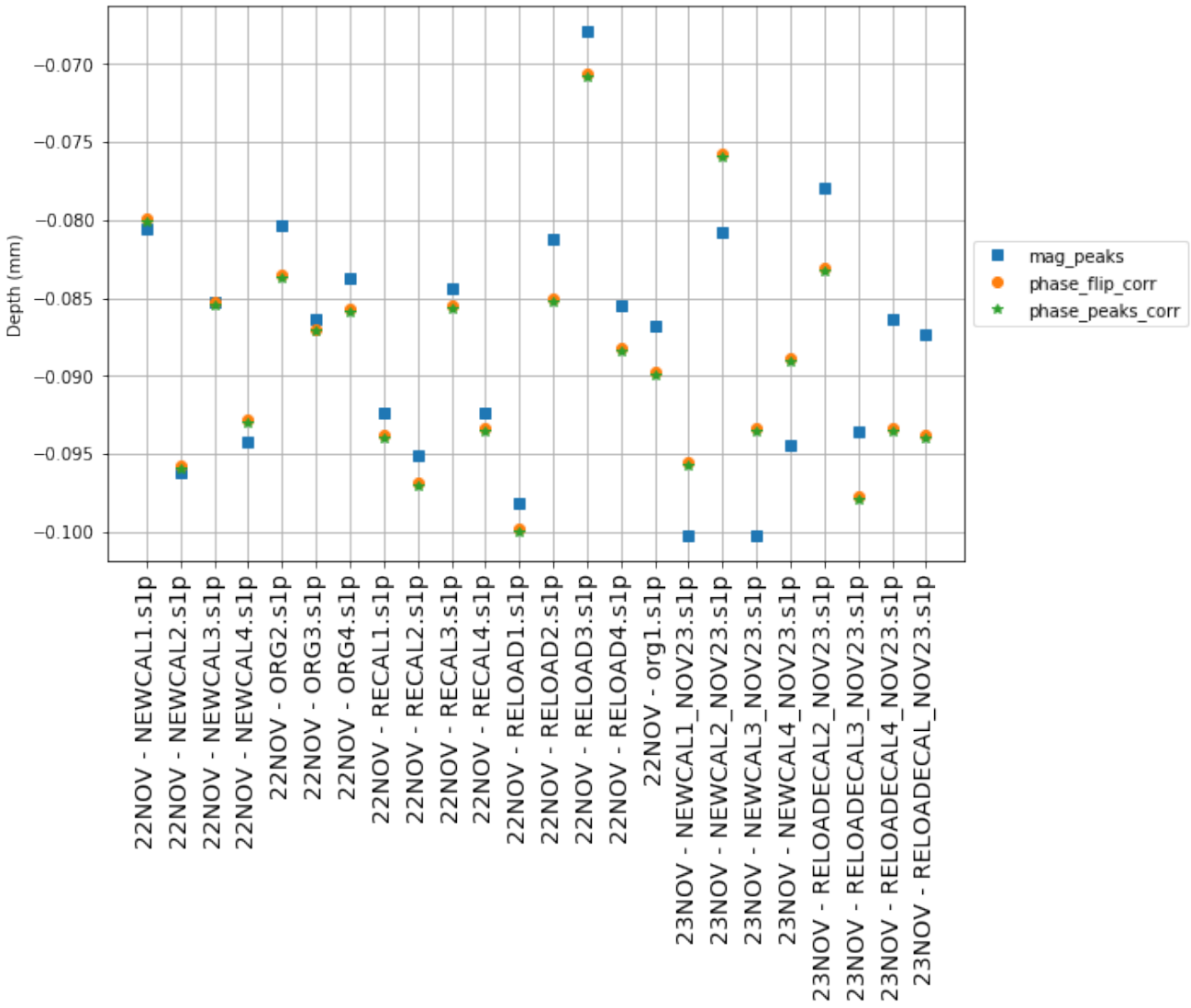


**Figure 5.15:** Calibration test result using the ENA. The data compares two different test days, the 22nd and the 23rd. On the 22nd the data sets are as follows: ORG is the original calibration which is saved for reloading. RELOAD is the reloaded calibration after power cycling the Fieldfox. RECAL is the new calibration done after power cycling and NEWCAL is the new calibration done without power cycling. On the 23rd the RECAL corresponds to the reloaded calibration from the 22nd and NEWCAL is the new calibration done after power cycling the Fieldfox. The graph above displays the depth calculation. The depth calculations were more consistent between testing days. There was no improved difference between the new calibration and the saved one for the results on the second day.

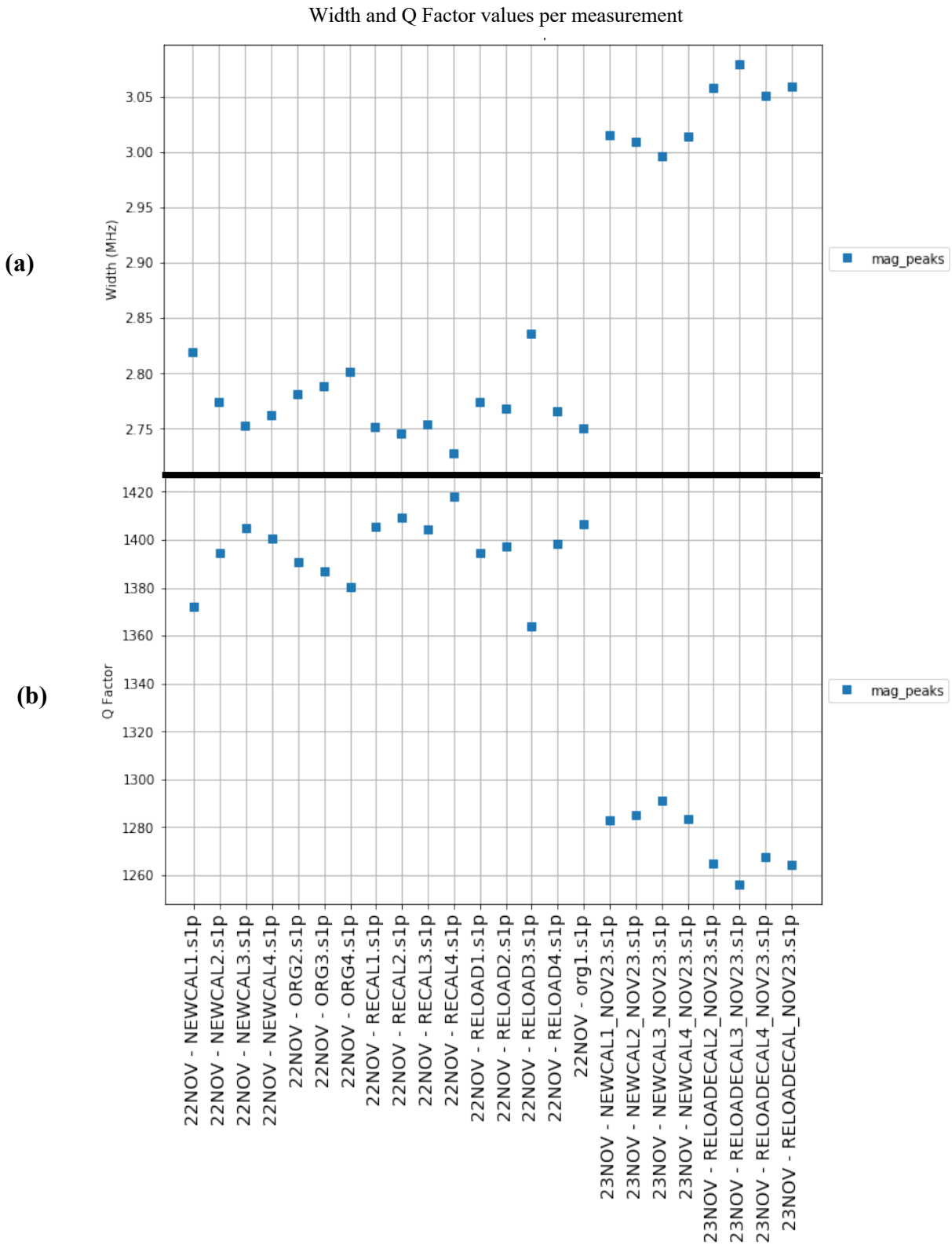


**Figure 5.16:** Continuation of the calibration test result using the ENA. **(a)** is the width measurement and **(b)** is the Q factor calculation. The width measurements were not consistent between testing days leading to a Q factor decrease of minimum 60 from the first to the second day. There was no improved difference between the new calibration and the saved one for the results on the second day. As with the Fieldfox data, we see results which are more consistent between testing days when we recalibrate the ENA rather than use the saved calibration.

## 5.3 Changes to Testing Environment

As we have now concluded that the daily calibration is the best option to ensure consistency between daily tests we can continue with the test designed to determine how changes to the testing environment affects the results. This entails changing the material beneath the veils as currently the resistivity and depth measurements have been taken with the veil on top of the non-conductive mat on the lab bench. To see if the mat has an effect on the depth and Q factor results, the veil will be measured while it is placed on top of the sheet of aluminum as well as on top of the lift which will simulate the effect of the veils being suspended in the air. Since the final dishes will have nothing directly beneath them except for air, the results for the lift are expected to be the most in line with what would be seen for the actual dish. The tests will be completed as outlined in Chapter 4 which detailed the exact procedure used for the three different measurement types, mat, aluminum and air when taking four different measurement locations on the veil. There was an additional set of tests conducted where the reflectometer's placement and location on the veil was maintained for four measurements. This was included to determine if the trends seen were possibly caused by the variation in the depth rather than the actual material beneath the veil. As mentioned in Chapter 4, due to the lift's height and size the environment testing could not be completed with the ENA as the cable was not long enough and in order to ensure comparability to the previous tests completed, the coaxial cable should not be changed. Therefore, the environment test was performed with the Fieldfox alone. The initial test was completed twice on different days to see how the day-to-day changes might affect the measurements and the test to verify the trends seen was taken once.

### 5.3.1 Environment Test Results

Although the exact results were slightly different between the two tests, the trends remained the same for both the veils and testing days. For the depth measurements, it was largest for the simulated air and very closely followed by the measurement on the mat with results of $0.37 \pm 0.03$ mm and $0.34 \pm 0.05$ mm respectively for the C-Glass and $0.54 \pm 0.03$ mm and $0.49 \pm 0.05$ mm respectively for the Pearl. The aluminum beneath changed the results quite a bit and resulted in the depths measured at $0.29 \pm 0.04$ mm for C-Glass and $0.43 \pm 0.05$ mm for Pearl. The values presented were calculated using the depth average results for the two testing days per measurement type. These depth values would be averaged, and the error bars determined by how large of a difference the daily results were from this average. Since the measurements taken here will include a rms value caused by the standard deviation of the mesh depth itself the second test conducted in the next section where the reflectometer is kept at the same location each measurement will determine if these error bars are too large. The stated values include the depth calibration from the aluminum plate. For the widths, the aluminum base result had the largest value which is consistent with the fact that the aluminum sheet alone had a larger width and therefore lower Q factor compared to the veil measurements. The Q factor for the simulated air was close to the aluminum results. As the mesh is made out of aluminum, we expect the resistive nature of the mesh to be similar to that of pure aluminum but not exactly the same since the mesh is an expanded metal sheet of aluminum. Using expanded metal compared to the traditional mesh increases the resistivity as there are no welded joints and therefore there is no vibration at the joint between two individual wires. The resistivity is dependent on the direction of flow for the expanded metal grid as will be discussed in section 5.4. This is not an issue an aluminum sheet would encounter therefore we expect there to be a direction of flow where the resistivity for the

expanded metal will be larger than that of the aluminum sheet and vice versa. As for the Q factor results for the measurement with the mat beneath, the values were higher than both the air and aluminum results. Due to the mm sized diamond cut outs in the mesh there will be some small amount of field leakage through the veil. The mat beneath the veil should not interact electromagnetically but does still have an effect on the resonance behaviour in the cavity due to these field leaks. For both the aluminum and mat measurements, this is not the behaviour we would expect for the dish once it is constructed. It is difficult to say if the lift did correctly simulate the environment that the dish will experience when it is constructed without testing directly inside a built dish. We believe that the lift was constructed tall enough to avoid introducing any interaction between the resonance cavity and the surface below (in this case the wooden lab table). Therefore, we believe that the simulated air results should be a good approximation of the expected behaviour. The Q factor values do still have the daily variance which was an average 200 between our two testing days. The shift was not uniform across the different environments meaning the daily change does not uniformly shift the width values and that the material beneath the veil does play a role in how much the daily changes affect the resonance peak widths. The largest change in Q factor was for the mat beneath with a change of ~350 and the smallest shift was the simulated air with a change of ~100. This suggests that the mat and the aluminum can amplify or play a role in the changes seen day-to-day as well. Based on these trends it seems that the most accurate results between days can be obtained by using the lift when taking the depth and resistivity measurements. Before this can be concluded for sure, we will ensure the trends seen thus far are not skewed by the depth changes.

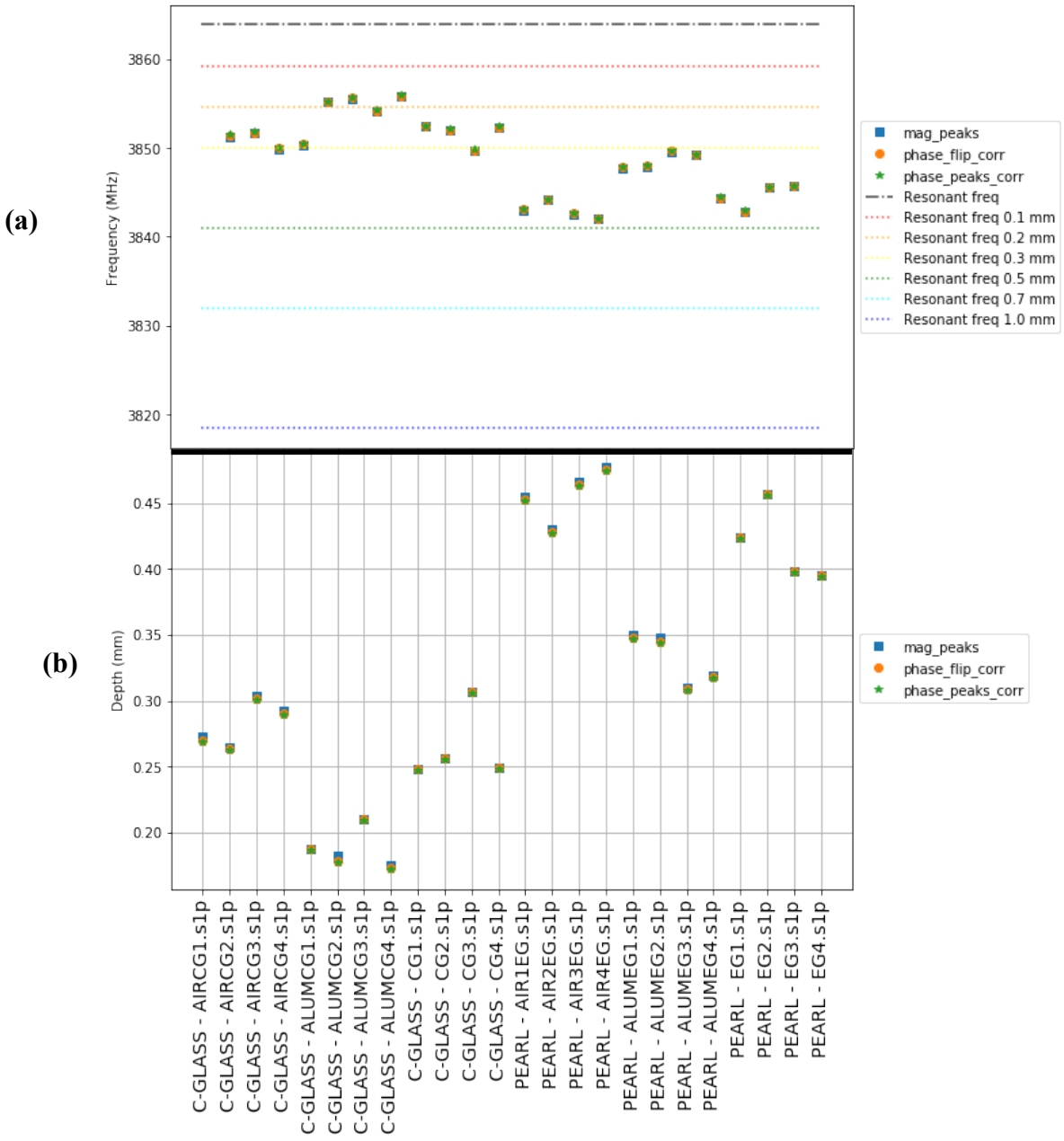


**Figure 5.17:** Transparency measurement results with both the Pearl and C-Glass veils. The measurements are separated into three types: aluminum, mat or air. The mat tests are the set with no extra name added (ex: CGLASSFF1). Data taken while changing the location of the reflectometer on the veil but maintaining the direction of the antenna. **(a)** resonance frequencies and **(b)** the calculated depth. The depth measurements were most similar for the air and mat measurements suggesting the aluminum adversely affects the resonance cavity and leads to the depth of the embedded mesh being underestimated.

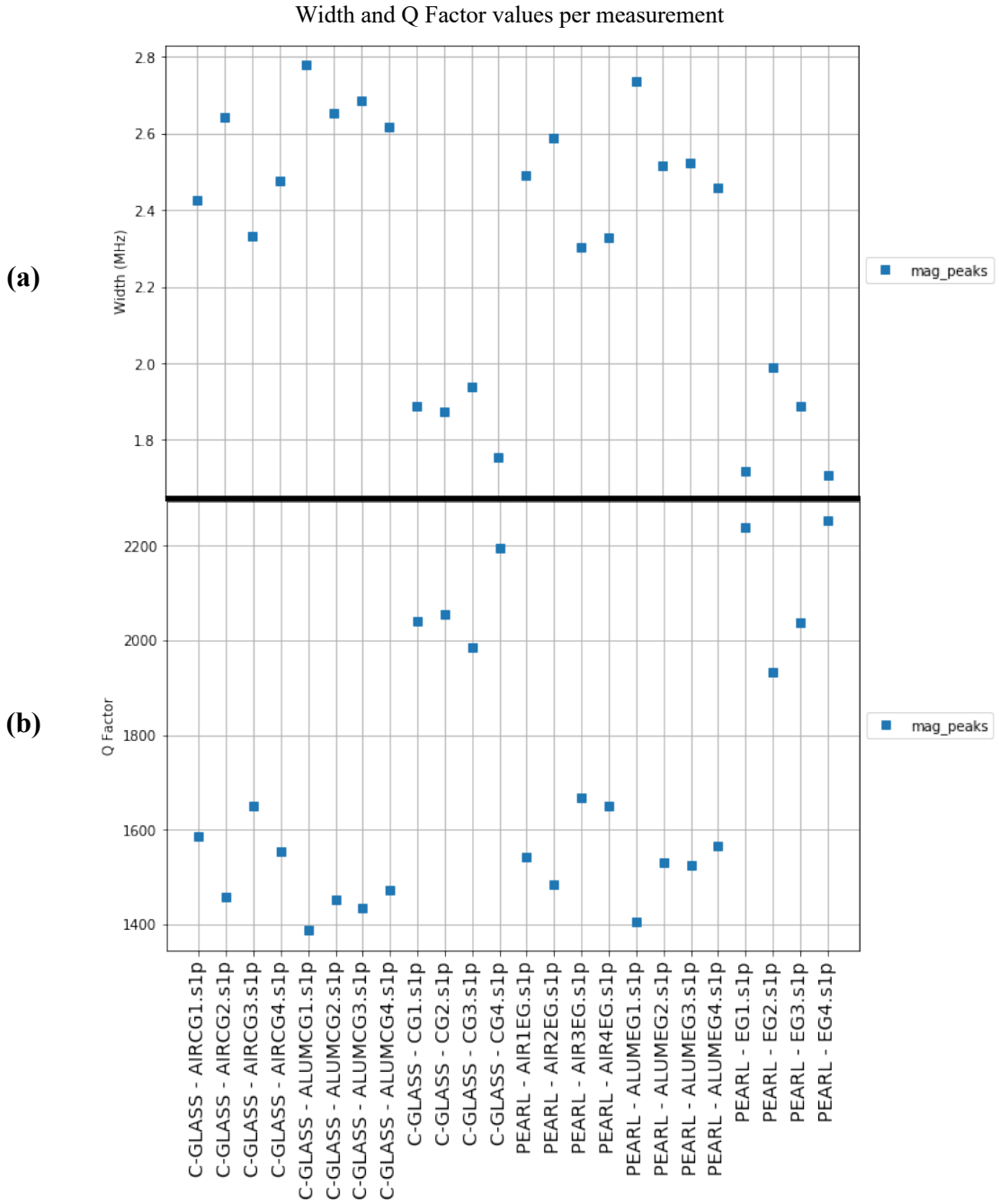


**Figure 5.18:** Continuation of the transparency measurement results with both the Pearl and C-Glass veils. The measurements are separated into three types: aluminum, mat or air. The mat tests are the set with no extra name added (ex: CGLASSFF1). Data taken while changing the location of the reflectometer on the veil but maintaining the direction of the antenna. **(a)** the width and **(b)** the Q factor. The Q factor results were most similar for the air and aluminum. The mesh embedded in the dish is made of an expanded aluminum sheet, so it we expect the resistive behaviour to be similar but not exactly the same since it is finer due to the holes. The mat appears to affect the resonance behaviour and reduces the resistivity the resonance cavity feels.

### 5.3.2 Test to Confirm Trends

The environment test was conducted once more but this time the reflectometer was placed at the same location each measurement rather than moving it around like the previous data sets. This test was added to confirm the relationship being seen thus far and ensure there were no trends that were caused by the changes in depth in the embedded mesh falsely appearing as trends caused by the material beneath the veil. The trends were the same as the previous tests with the range in values being slightly more consistent as the change in depth was no longer an affecting factor. The width and Q factor results for the air and aluminum were even closer than in the first tests suggesting that the simulated air has a very similar resistive behaviour as the aluminum sheet in combination with the mesh (Figure 5.19). The simulated air still had the largest depth with a value of $0.360 \pm 0.002$ mm for the C-Glass and $0.500 \pm 0.005$ mm for the Pearl. As expected, the error bars are much smaller now that the variance of the mesh is not included in the measurement results. The width and Q factor values for the aluminum and air measurements for both veils were approximately the same with width values of 2.65-2.70 MHz for the C-Glass and 2.55-2.60 MHz for the Pearl. The results with the mat underneath were not as similar with C-Glass having a width of 2.0 MHz and the Pearl 1.8 MHz. This was interesting as the previous test results were very similar for each material used as can be seen in the width graph in Figure 5.17 and 5.18. Since the mat is the material which was used during the resistivity tests, we can compare this change to what was seen in the previous results. The veils had a similar range in width for almost all data taken, with only two sets taken where the range in width values were slightly different. The previous time this occurred it was the C-Glass that had the lower width measurement, so it appears as though the slight shift in width seen in this measurement was most likely due to a measurement error such as the coaxial cable not being secured tightly enough.

The cable can loosen when taking measurements and if it is not retightened between measurements, it causes changes in the resonance peak amplitude.

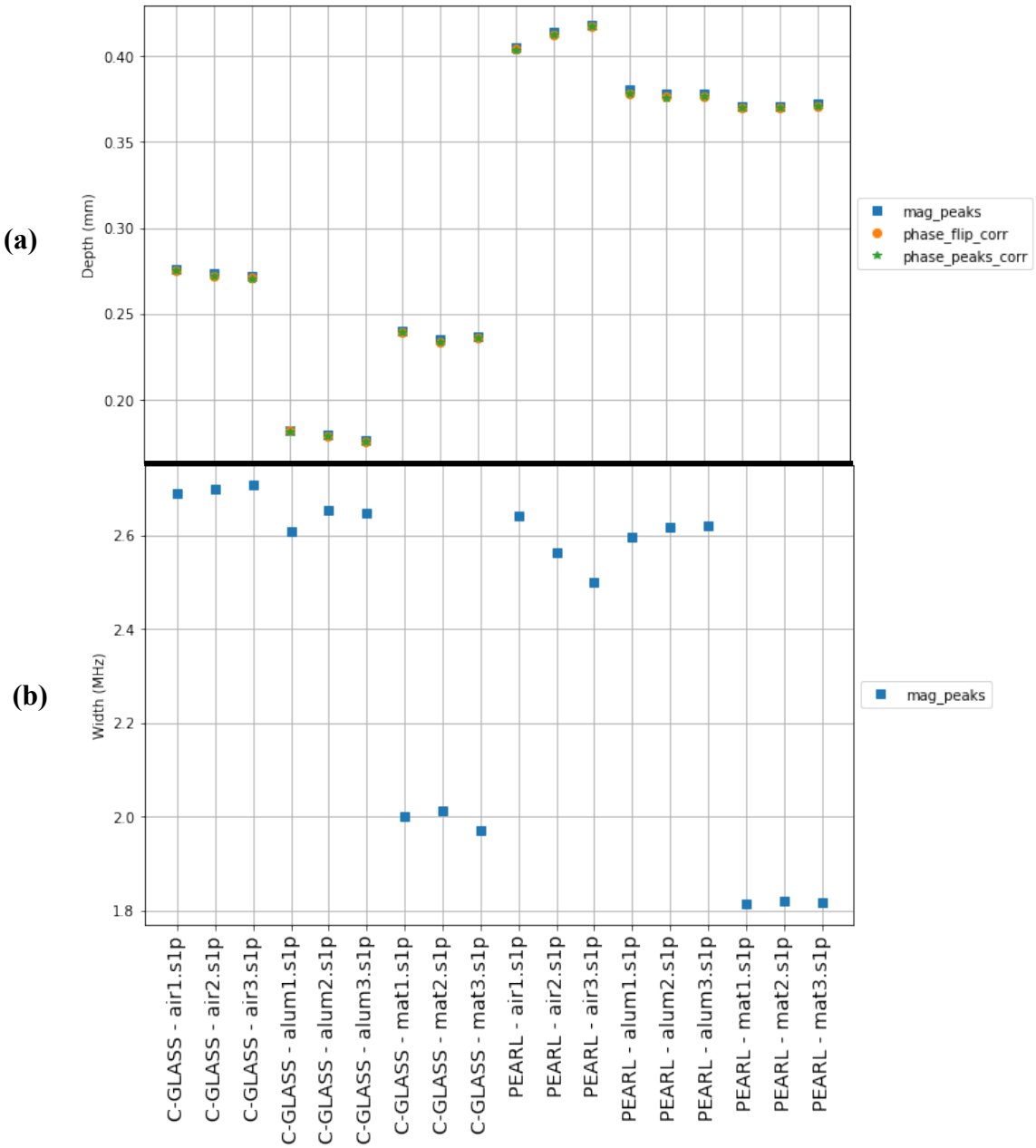


**Figure 5.19:** Transparency test conducted with both veils but maintaining the reflectometer's position between measurements. The trends seen during the original tests are also seen here confirming the trends were not skewed by the changes in depth. The resistive behaviour seen before where the air most closely resembles the bare aluminum sheet occurs here again confirming that the resonance behaviour seen in Figure 4.11 was not caused by day-to-day changes and is in fact behaving like we would expect for an aluminum embedded mesh.

## 5.4 Rotation of Reflectometer Position

While conducting the resistivity tests the placement of the reflectometer was kept the same on the veil as well as the direction that the antenna was pointed towards as much as possible. During these tests we noticed that rotating the reflectometer caused some small fluctuations to the resonance peak. A new test was included where the reflectometer position was rotated while in the same location on both the veils and then the aluminum. The angles varied from 0° to 90° with points at 20°, 45° and 60° as described in Figure 5.20. Test were conducted with both the Fieldfox, and the ENA and the following trends and data were seen with both VNA's. The aluminum plate results remained quite consistent between the degree changes which was expected as the surface is uniform no matter the placement of the reflectometer. The veils on the other hand contain an expanded metal sheet which has an elongated diamond cut out shape. The diamond's longest axis is in the direction of our 0° measurement axis (Figure 5.21). The change in angle caused slight variations in the data points for the depth but a much more pronounced change in the Q factor. The curves were steepest at 0° and widest at 45° (Figure 5.22). A parabolic shape can be seen in all the data with the 45° point being the maximum or minimum depending on the data calculated. For the depth, the values had a standard deviation between 0.008-0.009 mm which is not significant enough to affect the confidence in the depth measurements made thus far nor the accuracy required for the tolerance specification. For the Q factor, the rotation resulted in a significant change with the difference between the 0° and 45° being 450 or 0.60 MHz for the width value. The highest Q factor was seen for the 0° with a value of approximately 2050 for the C-Glass and 2100 for the Pearl when using the ENA and 1900 and 1950 respectively for the Fieldfox. As mentioned before, the 0° is the same direction of the long way of the diamond (LWD) (Figure 5.21). This is the direction that has the lowest

resistance for an expanded metal sheet [34]. The direction of flow for our veil is along the 90° axis which is the same direction as the short way of the diamond (SWD). This direction should also have a lower resistivity but not as low as the LWD direction since the distance between the metal wires is smaller. This is confirmed with our results since the Q factor for the 90° position was approximately 1750 for the C-Glass and 1800 for the Pearl with the ENA and 1615 and 1650 respectively with the Fieldfox. For an expanded metal sheet, the diagonal is the direction of flow which has the highest resistivity. This corresponds to the point where the antenna is directly in line with the diagonal wire. When the reflectometer is placed at the 45° angle it is in line with the direction of the wire meaning it should experience the lowest Q factor here. This is again confirmed by the results with the Q factor being approximately 1600 for the C-Glass and 1650 for the Pearl with the ENA and approximately 1450 for both veils with the Fieldfox. Since the direction of flow for our veils is the 90° axis it is best to ensure the reflectometer is placed along that direction so that we can properly estimate the possible resistive loss that the incoming signal will experience.

Since the expanded metal mesh does not have a consistent resistive behaviour as we saw with the solid aluminum sheet, the angle with which we perform our tests must be maintained between testing days. Should this not be maintained, the results may appear to have variations caused by the daily changes but in actuality are simply due to the direction of the reflectometer. This affect that the rotation has on the Q factor is significant and cannot be ignored when conducting tests. The interpretation of the resistive behaviour of the dish samples can be skewed if the angle at which the reflectometer is placed is not maintained. This is a parameter which can help reduce

the changes seen between tests so that when all other testing protocols are maintained the only changes seen for the data should be due to the daily variance.

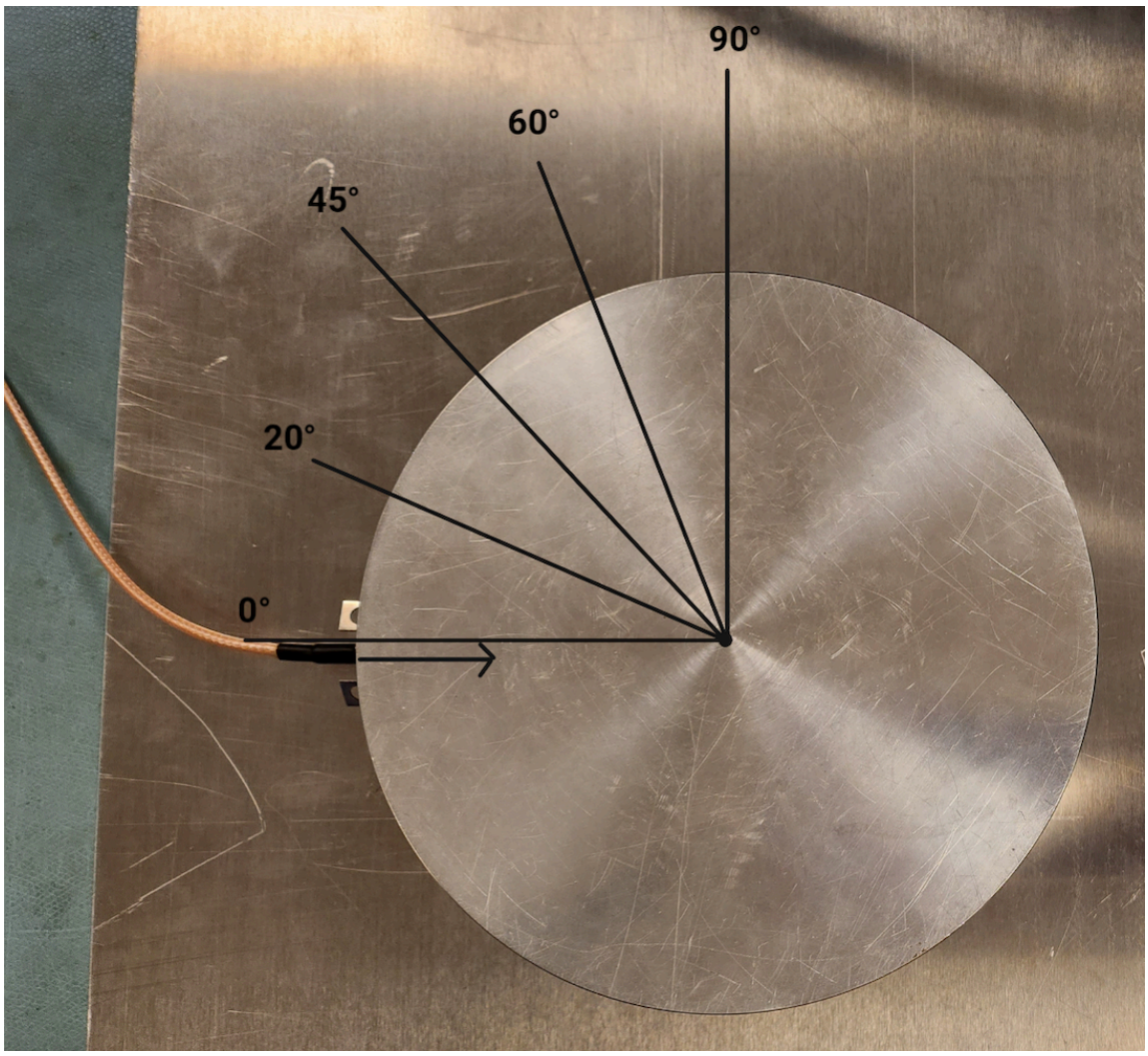


**Figure 5.20:** Diagram of the angles used for the reflectometer placement. Angle is based on the direction of the antenna with the arrow showing the antenna pointing in at the 0° point. Reflectometer was rotated to each angle between 0° and 90° per data point.

**(a)**

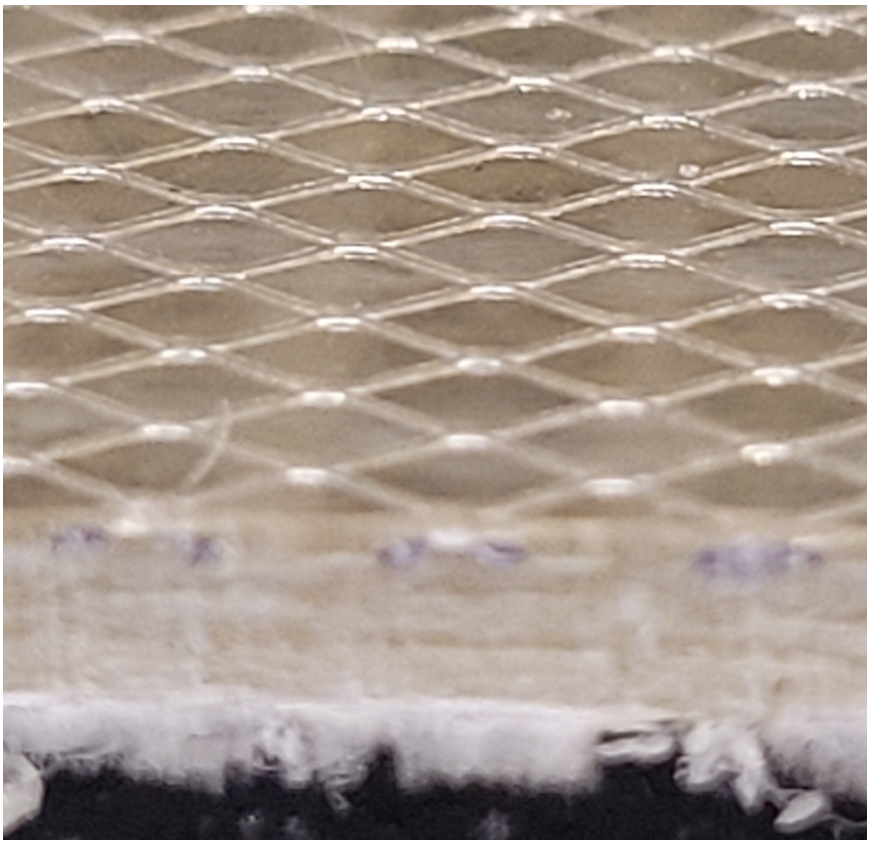

**(b)**

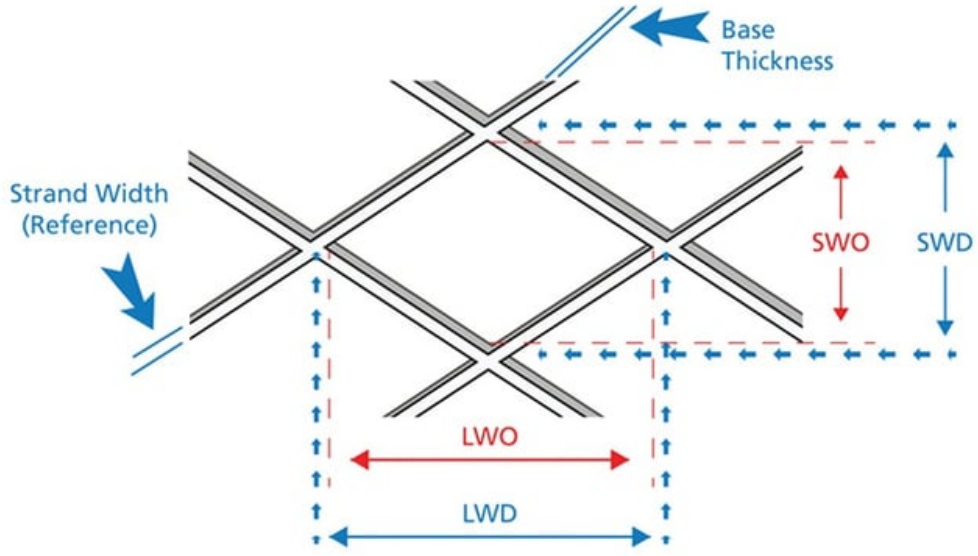


**Figure 5.21:** Close up image of the mesh embedded inside the composite material of the dish sample in **(a)**. The spread mesh pattern can be observed via the elongated diamond shape of the cut outs which is described in the diagram from Dexmet in **(b)**. Photo credit: **(a)** L. Gonzalez Escudero and **(b)** [32]

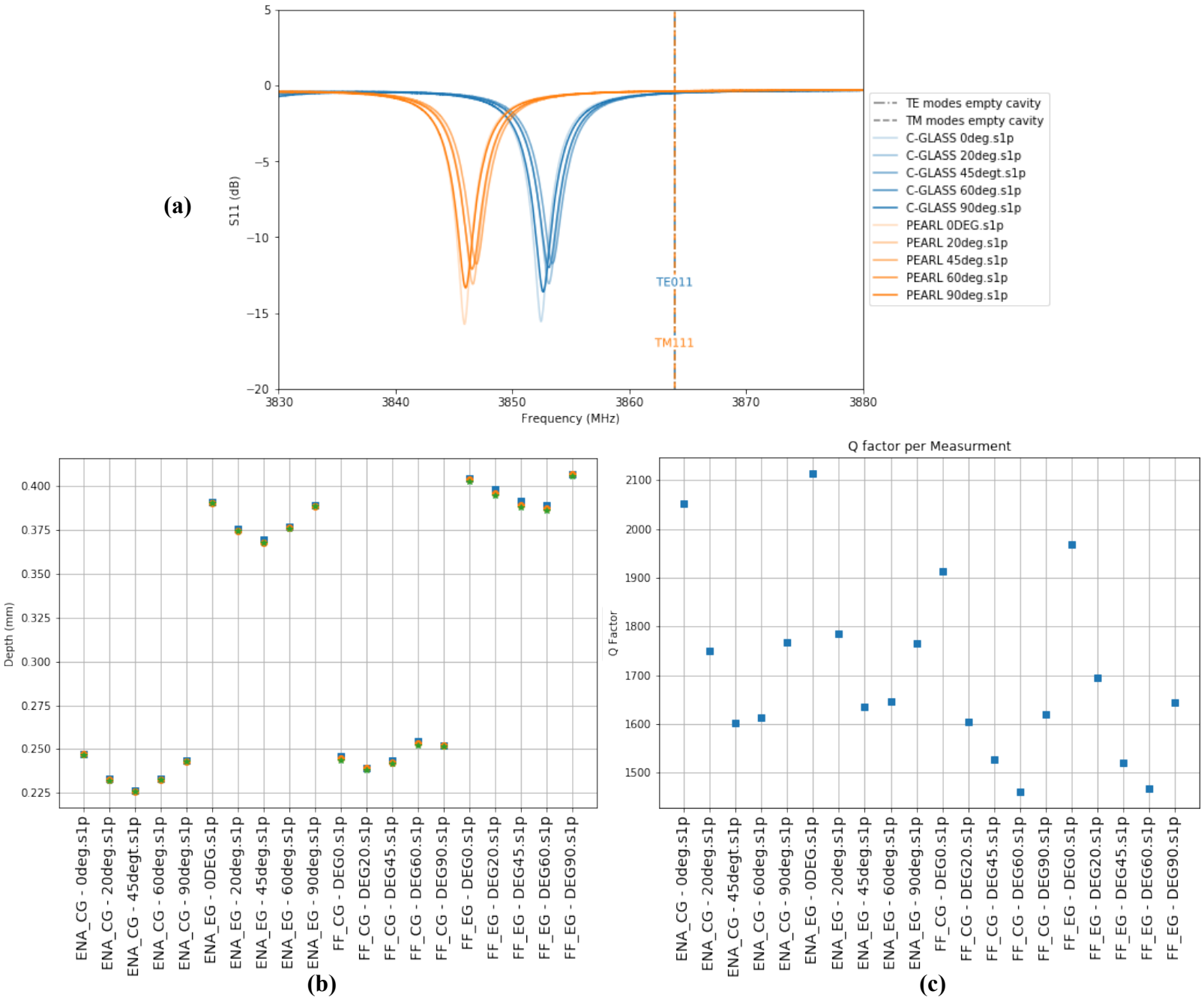


**Figure 5.22:** Data taken with the ENA and Fieldfox. Rotation of reflectometer from 0° to 90° on the C-Glass and Pearl veils. **(a)** is the $S_{11}$ curves using the ENA for each veil, showing the change in amplitude of the peaks per angle. The next graphs display both the Fieldfox (FF) and the ENA data where CG refers to the C-Glass and EG the Pearl. **(b)** is the depth calculation for and **(c)** the Q factor calculation. Both graphs have a U shape to the data points with 45° being the min/max. For the Fieldfox, the curves were not as smoothly parabolic with the 60° having the lowest Q factor instead but the trend of the 0° and 90° being the highest remains the same. Data for the depth varied across a range of 0.025 mm and the width 0.600 MHz (~450 Q factor) for both. The width and Q factor range is similar to the values seen from daily changes.

# Chapter 6:

# Summary

Reflectometry is an important tool to use while prototyping the dishes for an interferometer array. It is capable of measuring the depth of an embedded electromagnetically reflective surface by creating a resonance cavity with the surface as the enclosing wall and tracking the shift in frequency for a specific resonance mode, which for our case was the $TE_{011}$mode. It was capable of detecting variations in the depth of the embedded surface below 0.1 mm with the maximum standard deviation seen for the two dish samples being 0.035 mm rms and average results being between 0.010 – 0.025 mm rms for both dish samples. It had an approximate error of less than 0.05 mm when tested with both VNAs, namely the Fieldfox and the ENA. These values fall well below the sensitivity requirement set by CHORD and HIRAX which required the dishes have surfaces consistent within 0.1 mm meaning that the reflectometer was able to operate within the constraints needed for dish prototyping.

The resistive properties of the embedded material was another parameter the reflectometer measured. It did so by monitoring the change to the resonance behaviour in the cavity which presented itself as changes to the FWHM of the $TE_{011}$resonance peak. From the width change the Q factor was measured which provides information about the resistive properties of the embedded metal. From the Q factor we can determine how conductive the metal material is, with a lower Q factor indicating that the metal is more resistive and can lose energy with fewer oscillations than a higher Q material. When discussing the physical representation of the Q factor we can discuss it in terms of oscillations. At high Q values, such as those seen with the

reflectometer, the Q value roughly represents an estimate of the number of oscillations it takes for a freely oscillating system to lose up to $e^{-2\pi}$ of its original energy or until only 0.2% of the energy of the system remains. Therefore, for values of Q between 1400-1800 measured with a 3GHz electromagnetic wave like the tests taken with the reflectometer, the wave should bounce off the reflective embedded surface at the very least 1400 times before it decays away. This means the decay is two times the Q factor since the decay includes half of the bottom and half of the top of the reflectometer and as we are only concerned with the loss from the bottom of the reflectometer a factor of two must be included. The decay would be 2800 and the reflective loss is $\frac{2\pi}{2800} = 0.002$ meaning that 99.9% is reflected. This rough order of magnitude calculation goes to show that the reflections are good enough that even the worst case of order unity variations along the surface will not matter in terms of the HIRAX/CHORD specifications for the resistivity. As mentioned in Chapter 3, the reflectometer uses a higher frequency than what will be seen by the constructed dishes and reflective loss is almost always worse at higher frequencies, so this value is expected to improve when the dish is being used by HIRAX/CHORD. Therefore, as long as the Q factor measured for the veils is in the higher Q region, the resistivity of the embedded mesh will be consistent enough to satisfy the surface variations conditions.

| Type of systemic Bias | Effect on Measurement |
|---|---|
| **Loose SMA connector (i.e. loose coax cable connection)** | Dampens the signal from VNA by at very least 5dBs, if too loose can lead to signal so damped "mag_peaks" cannot find a resonance frequency (Fig. 5.3). |
| **Antenna loop not parallel to surface** | Dampens signal seen in $S_{11}$ by 5dBs or more depending on position |
| **Changing direction of antenna with respect to direction of flow between measurements** | Can lead to change in Q factor measurements of up to ~ 450 or 0.60MHz in terms of width. |
| **Not maintaining same material beneath veils when measuring** | The material beneath the veil can change the resistive behaviour seen by reflectometer by a value of up to ~ 400 in terms of Q factor. |

**Table 6.1:** Summary of different systemic biases that can be introduced by the user and their estimated effect on the results taken by the reflectometer.

## 6.1 Best Practices

The reflectometer results experienced changes seen mainly in the width of the resonance peaks from day-to-day. These changes were on the scale of approximately 0.3 MHz for the ENA and approximately 1 MHz with the Fieldfox with a maximum difference of 1.7MHz seen between values. This translates to a change in Q factor of 300 for the ENA and 500-900 for the Fieldfox. These changes were tested in order to determine what may be causing them and how to reduce them since it is difficult to infer anything about the resistive nature of the material when the Q factor had such a large range of different values. Via the calibration test we confirmed that the

best practice is to recalibrate both VNAs each testing day. It was determined that the direction of the antenna with respect to the direction of flow for the veil did have a large effect on the Q factor with the changes being close in value to what was seen from the daily changes (0.60 MHz for the resonance peak FWHM and a Q factor change of 450). The material beneath the veil also lead to large changes in both the depth calculation and the resistive behaviour. It was found that the mat beneath the veils, which was used in most tests, produced a Q factor which was much higher than that of the air and the aluminum, with the aluminum and air results being quite close ($\geq$100 difference when kept at same location on the veil). It appears that the mat has an effect on the resonance behaviour of the cavity. We also expected the dish results to be similar to the aluminum sheet since the Dexmet is an expanded aluminum sheet. This trend was observed for the air results (with the Q factors both being around 1300-1400). The fact that the Q factors are very close also means that the field leakage from the veil is not large enough to cause concern for the HIRAX/CHORD frequencies of interest. Based on all these test results, a list of best practices is provided. This will help reduce measurement errors which may have been introduced by the user while taking measurements. These methods should be employed when testing the dishes that come from fabrication for CHORD/HIRAX to ensure consistent testing for all the dishes made:

- Always ensure the reflectometer is free of dust inside the cavity
- Ensure the coax cable on the outside of the reflectometer cavity is tightly secured as a loose connector leads to variations in the width of the resonance peak. Check the connection of the coax cable to the VNA between measurements as it frequently loosens.
- Ensure the antenna is tightly secured to the SMA connector and that the ring is parallel to the flat wall of the reflectometry.

- Make sure to pick the reflectometer up between measurements. Never slide it to the next position as that may scratch the edge of the reflectometer or loosen the coax cable of antenna.
- Always ensure to place the reflectometer at the same angle with respect to the direction of flow for the dish being prototyped. This must be done whether the test is being done on four separate spots of the same spot four times.
- When measuring the variance in depth and the resistive behaviour it is important to take data sets on multiple days in order to check the range of the daily changes. Variances in the depth generally did not go above 0.05 mm and the width varied no more than 1.7 MHz with different day measurements. Should values experience a change much larger than that, further investigation into the measurements taken that day will be necessary as error could have been introduced by the user.
- Always take note of what is beneath the veils when performing a measurement. Different materials have different effects on the depth and resistive nature of the veils.
- If possible, it is best to use a lift where the veils can be placed on top and there is nothing beneath them (simulate the environment it will experience when the dish is fully constructed). These results are most in line with what will be see with the full dish and it reduces the issue of the material beneath affecting the results.

# Reference List


[1] K. Jedamzik, and M. Pospelov, “Big Bang Nucleosynthesis and Particle Dark Matter.” *New Journal of Physics*, vol. 11, id. 105028, October 2009.

[2] R. H. Becker, F. Xiaohui, R. L. White, M. A. Strauss, V. K. Narayanan, et al. "Evidence for Reionization at z∼ 6: Detection of a Gunn-Peterson Trough in az= 6.28 Quasar." *The Astronomical Journal* vol. 122, no. 6, pp. 2850-2857, 2001.

[3] D. Clowe, M. Bradac, A. H. Gonzalez, M. Maskevitch, S. W. Randall, et al. "A direct empirical proof of the existence of dark matter." *The Astrophysical Journal,* vol. 648, no. 2, pp. L109-L113, 2006.

[4] E. D. Kovetz, M. P. Viero, A. Lidz, L. B. Newburgh, M. Rahman, et al. "Line-intensity mapping: 2017 status report*." arXiv preprint arXiv:1709.09066*, September 2017.

[5] E. Hubble, “A Relation between Distance and Radial Velocity among Extra-Galactic Nebulae”, *Proceedings of the National Academy of Science of the United States of America*, vol. 15, no. 3, pp. 168–173, April 1929.

[6] H. I. Ewen, and E. M. Purcell, “Observation of a Line in the Galactic Radio Spectrum: Radiation from Galactic Hydrogen at 1,420 Mc./sec.” *Nature,* vol. 168, pp. 356, September 1951.

[7] NASA, “WMAP CMB Fluctuations.” [online]. Available: wmap.gsfc.nasa.gov/universe/bb_cosmo_fluct.html, August 2014.

[8] D. H. Weinberg, M. J. Mortonson, D. J. Eisenstein, C. Hirata, A. G. Riess and E. Rozo, "Observational probes of cosmic acceleration." *Physics Reports,* vol. 530, no. 2, pp. 87-255, September 2013.

[9] B. Bassett, and R. Hlozek, "Baryon acoustic oscillations." *Dark energy: observational and theoretical approaches,* pp. 246, 2010.

[10] Loeb, and J. S. B. Wyithe. "Possibility of precise measurement of the cosmological power spectrum with a dedicated survey of 21 cm emission after reionization." *Physical Review Letters*, vol. 100, no. 16, id. 161301, April 2008.

[11] D. R. Lorimer, M. Bailes, M. A. McLaughlin, D. J. Narkevic and F. Crawford, "A bright millisecond radio burst of extragalactic origin." *Science*, vol. 318, no. 5851, pp. 777-780, September 2007.

[12] Thompson, J. Moran, and G. Swenson, *Interferometry and Synthesis in Radio Astronomy.* Astronomy and Astrophysics Library, Springer International Publishing, 2017.

[13] J. Condon, and S. Ransom, "Essential Radio Astronomy." [online]. Available: www.cv.nrao.edu/~sransom/web/xxx.html, October 2018.

[14] Liu, M. Tegmark, S. Morrison, A. Lutomirski and M. Zaldarriaga, "Precision calibration of radio interferometers using redundant baselines." *Monthly Notices of the Royal Astronomical Society,* vol. 408, no. 2, pp. 1029-1050, July 2010.

[15] M. F. Morales, "Power Spectrum Sensitivity and the Design of Epoch of Reionization Observatories." *Astrophysical Journal,* vol. 619, no. 2, pp. 678-683, February 2005.

[16] M. Wieringa, "The Use of Redundancy in Interferometry – a Comparison of Redundancy and Selfcal." *International Astronomical Union Colloquium*, vol. 131, pp. 192–196, 1991.

[17] W. L. Stutzman and G. A. Thiele, *Antenna Theory and Design*. John Wiley and Sons, 3rd ed., 2012.

[18] M. Deng, and D. Campbell-Wilson, “The cloverleaf antenna: A compact wide-bandwidth dual-polarization feed for CHIME.” *2014 16th International Symposium on Antenna Technology and Applied Electromagnetics (ANTEM)*, pp. 1-2, July 2014.

[19] L. B. Newburgh, K. Bandura, M. A. Bucher, T.-C. Chang, H. C. Chiang, J. Cliche, R. Dave, M. Dobbs, C. Clarkson, K. M. Ganga, et al., "HIRAX: a probe of dark energy and radio transients." *Ground-based and Airborne Telescopes VI.* Vol. 9906, July 2016.

[20] J. Ruze, “The effect of aperture errors on the antenna radiation pattern.” *Il Nuovo Cimento (1943-1954)*, vol. 9, no. 3, pp. 364-380, March 1952.

[21] Facebook, “HIRAX.” [online]. Available: www.facebook.com/HIRAX.Telescope/photos/pb.100057580174247.-2207520000./140193074209344/?type=3. April 2020.

[22] K. Vanderlinde, A. Liu, B. Gaensler, D. Bond, G. Hinshaw, C. Ng et al. "LRP 2020 Whitepaper: The Canadian Hydrogen Observatory and Radio-transient Detector (CHORD)." *Canadian Long Range Plan for Astronomy and Astrophysics White Papers*, vol. 2020, October 2019.

[23] Rj. Clauss, and P. D. Potter, “Improved RF Calibration Techniques--A Practical Technique for Accurate Determination of Microwave Surface Resistivity.” *Deep Space Network Progress Report,* vol. 12, pp. 59-67, September 1972.

[24] D. Henke, G. Lacy, I. Wevers, P. Niranjanan, and F. Miranda, “Fabry-Perot resonator design for the measurement of surface reflectivity.” *2016 Global Symposium on Millimeter Waves (GSMM) & ESA Workshop on Millimetre-Wave Technology and Applications*, pp.1-4, 2016.

[25] D. Pozar, *Microwave Engineering*. John Wiley and Sons, 4th ed., 2011.

[26] E. Pieters, “Prototyping and testing analog electronics and dishes for HIRAX and CHORD”. *McGill University, Master Thesis*, 2021.

[27] Dassault Systemes, “CST Studio Suite 3D EM Simulation and Analysis Software.” [online]. Available: www.3ds.com/products-services/simulia/products/cst-studio-suite.

[28] Tektronix, “What Is a Vector Network Analyzer and How Does It Work?” [online]. Available: www.tek.com/en/documents/primer/what-vector-network-analyzer-and-how-does-it-work, March 2017

[29] Keysight technologies, “SnP File Format.” [online]. Available: rfmw.em.keysight.com/wireless/helpfiles/N1930B/FilePrint/SnP_File_Format.htm.

[30] Keysight Technologies, “ENA Vector Network Analyzers.” [online]. Available: www.keysight.com/ca/en/products/network-analyzers/ ena-vector-network analyzers.html, February 2023.

[31] Keysight Technologies, “FieldFox Handheld RF and Microwave Analyzers.” [online]. Available: www.keysight.com/ca/en/products/ network-analyzers/fieldfox-handheld-rf-microwave analyzers. html, October 2019.

[32] SciPy Documentation, “scipy.signal.find_peaks.” [online]. Available: docs.scipy.org/ doc/scipy/reference/generated/scipy.signal.find_peaks.html, 2021.

[33] K. Torokhtii, A. Alimenti, N. Pompeo, F. Leccese, F. Orsini, *et al,* “Q-factor of microwave resonators: calibrated vs. uncalibrated measurements.” *Journal of Physics: Conference Series,* vol. 1065, no. 5, pp. 2027, 2018.

[34] Dexmet Corporation, “Expanding Technology.” [online]. Available: https://www.dexmet.com/technology, 2023.

# Appendix A: Reflectometer schematic

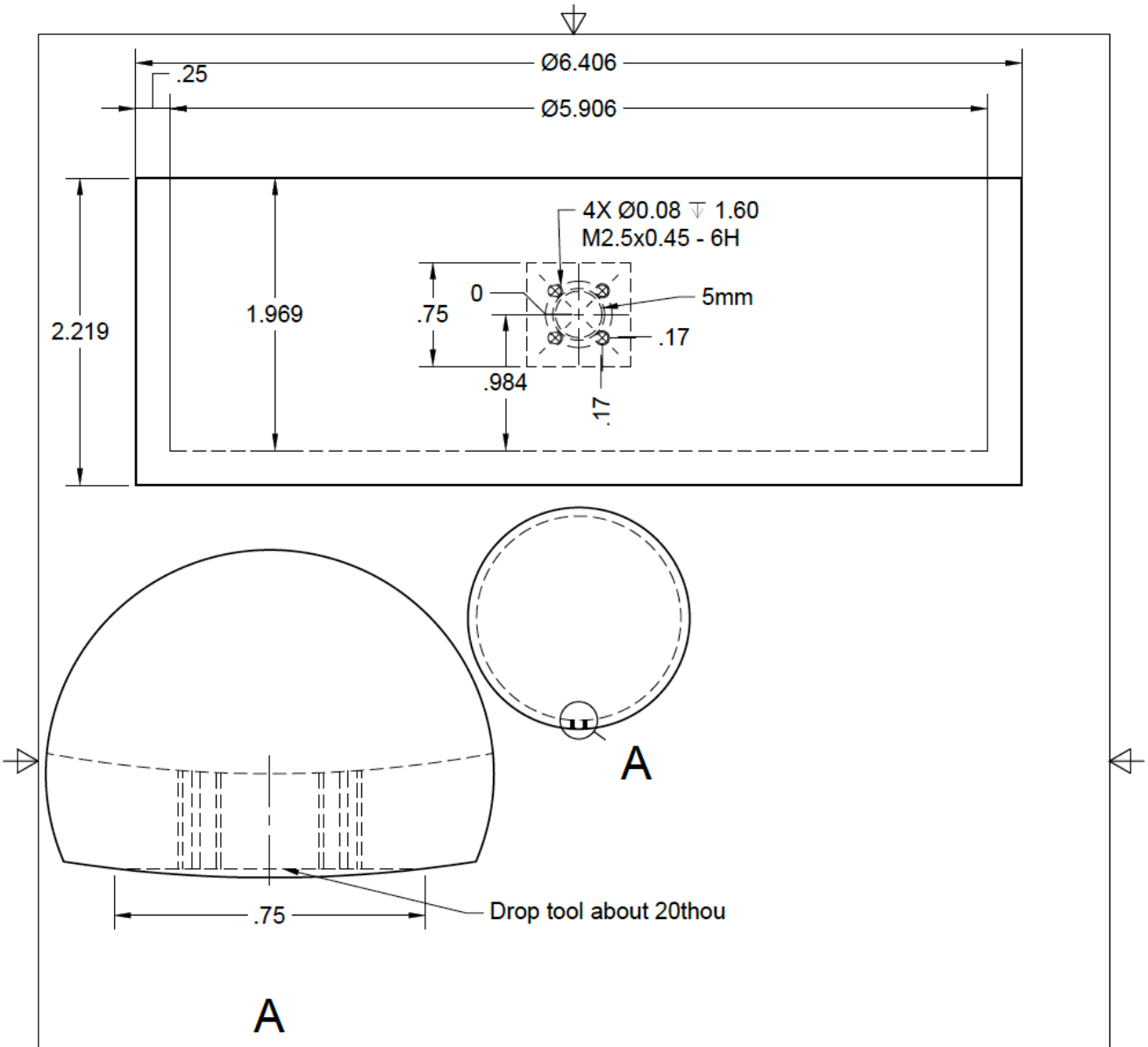


| | | | | | |
|---|---|---|---|---|---|
| | PROJECT: Hirax | | | | |
| | TITLE: resonator | | | | |
| APPROVED | SIZE: A | CODE | DWG NO | | REV |
| CHECKED | | | | | |
| DRAWN: Simon Tartakovsky 2020-11-27 | SCALE: 1:1 | | WEIGHT | SHEET: 1/1 | |